Systematic Studies on Track Reconstruction Efficiency at Belle II

von

Martin Sobotzik

1. Gutachter: Prof. Dr. Wolfgang Gradl
2. Gutachter: Prof. Dr. Niklaus Berger

Ich versichere, dass ich die Arbeit selbstständig verfasst und keine anderen als die angegebenen Quellen und Hilfsmittel benutzt sowie Zitate kenntlich gemacht habe.

Mainz, den 03.12.2019 [Unterschrift]

Martin Sobotzik
Institut für Kernphysik
Johannes-Joachim-Becher-Weg 45
Johannes Gutenberg-Universität D-55128 Mainz
msobotzi@students.uni-mainz.de

Before the sea,
land, and heavens, which cover everything,
the entire world of nature looked the same.
They called that Chaos, a crude, confused mass,
nothing but lifeless stuff and scattered seeds
of matter not yet properly combined,
all piled up in the same place together

Ovid (~ 8 AD) -*Metamorphoses*-
Book I: -*The Primal Chaos*- Verse: 5-9
Translated by: Ian Johnston (2012)

Contents

Contents

1 Introduction, Motivation And Overview

THE standard model of particle physics (SM) is an extraordinarily successful theory which describes three out of the four fundamental forces of nature. The predictions of this theory are extremely accurate within the reach of precision and energy currently available at modern experiments. Nevertheless, the standard model is far from complete because it is unable to answer fundamental questions like the origin of the matter/antimatter asymmetry, the presence of dark matter/energy and the hierarchy problem. Theories which try to answer these questions have been developed suggesting physics beyond the standard model. Nonetheless, these theories lack experimental evidence.

The Belle II experiment is located at the electron-positron collider SuperKEKB at KEK in Tsukuba, Japan. SuperKEKB is a next-generation B factory with a design luminosity of $8 \cdot 10^{35}\,\mathrm{cm}^{-1}\mathrm{s}^{-1}$. It is planned that SuperKEKB will have a data sample corresponding to a recorded integrated luminosity of $\sim 50\,\mathrm{ab}^{-1}$.

The Belle II detector is designed to perform precision measurements in the B and D meson systems as well as searches for rare decays, like lepton flavor violating τ decays. Belle II started taking physics data in early 2019.

The detector consists of a vast variety of sub-detectors each fulfilling a specific purpose, e.g., trajectory reconstruction (tracking), momentum measurements, particle identification. For example, the purpose, amongst others, of the innermost sub-detectors is to reconstruct tracks created by charged particles passing through them. Of course, these sub-detectors are not able to reconstruct every charged particle as such. Therefore, one has to estimate how well they perform.

There are several methods to calculate a tracking efficiency. One method is to select a single physical process with two outgoing charged particles. Then if one particle, in this physical process, is reconstructed as a charged particle we know that the other outgoing particle also has to be a charged particle. Thus, if only one particle in the process is reconstructed as a charged particle then we have an inefficiency. If both particles are reconstructed as charged particles then this is the efficient case. Using this method a tracking efficiency can be calculated.

1. Introduction, Motivation And Overview

In this thesis, this method will be applied to Bhabha events ($e^+e^- \rightarrow e^+e^-$) to measure the track reconstruction efficiency. The selection will be motivated by Monte Carlo-Truth informations. These informations are the true properties of the particles generated in Monte Carlo (MC). Then it will be shown that this selection works even without the Truth information and therefore, can be applied to real data as well. Finally, the tracking efficiencies for different phases of the Belle II detector will be calculated and presented. The tracking efficiencies will be shown for several (transverse) momenta ranges and as function of the polar angle θ and of the azimuthal angle ϕ. We will also differentiate between an electron tracking efficiency and a positron tracking efficiency.

Chapter 2 will present a short introduction to the standard model of particle physics. Additionally, the theory of the Bhabha process will be explained briefly.
In chapter 3 the experimental setup at SuperKEKB will be described. First, the accelerator SuperKEKB will be introduced, followed by the Belle II detector.
Since the ECL will be used as a tool to select Bhabha events, one has to ensure that it sends out a trigger signal in each event which is taken into account. Thus, the trigger and data acquisition system will be described briefly in chapter 4. This chapter will also provide a brief introduction to the analysis framework Basf2.
The specific kinematic properties of Bhabha scattering at Belle II will be calculated and presented in chapter 5.
In chapter 6 the selection used to only take Bhabha events into account with informations solely coming from the ECL will be presented in detail.
Finally, this selection will be used to calculate the tracking efficiency of phase2 in chapter 7 and phase3 in chapter 8.
Since the same selection is used to calculate the tracking efficiencies of phase2 and phase3 one can compare them. This will be done in chapter 9.
A brief summary and conclusion will be given in chapter 10.

In this thesis, natural units are used. This means that $c = \hbar = 1$.

CHAPTER 2
Theoretical Foundations

T HE first part of this chapter will give a brief introduction to the standard model of particle physics. The standard model of particle physics (SM) is a theory that describes three of the four fundamental known forces in the universe: the electromagnetic, the weak and the strong force.

At the current level of experimental precision and the energies reached so far, it is the best theory describing these forces.

Unfortunately, the standard model fails to explain a variety of different observations and since gravitation is not included in the standard model, it is easy to see that the standard model is not complete.

Finally, this chapter will briefly describe the electron-positron scattering process, also known as Bhabha scattering. This process will be used to perform the tracking efficiency later on.

2.1. The Standard Model

The standard model is based on the idea that matter is made of particles with no internal structure. These particles can interact with each other by exchanging other particles which are associated to the fundamental forces. The standard model includes *quantum electrodynamic* (QED), *electroweak theory* (EWT) and *quantum chromodynamic* (QCD) as well as the *Higgs mechanism*.

QED describes all electromagnetic phenomena which are caused by the interaction of photons (γ) and charged point-like particles like electrons and positrons. In the 1920s, Paul Dirac laid the foundation for the QED while computing the coefficient of spontaneous emission of an atom. The description of the weak force (*quantum flavordynamics*, QFD) and the QED got merged by Sheldon Glashow in the early 1960s. The exchange particles of the weak force are the Z and $W^{\pm}$ *bosons*. A few years later, Steven Weinberg and Abdus Salam independently proposed a theory that included the *Higgs mechanism* whereby the *electroweak theory* (EQT) emerged. The Higgs mechanism is the reason why the *gauge bosons* mediating the weak interaction have mass.

Finally, the standard model reached its modern form after combining the EWT and the theory of the strong interaction (*quantum chromodynamics*, QCD). This was done by Abraham Pais and Sam Treiman in 1975. The exchange particles for the strong force are the *gluons* (*g*). They «*glue*» *quarks* (fundamental particles) together, forming *hadrons* like *mesons* (containing two quarks) and *baryons* (containing three quarks). [1]
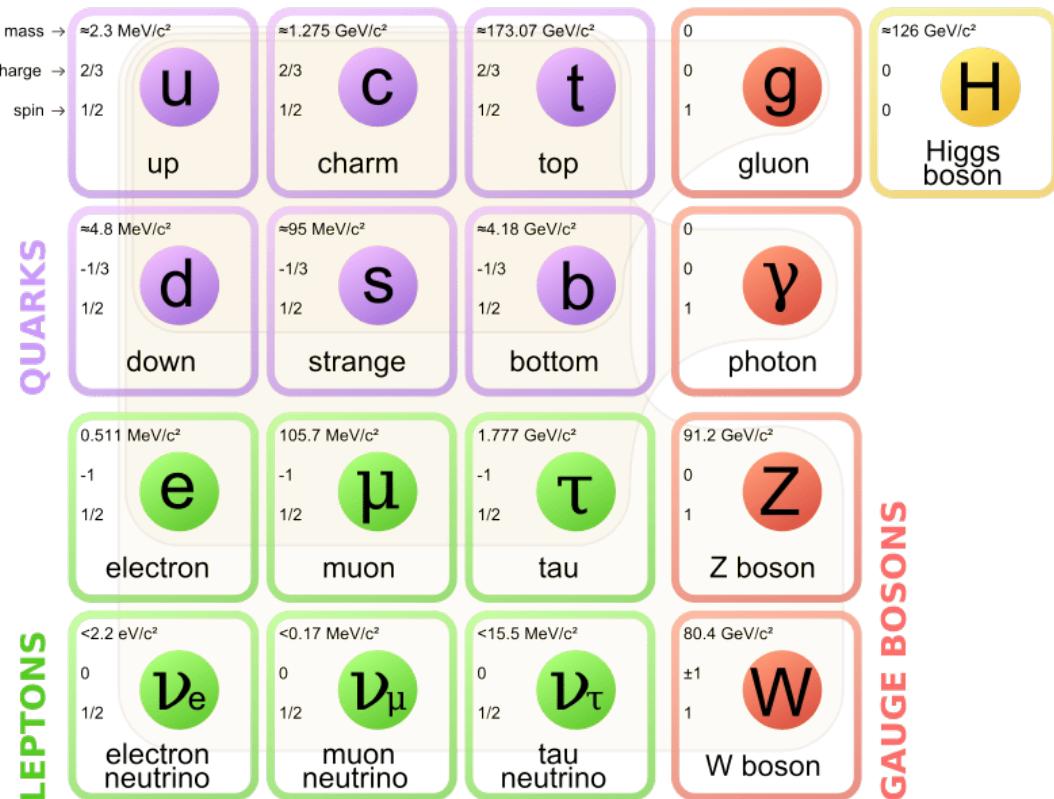
Figure 2.1.: The particles of the standard model include three families of quarks and leptons, four gauge bosons and the Higgs boson. The beige background indicates which bosons interact with which fermions. [2]

Figure 2.1 shows the fundamental particles of the standard model. It includes three families of quarks and leptons so-called *fermions*, four *gauge bosons* and the Higgs *boson*. Fermions and bosons differ in their spin. Spin is a degree of freedom, which had to be introduced to conserve the angular momentum in the Dirac equation. The matter forming fermions have a half-integral spin (in units of the reduced Planck constant $\hbar$) and the bosons (the exchange particles have spin 1 and the Higgs particle has spin 0) have an integer spin. The fermion family can be subdivided into two families, the quark and the lepton family.

The quark family consists of up- (u), down- (d), strange- (s), charm- (c), bottom- (b) and top- (t) quark. Quarks have fractional electric charge values. u-, c- and t-quark

have an electric charge of $^2/_3\,e$, and d-, s- and b-quark have an electric charge of $-^1/_3\,e$. As indicated in figure 2.1 by the beige background, quarks can interact with all four gauge bosons. The lepton family is made of the electron (e), the muon (μ) and the tau (τ) and their corresponding neutrinos ν_e, ν_μ and ν_τ. All leptons can interact via the weak exchange particles ($W^\pm$ and Z bosons), and since the electrons, muons and taus are charged, they can also interact with photons.

All fermions also have so-called *antiparticles*. Antiparticles have the same mass as their corresponding particle but they have opposite charge. For example, the antiparticle of the electron is the positron. Both have the same mass and the same spin but the electron has an electric charge of $-1\,e$ and the positron has an electric charge of $+1\,e$. When a particle collides with its antiparticle *annihilation* can occur. In an annihilation process the incoming particles are destroyed to produce other particles. In this process, overall energy and momentum are conserved.

All visible matter in the universe is made out of fermions from the first family. For example, atoms consist of protons and neutrons, each of which is a combination of up and down quarks. In the electron shell of an atom the eponymous electrons are located. Pauli proposed the neutrino in the 1930 to explain the energy spectrum of electrons in β-decays. Since neutrinos are only weakly interacting particles, they were not observed until 1956.[3] With increasing energy, more and more particles of the standard model have been discovered gradually, first from cosmic ray experiments in the 1930s up to the discovery of the Higgs boson at the Large Hadron Collider (LHC) at CERN in 2012. Parallel to the experimental discoveries, the theory also evolved, partially explaining the results and in part motivating new experiments through predictions.

2.2. Physics Beyond The Standard Model

Despite the success of the standard model, it fails to answer many open questions. As already mentioned, the standard model only includes three of the four fundamental forces; it does not include gravity, and it is not valid at energy scales approaching the Planck energy, $E_P \approx 10^{19}$ GeV.[4] Additionally, it also does not describe observations like:

- Dark matter: the mass of all visible matter in spinning galaxies is not large enough to counteract the centripetal force, therefore additional massive particles which do not interact electromagnetically have to be introduced. They are called dark matter. The universe consists of $\sim 27\,\%$ dark matter.[5]

- Dark energy: Observations of supernovae in distant galaxies showed that the expansion of the universe is accelerating. The theory of dark energy was created to explain this observation. Dark energy is an unknown form of energy and it is thought that it permeates the universe. The universe consists of $\sim 68\,\%$ dark energy.[6]

- Matter-Antimatter asymmetry: The standard model requires conservation of the number of baryons, and the big bang should have created equal amounts of matter and antimatter. However, today the universe almost exclusively contains matter. This is directly linked to charge-parity violation.[7]

These observations motivate searches for physics beyond the standard model, so-called *new physics*. New physics could manifest itself by the presence of new particles or forces that are not described by the standard model.

2.3. Bhabha Scattering

In this section the physics of Bhabha scattering will be discussed briefly.

2.3.1. Bhabha Process

Bhabha scattering is a quantum electromechanical process between an electron and a positron. It is named after the Indian physicist Homi Bhabha who first derived the electron-positron scattering cross section in 1935.[8]
In a Bhabha process there is an electron and positron in the initial and final state.
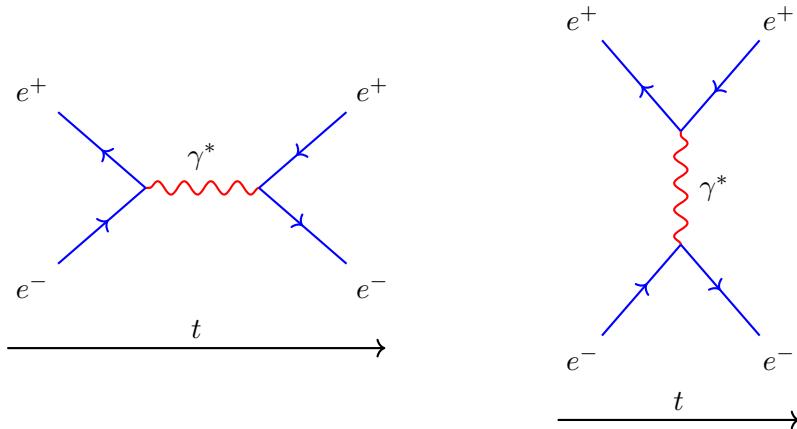
Figure 2.2.: The two leading-order Feynman diagrams of the Bhabha process. The left diagram describes the annihilation and pair production process, whereas the right diagram describes a classic electromagnetic scattering process.

Figure 2.2 shows the two leading-order Feynman diagrams of the Bhabha process. A Feynman diagram is a visual representation of an interaction described by quantum field theory. These diagrams are strictly translatable into mathematical expressions. The time passes from the left to the right side. In the left Feynman diagram the initial electron and positron annihilate to form a virtual photon γ^*. This virtual photon then decays into an electron and a positron. The right Feynman diagram describes a classic electrodynamic scattering process. Here the incoming electron and

positron are scattering via interaction of a virtual photon. In contrast to the right diagram, the left diagram can only be explained by quantum field theory, due to the creation and destruction of particles.

2.3.2. Differential Cross Section Of Bhabha Process

A cross section describes the probability that two particle will interact with each other when they collide. Then the intensity distribution of the outgoing particles over the spatial direction Ω is described by the differential cross section $\mathrm{d}\sigma/\mathrm{d}\Omega$.
The differential cross section for the electron[1] in a Bhabha process is given by equation 2.1.

$$\left(\frac{\mathrm{d}\sigma}{\mathrm{d}\Omega}\right)_{\mathrm{cms}} = \frac{e^4}{32\pi^2 E^2}\left(\frac{1+\cos^2(\theta)}{2} + \frac{1+\cos^4(\theta/2)}{\sin^4(\theta/2)} - \frac{2\cos^4(\theta/2)}{\sin^2(\theta/2)}\right) \tag{2.1}$$
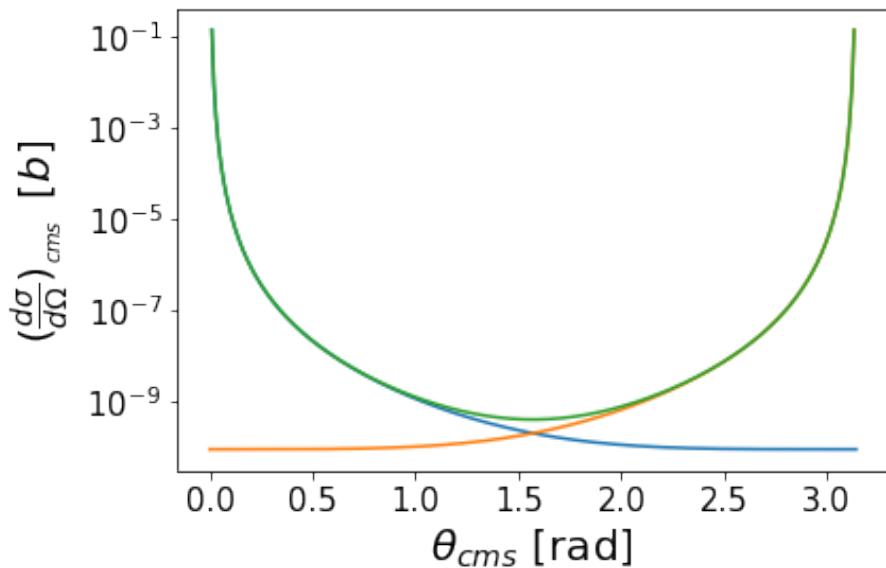
Figure 2.3.: This figure shows the differential cross section for the Bhabha process.

In figure 2.3 the differential cross section for electrons is plotted in blue. Since most incoming particles are only very slightly deflected, the cross section is very high for small scattering angles and gets smaller with increasing angle. Equation 2.1 is also true for positrons but they are moving in the opposite direction. Therefore, θ has to be replaced by $\pi - \theta$ for positrons. The result is plotted in the same figure but in orange.
To get to differential cross section for the Bhabha process, one has to add the differential cross section of electrons and positrons. This is also shown in figure 2.3. The

---

[1]The electrons are moving along the x-axis. The positrons are moving in the opposite direction

differential cross section of the Bhabha process is shown in green. As can be seen in this figure, most of the outgoing particles will have a very small or very large angle θ.

3
Experimental Setup At SuperKEKB

$\mathcal{S}$UPERKEKB is a two-ring, asymmetric[1], electron positron accelerator, which is located at KEK (*High Energy Accelerator Research Organization*) in Tsukuba, Japan. The electron beam has an energy of 7 GeV and the positron beam has an energy of 4 GeV. These beams collide with a center-of-mass energy of about 10.58 GeV, which is close to the mass of the $\Upsilon(4S)$ meson resonance. $\Upsilon(4\,S)$ decays, almost exclusively, in two *B*-mesons, making SuperKEKB a so-called *B-factory*. The decay products are then detected by the Belle II detector to study the properties of these B mesons with high precision. In early 2018, Belle II started taking data. One goal of Belle II is to study CP-Violation.[9]

3.1. KEKB And SuperKEKB

This section will only provide a brief overview of the SuperKEKB accelerator.
SuperKEKB is an upgrade of the KEKB accelerator. KEKB was also an asymmetric electron positron accelerator in the period from 1998 to 2010, but the energies were different compared to SuperKEKB. At KEKB the electrons were accelerated to an energy of 8 GeV and the positrons to an energy of 3.5 GeV. KEKB was also a B-factory and the reaction products were then detected in the Belle detector. In 2009, KEKB achieved an instantaneous luminosity of $\mathcal{L} = 2.11 \cdot 10^{34}\,\mathrm{cm}^{-1}\mathrm{s}^{-1}$. This was the world record at that time. KEKB was discontinued after more than 10 years, to be upgraded to SuperKEKB.[10]
In figure 3.1 the schematic layout of the SuperKEKB accelerator is shown. The electrons start at the low emittance gun. Then they are accelerated in the *J*-shaped linear particle accelerator (linac). Due to lack of space, the linac has to have this special form.[12] After the curve and a second acceleration stage the electrons hit the positron production target, where the positrons are created. After this target there are more acceleration stages, before the two beams are then finally injected into their independent storage rings. The electrons are stored in the high-energy ring (HER) and the positrons are stored in the low-energy ring (LER). Each of these rings has

---

[1]asymmetric means that there is an energy difference between the two colliding beams
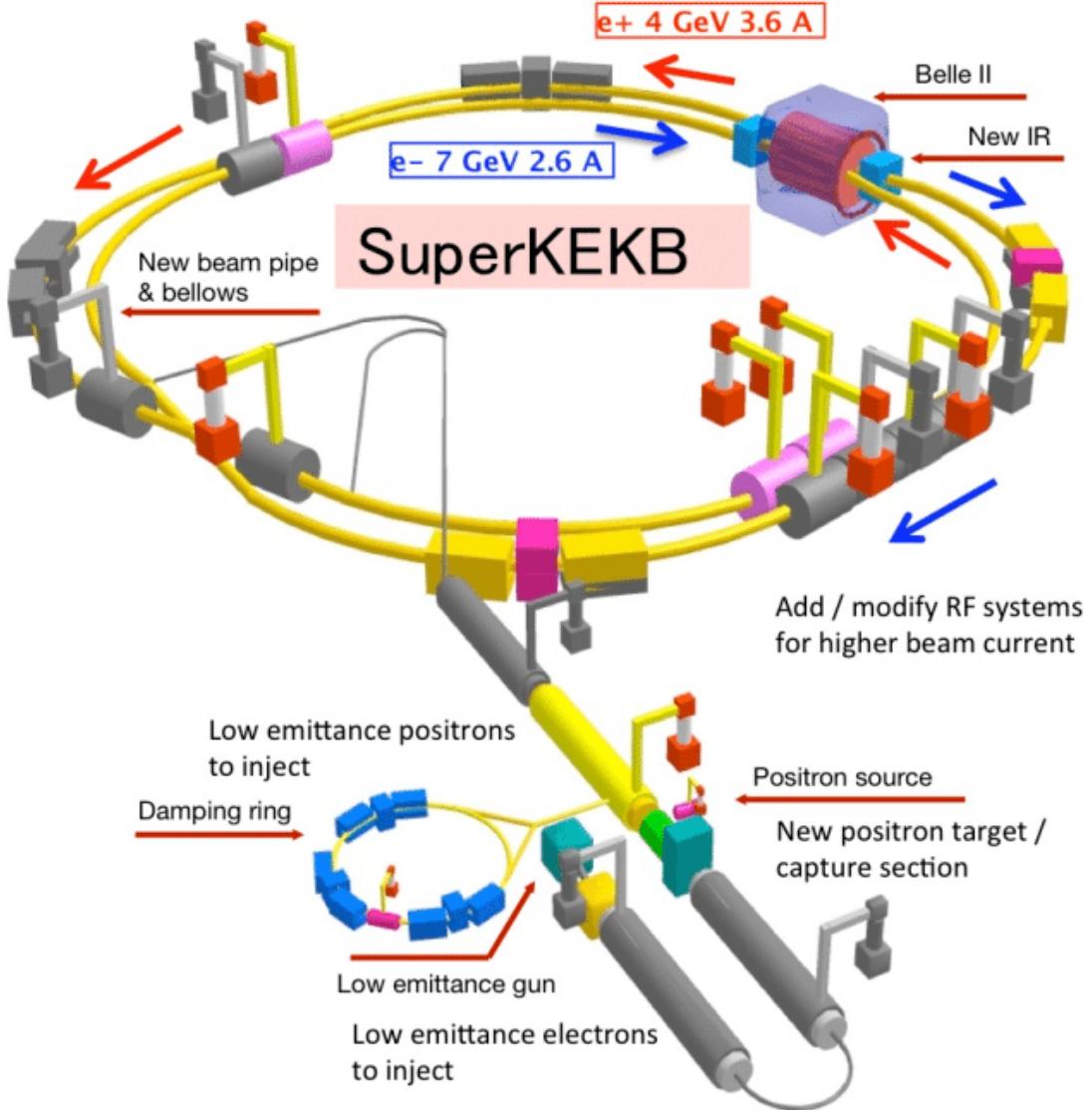
Figure 3.1.: The SuperKEKB collider.[11]

a circumference of about 3 km. Both beams collide at the interaction region (IR). The products of the collisions are then detected by the Belle II detector, an upgraded version of the Belle detector.[9] (See section 3.2)

SuperKEKB uses a smaller asymmetry in the beam energies compared to KEKB. This allows the usage for higher beam currents and better focusing magnets. Ultimately, this will result in a higher luminosity. The goal is to achieve a 40 times higher luminosity with SuperKEKB compared to KEKB. An integrated luminosity of $50 \, \text{ab}^{-1}$ is planned to be achieved by 2025.[9]

The instantaneous luminosity $\mathcal{L}$ specifies the performance of the collider. Knowing $\mathcal{L}$ and the cross section σ one can calculate the events per second for a process by the following formula.

$$\frac{\mathrm{d}N}{\mathrm{d}t} = \mathcal{L} \cdot \sigma \tag{3.1}$$

To increase the event rate one has to increase the instantaneous luminosity since σ is given by the processes. The instantaneous luminosity of a collider can be calculated by the following equation:

$$\mathcal{L} = \frac{N_{e^-} N_{e^+} f_c}{4\pi \sigma_x \sigma_y} \cdot S \tag{3.2}$$

One has to assume that both beams have a Gaussian profile of horizontal and vertical size σ_x and σ_y. In equation 3.2 N_{e^-} is the number of particles in an electron bunch and N_{e^+} is the number of particles in a positron bunch. f_c is the average crossing rate, which can be calculated by $f_c = n \cdot f_r$, where n is the number of bunches and f_r is the revolution frequency. S is a reduction factor which takes geometrical effects linked to the finite cross section and bunch length into account.[13] SuperKEKB increased the luminosity by a factor of two compared to KEKB by increasing the number of bunches and the number of particles per bunch.
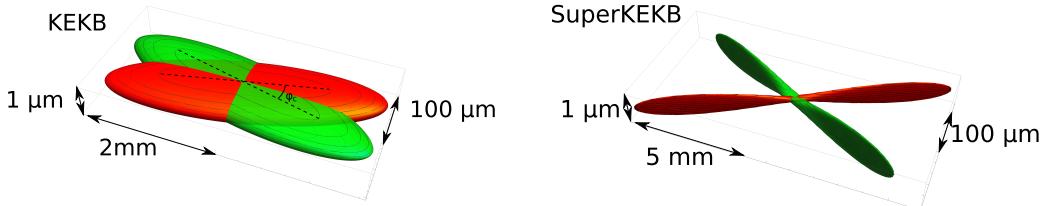

Figure 3.2.: Sketch of the beam crossing at KEKB (left) and SuperKEKB (right). At KEKB the size of the interaction region in z-direction was about 10 mm. At SuperKEKB it is about 0.5 mm.[14] This figure was edited in order to make the axis more readable.

Additionally, the size of the interaction region at SuperKEKB is just one twentieth of what it was at KEKB, resulting in a vertical beam size of $\sigma \approx 50$ nm. This can be seen in figure 3.2. This decrease in beam size along with the increase in the beam currents results in an overall 40-fold increase in luminosity. [15] [9] At SuperKEKB the crossing-angle of both beams is just 1.26°.

3.2. The Belle II Detector

The Belle II detector is an upgraded version of the Belle detector which was a solid-angle magnetic spectrometer located at the interaction region of KEK. In figure 3.3 a sketch of the Belle II detector is shown. The detector contains a variety of sub-detectors, each fulfilling a specific purpose.

Pixel Detector（PXD）

Silicon Vertex Detector（SVD）

Central Drift Chamber（CDC）

TOP counter（TOP）

Aerogel RICH counter（ARICH）

Electromagnetic Carolimeter（ECL）

K$_L^0$／Muon Detector（KLM）
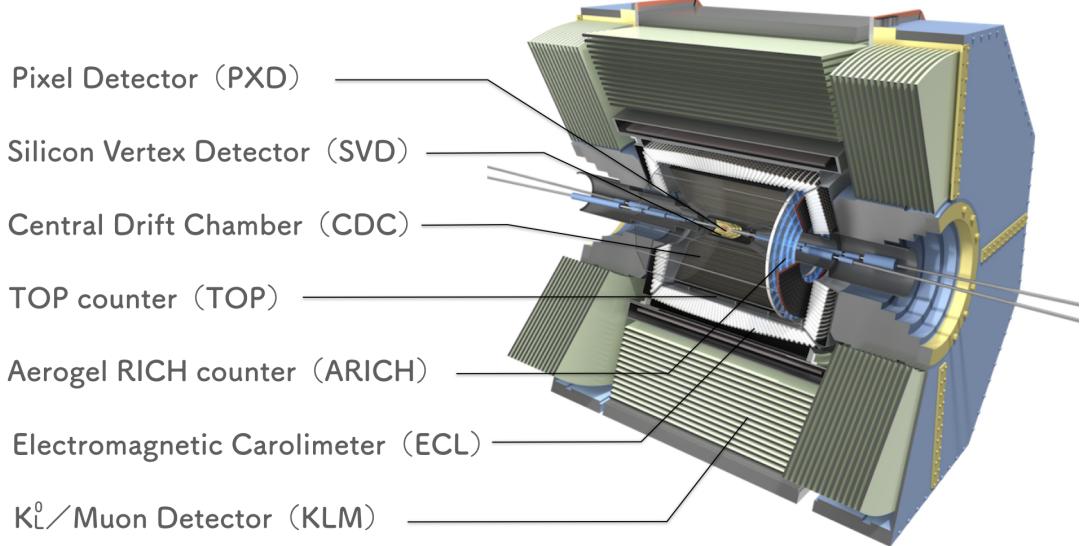
Figure 3.3.: Schematic view of the Belle II detector. The different detector elements are labeled. [16] This figure was modified in order to make the text more readable.

In the innermost segment of the detector, three tracking sub-detectors are located surrounding the IR. These sub-detectors are in an axial magnetic field of 1.5 T provided by a solenoid, to be able to reconstruct the trajectories (tracks) of charged particles.

The vertex detectors, consisting of the silicon vertex detector (SVD), an upgraded version of the SVD used in Belle, and the pixel detector (PXD), a new detector designed for Belle II, are used to measure the momenta of charged particles and to reconstruct decay vertices and particles with a momentum too low to reach the central drift chamber (CDC).

The CDC also already existed in the Belle detector and has been upgraded for Belle II. The CDC scans the trajectories of charged particles. From these trajectories the charge, momentum and energy loss can be determined from ionization.

These three innermost tracking detectors are surrounded by a barrel. The time-of-propagation (TOP) detector, which also got an upgrade for Belle II, surrounds the inner detectors parallel to the beam-pipes. The TOP detector, as the name suggests, measures the flight-time of charged particles. Knowing the flight-time and the momentum of the charged particles, it is possible to conclude their mass and to identify them. The forward end-cap of the barrel is closed with an Aerogel Ring-Imaging Cherenkov detector (ARICH) which also identifies charged particles.

The next outer detector is the electromagnetic calorimeter (ECL). It surrounds all the previously mentioned detectors, and was already installed in Belle. The ECL is able

to measure the energy of electromagnetically interacting particles, especially photons and electrons.

The task of the outermost detector the K_L^0 and muon detector (KLM) is to identify K_L^0 and muons. The KLM also got upgraded for Belle II. [9]

3.3. Coordinate System

For the sake of clarity, the coordinate system of Belle II will be described in this section, before the detectors are explained in more detail.
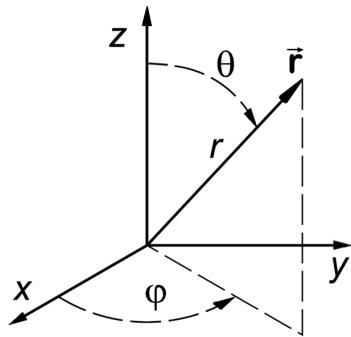

Figure 3.4.: A sketch of the coordinate system of Belle II. [17]

A sketch of the coordinate system is shown in figure 3.4. The origin of the coordinate system corresponds to the interaction region. For the Cartesian coordinate system: The z-axis points in the direction of the magnetic field. This is also called the forward direction. The y-axis points up to the upper part of the detector. The x-axis points along the radial direction of the accelerator. The electrons are moving roughly along the positive z-axis, while the positrons are moving in the opposite direction. In figure 3.4 also the spherical coordinate system is shown. Here θ corresponds to the polar angle and ϕ to the azimuthal angle.[18]

3.4. Vertex detector

The vertex detectors (VXD) are able to make precise measurements of the tracks of particles close to the interaction region. This allows the reconstruction of decay-vertices of long-lived particles. For this it is very important to determine the distance and the spatial resolution of the first measured hit, and the effect of multiple scattering.

The VXD consists of the pixel vertex detector and the silicon vertex detector, both can be seen in figure 3.5. These two detectors complement each other.
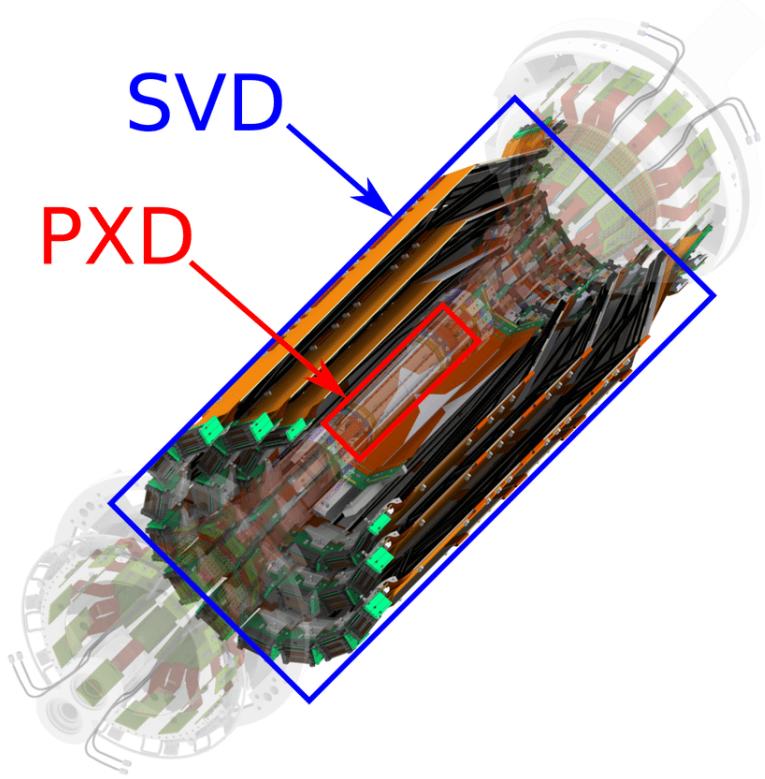
Figure 3.5.: Sketch of the vertex detectors. The vertex detector itself consists of two sub-detectors. The PXD is surrounded by the SVD. [19]

3.4.1. Pixel Vertex Detector

The purpose of the PXD is to reconstruct the spatial position of the decay vertices of B, D and τ. The PXD is based on Depleted P-channel Field-Effect Transistor (DePFET) technology. This technology allows the sensors of the PXD to be very thin ($\sim 50\,\mu$m).

As can be seen in figure 3.6, the PXD consists of two layers of sensors. The inner layer is made out of eight planar sensors (ladder), each has a width of 15 mm and an effective length of 90 mm. This layer has a radius of 14 mm. The second layer consists of 12 planar sensors. These sensors also have a width of 15 mm but a length of 123 mm. The radius for the second layer is 22 mm. The PXD provides a spatial resolution of about $1.2\,\mu$m.[15]

Due to the vicinity of the PXD to the interaction region, the QED background is very high, so the sensors must withstand high radiation. The DePFET technology fulfills this condition. [15] [20]
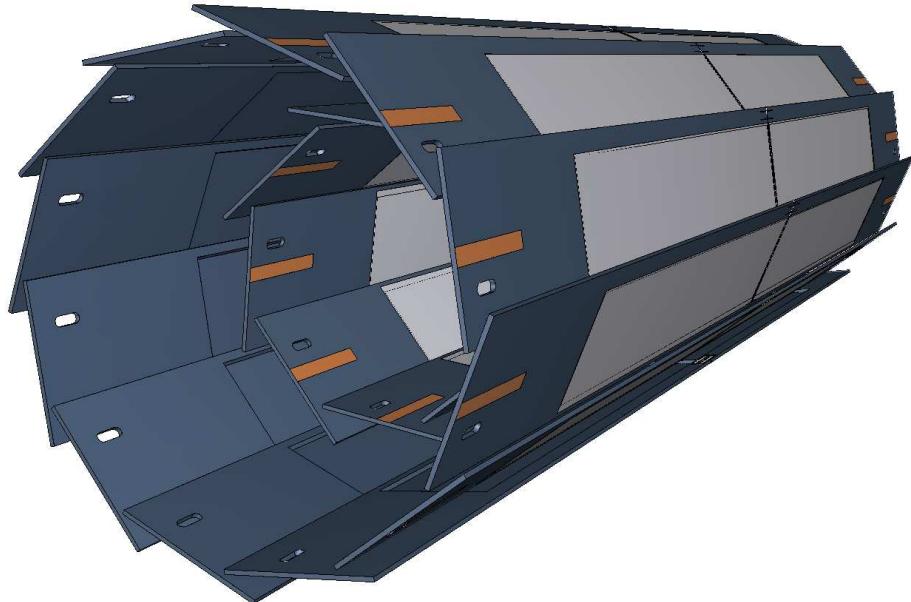
Figure 3.6.: Sketch of the complete PXD [15]

DePFET is a semiconductor detector concept invented in 1987 by J. Kemmer and G. Lutz of the MPI for Physics. This concepts combines detection and amplification in one single device. [15]
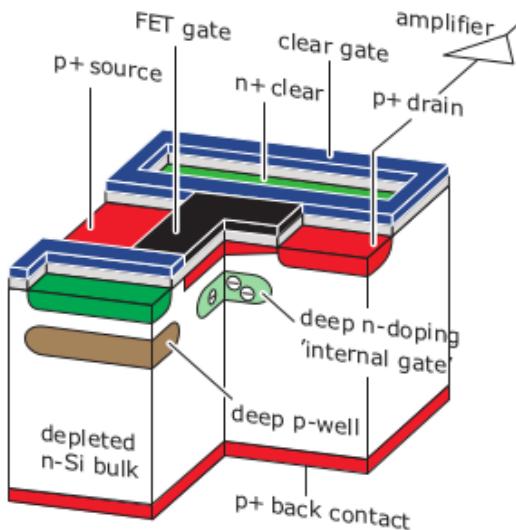

Figure 3.7.: Illustration of the DePFET technology.[15]

A cross section of the device is shown in figure 3.7. The structure of a DePFET cell consists of fully depleted silicon. In this silicon substrate, depleted by a high negative voltage, a $p-$channel MOSFET (metal oxide semiconductor field effect transistor) of a JFET (junction field effect transistor) is integrated. The field effect transistors act as a first pre-intensification. When radiation or a particle hits the detector, electron-hole pairs are created. These pairs get separated by the potential field of the sidewards depletion. The positive charged holes drift to the negatively charged back contact. The negative charged electrons are collected in the potential minimum, the so-called internal gate. Above the internal gate a field emission transistor is located. The signal charge is amplified right above the position where it was generated. This avoids the leakage of lateral charge transfers. One of the most important main features of the DePFET technology is that the internal gate has a very small capacitance. This makes it possible to measure events affected by low noise even at room temperature.[15]

3.4.2. Silicon Vertex Detector

The SVD covers a polar angle region of $17.0° < \theta < 150.0°$. It consists of four layers of double-sided strip detectors. The layers are located at radii of 38, 80, 115 and 140 mm. There are two different shapes of these sensors. The rectangular sensors are used in the barrel part and the trapezoidal sensors are used in the forward region of the SVD. Each sensor has a thickness of $320\,\mu$m but the sensors have different dimensions depending on the layer they are located. The barrel sensors in the most inner layer of the SVD have a dimension of $38.4 \times 122.8\,\text{mm}^2$. The size for the barrel sensors of the other layers is $57.6 \times 122.8\,\text{mm}^2$. The trapezoidal sensors have a dimension of $38.4\,\text{mm}$ on the small side of the trapeze to $57.6\,\text{mm}$ on the long side of the trapeze times a length of $122.8\,\text{mm}$.[15] An illustration of the SVD can be seen in figure 3.8. In the barrel region the p-side of the double-sided-strip sensors is arranged parallel to the beam axis and facing the interaction region. The n-side is facing outside the detector and the n-strips are perpendicular arranged to the beam axis.

When a particles travels through the sensors it creates electron-holes pairs along its path by ionization. The electrons then propagate to the n-strips and are accumulated there. The holes propagate to the p-strips and are collected there. The sensors then produce a signal from which the coordinate of the particle position can be read out. The p-side provides the z-direction and the n-side provides the r-θ direction.[15] [22]

3.5. Central Drift Chamber

The CDC surrounds the SVD and also covers a polar angle region of $17.0° < \theta < 150.0°$. It consists of 14336 wires arranged in 56 layers and has an inner radius of 16 cm and an outer radius of 113 cm. The volume is filled with a 50 % helium and a 50 % ethane gas mixture. The purpose of the CDC is to reconstruct the momenta and tracks of charged particles, to identify these particles by measuring their specific energy loss within the gas volume. The CDC alone is able to identify low-momentum tracks, which are unable to reach the particle identification device. The CDC also
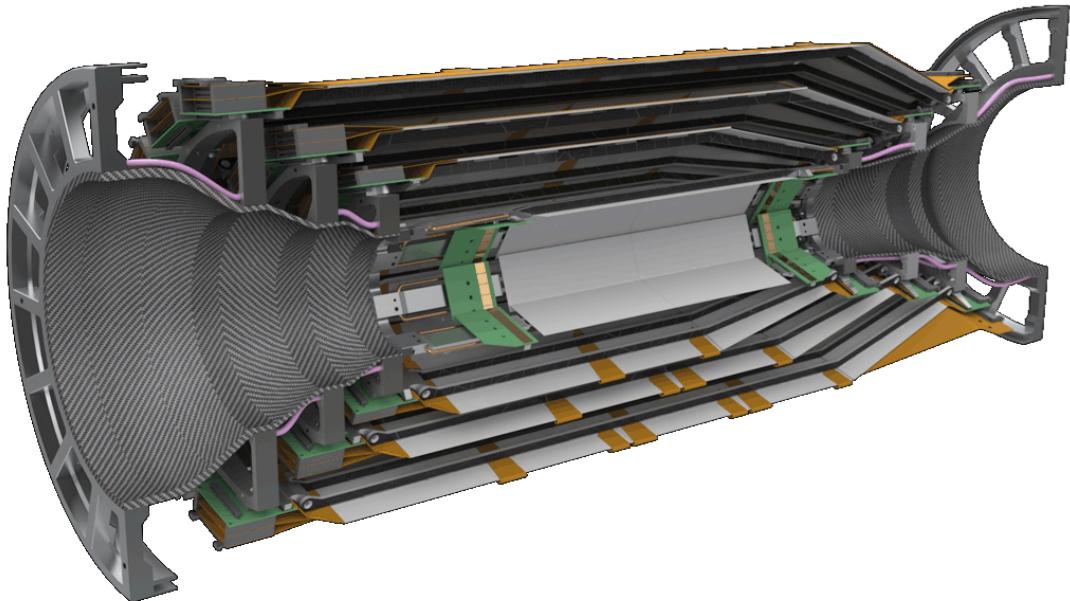
Figure 3.8.: Cross section of the silicon vertex detector[21]

acts as a reliable trigger for charged particles.[15] A small cross section of the CDC is shown in figure 3.9.
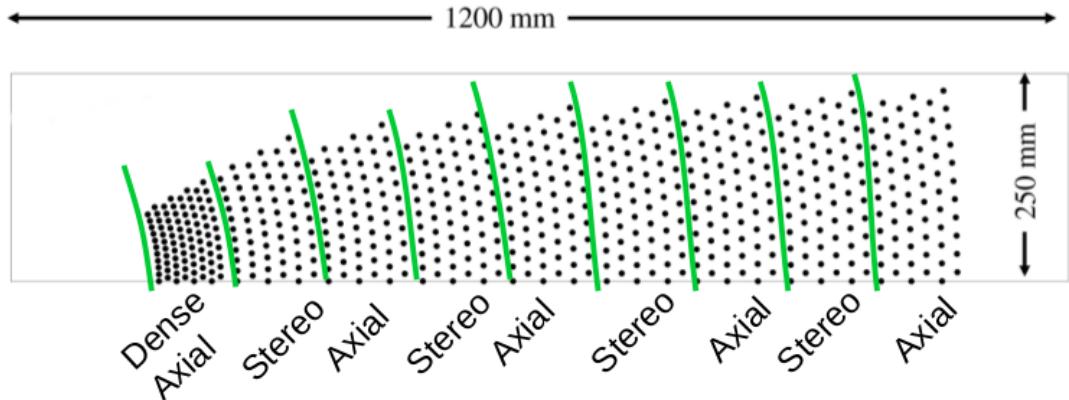
Figure 3.9.: Cross section and only a small part of the CDC. Each dot represents a wire. Additionally, the area for the different superlayers are separated by the green line. All of these wires are immersed in a helium-ethane mixture.[23]

When a charged particle passes through the CDC it losses energy due to ionization of the gas. This produces electron-ion pairs, which are then separated by the electric field provided by 42240 aluminum field wires with a diameter of $125\,\mu$m. The signal

is then read out by the sense wires. These have a radius of $30\,\mu$m and are made out of gold-plated tungsten.[15]

As indicated in figure 3.9, there are different superlayers in the CDC. The Dense Axial and Axial sense wires allow the reconstruction of the track in the r-ϕ plane. The stereo sense wires give information about the z-direction. These stereo wires are tilted with respect to the z-direction. Six layers of sense wires are combined to a superlayer. The CDC consists of five axial superlayers (A) and four stereo superlayers. The four stereo superlayer are subdivided into two stereo superlayers (U) with a positive stereo angle and two stereo superlayers (V) with a negative stereo angle. Starting with the innermost superlayer, every second superlayer is an axial superlayer. The stereo superlayers are between them, alternating between U and V. The stereo angles of the innermost stereo (first) superlayer ranges between 45.4 mrad and 45.8 mrad, the second between -55.3 mrad and -64.3 mrad, the third between 63.1 mrad and 70.0 mrad and the fourth between -68.5 mrad and -74.0 mrad. All five axial superlayers have a stereo angle of 0 mrad. In total there are nine superlayers. The innermost superlayer, called *small-cell chamber*, is realized with a denser packing of wires and has a total of eight layers (compared to the other superlayers with just six layers). This was done to lower the influence of the background, which is higher in the innermost superlayer due to the vicinity to the interaction region. The CDC has a spatial resolution of about $100\,\mu$m.[15]

3.6. Time-Of-Propagation And Aerogel Ring-Imaging Cherenkov Detector

There are two additional detectors for particle identification, the TOP and the ARICH. The TOP counter is located in the barrel part and it uses a combination of time-of-flight and Cherenkov angle measurements. When a charged particle with the velocity β is faster than the speed of light c_n in a medium with a reflective index n then this particle emits Cherenkov radiation under the angle θ_C.[24]

$$c_n = \frac{c_0}{n} \leq \beta \tag{3.3}$$

The Cherenkov angle is given by [24]:

$$\cos(\theta_C) = \frac{1}{n\beta} \tag{3.4}$$

Figure 3.10 shows an illustration of the functionality of a TOP bar. The charged particle emits Cherenkov light when it passes the quartz crystal. These photons then travel inside the crystal due to reflection until they are detected by a photon detector. Measuring the time difference between the emitted photons it is possible to calculate the position of the track of the charged particle. Then the outgoing photons are focused by mirrors and are finally detected by PMTs. Cherenkov photons with different θ_C will be detected by different PMTs. Therefore, the TOP reconstruct the Cherenkov ring image using the information of time, x and y.[15]

Figure 3.10.: Operating mode of a TOP detector.[15]

The TOP counter consists of 32 quartz bars. They have a length of $1250\,\text{mm}$, a width of $45\,\text{mm}$ and a depth of $20\,\text{mm}$. There are two quartz bars per module. The TOP counter has a K/π separation of over $96\,\%$ at a momentum of $4\,\text{GeV}$.[15]

The ARICH detector is located in the forward end-cap region. It is designed to distinguish between kaons and pions over most of their momentum spectrum. It is also able to identify particles with a momentum below $1\,\text{GeV}$.
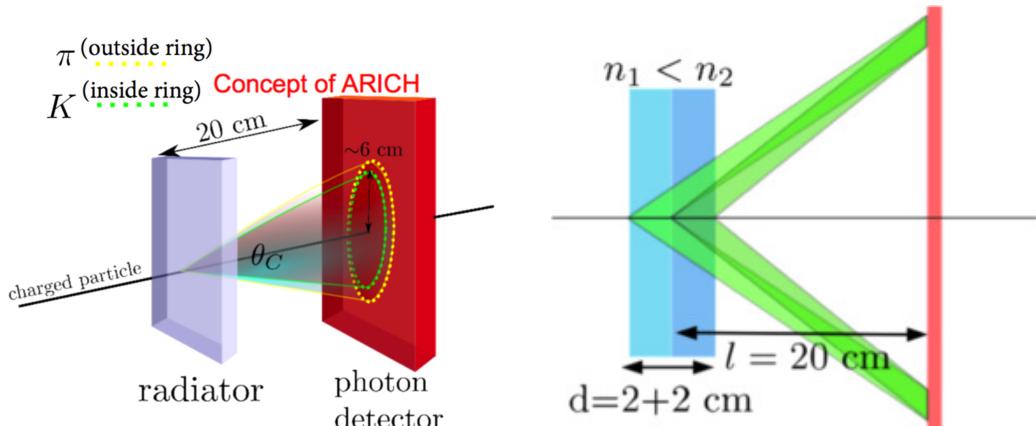

Figure 3.11.: Left: Illustration of the working principle of the ARICH detector. The yellow Cherenkov ring on the photon detector is produced by a pion, the green ring by a kaon. Right: The radiator is shown in more detail. The radiator consists of two aerogel layers with different reflective index. [25]

In figure 3.11 the working principle of the ARICH detector is shown. A charged particle passes through two layers of an aerogel radiator with different refractive indexes and emits Cherenkov photons under a Cherenkov angle θ_C. Behind the radiator, an extension volume, for the Cherenkov rings to form, is located. At a distance of $20\,\text{cm}$ behind the radiator the photon detectors are placed.[15] Once the Cherenkov ring is reconstructed, the radius of the ring can be determined and, knowing the distance and the radius, the Cherenkov angle can be calculated.

3.7. Electromagnetic Calorimeter

One of the main tasks of the ECL is the detection of photons with a high efficiency. It determines the energy and the angular coordinates of these photons with high precision. It is also used for electron identification and the generation of a proper signal for the trigger. The ECL consists of a 3 m long barrel section with an inner radius of 1.25 m. The circular end-caps are located at a distance of $z = 1.96$ m in the forward direction and $z = -1.02$ m in the backward direction from the interaction region. The ECL covers a polar angle region of $12.4° < \theta < 155.1°$. Due to construction, there are two $\sim 1°$ wide gaps between the barrel and the end-caps. The barrel section of the calorimeter consists of 6624 CsI(Tl)[2] crystals with 29 distinct shapes. Each of these crystals is a truncated pyramid with an average size of about $6 \times 6 \, cm^2$ in cross section and 30 cm in length. The length of these crystals corresponds to around 16.1 radiation lengths X_0. The end-caps consist of 2122 CsI crystals of 69 shapes. At the end of each crystal, photo-multiplier are mounted to detect the excitation of the scintillators. The detected number of photons corresponds directly to the energy released by absorbed particles. The energy resolution of the calorimeter can be approximated by [15] [26]:

$$\frac{\sigma_E}{E} = \sqrt{\left(\frac{0.066\%}{E}\right)^2 + \left(\frac{0.81\%}{\sqrt[4]{E}}\right)^2 + (1.34\%)^2} \qquad (3.5)$$

The energy E is in GeV.

Photons and electromagnetic particles are creating electromagnetic cascades when they pass through material.[27] When a high energetic photon passes through a material it creates an electron-positron pair by pair production. For this the photon must have an energy of at least $2 \cdot m_{e^-} = 1.022$ MeV. This energy is evenly distributed amongst the two particles. Because these two particles are charged and their velocity changes in an the electric field of a nuclei, they generate photons through bremsstrahlung. These processes are repeated and an electromagnetic shower is created. The energies of the particles continue to decrease until the critical energy E_c is reached. At the critical energy the energy loss due to bremsstrahlung is as high as the energy loss due to ionization.

If the average energy of an electron becomes E_0/e then the distance the electron traveled is called radiation length X_0.

Assuming that the electromagnetic particles and photons interact after one radiation length and that they lose half of their energy each time they do, the total number of particles and their energy after t cascades can then be calculated by [27]:

$$N \simeq 2^t \qquad (3.6)$$

$$E(t) \simeq \frac{E_0}{2^t} \qquad (3.7)$$

---

[2]Thallium activated Cesium Iodide

This shower spreads both longitudinally and transversely. The transverse propagation can be described by the Molière radius. It can be calculated by:

$$R_{\mathrm{m}} = 21 \, \mathrm{MeV} \cdot \frac{X_0}{E_c} \qquad (3.8)$$

95 % of all particles of a shower are within two Molière radii.[27]

3.8. K_L^0 And Muon Detector

The KLM consists of an alternating sandwich structure of a 4.7 cm thick iron plates and resistive plate chambers (RPC) in between.

RPCs consist of two glass sheets separated by a thin gas volume. These sheets act as high voltage electrodes. When a particle passes through the volume, they create ion-electron pairs which are then accelerated by the strong electric field. Therefore, they initiate more ionization, which leads to a shower between the electrodes. This causes a voltage drop in the nearby electrodes, which is detected by pick-up strips, located on both sides of the chamber. These strips are a few centimeters wide and are placed orthogonally on each side. Therefore, the particle track can be localized in z/ϕ for the barrel region and ϕ/θ for the end-caps.

To distinguish between muons and hadrons, the KLM takes advantage of the high penetration power of muons. Hadrons deplete their energy through hadronic showers in the ECL and KLM. Electrons have a shorter radiation length and are therefore absorbed by the ECL most of the time. The K_L^0 create clusters in the ECL and the KLM. These clusters are then grouped and geometrically matched to charged tracks which are detected by the inner detectors. If no corresponding charged track can be found by geometrical matching, the detected particle is then treated as a K_L^0 candidate.[15][28]

4 Data Flow And Reconstruction Software

I~n~ this chapter a brief introduction to the trigger system and the data acquisition system as well as the analysis software at Belle II is provided.

4.1. Trigger

The online event selection system (trigger) for Belle II makes it possible to acquire data from the detector based on information from a set of sub-detectors. The individual triggers are structured in a hierarchy. Each sub-trigger system provides the trigger information from the corresponding sub-detector to the global decision logic (GDL). This global trigger decides whether the event should be written out or not. [15] A schematic overview of this trigger hierarchy can be found in figure 4.1.
The trigger system has to fulfill the following requirements:[15]

0. high efficiency for hadronic events from $\Upsilon(4S) \to B\bar{B}$ and from continuum

1. a maximum average trigger rate of $30\,\mathrm{kHz}$

2. a fixed latency of about $5\,\mu\mathrm{s}$

3. a timing precision of less than $10\,\mathrm{ns}$

4. a minimum two-event separation of $200\,\mathrm{ns}$

5. a trigger configuration that is flexible and robust

At SuperKEKB bunch crossing occurs almost continuously, since the radio-frequency (RF) is about $508\,\mathrm{MHz}$ and every second or third period produces an event.[15] The total cross section and trigger rates at a luminosity of $\mathcal{L} = 8 \cdot 10^{35}\,\mathrm{cm}^{-2}\mathrm{s}^{-1}$ for various physics processes is shown in table 4.1.
The luminosity is measured by using Bhabha and $\mathrm{e}^+\mathrm{e}^- \to \gamma\gamma$ events. These events are also used to calibrate the detector response. Due to their high cross section, these events are very dominant. That is also the reason why there is a prescaling factor of 100 on these events. This means that only a predetermined fraction of these events are

Figure 4.1.: Schematic overview of the Belle II trigger system. The four sub-trigger systems send their outputs to the Global Decision Logic. The GDL then performs the final on-line trigger decision. [29]

accepted after satisfying the trigger requirements. After a beam collision, the GDL decides within about $5\,\mu$s if the event should be accepted and if it should be written out. Since the GDL is the first module to make a decision, and since it has no dead time, it is also called Level-1 trigger.[15]

4.2. Data Acquisition System

The data acquisition system (DAQ) reads out the detector signals once the Level-1 trigger decision is given by the trigger system. Starting from the front-end electronics, DAQ transfers the data trough multiple steps of data processing to the storage system.

Table 4.1.: Total cross section and trigger rates for $\mathcal{L} = 8 \cdot 10^{35} \, \mathrm{cm}^{-2}\mathrm{s}^{-1}$ from various physics processes at the $\Upsilon(4S)$.[29]

Physics process	Cross section (nb)	Rate (Hz)
$\Upsilon(4S \to B\bar{B})$	1.2	960
$\mathrm{e}^+\mathrm{e}^- \to$ continuum	2.8	2200
$\mu^+\mu^-$	0.8	640
$\tau^+\tau^-$	0.8	640
Bhabha ($\theta_{\mathrm{lab}} \geq 17°$)	44	350 [a]
$\gamma\gamma$ ($\theta_{\mathrm{lab}} \geq 17°$)	2.4	19 [a]
2γ processes ($\theta_{\mathrm{lab}} \geq 17°, \; p_t \geq 0.1 \, \mathrm{GeV/c}$)	~ 80	~ 15000
Total	~ 130	~ 20000

[a] The rate is pre-scaled by a factor of $1/100$

With the exception of the PXD, all sub-detectors are read out by the unified data link system called the Belle2Link. The working principle of the DAQ can be seen in figure 4.2.
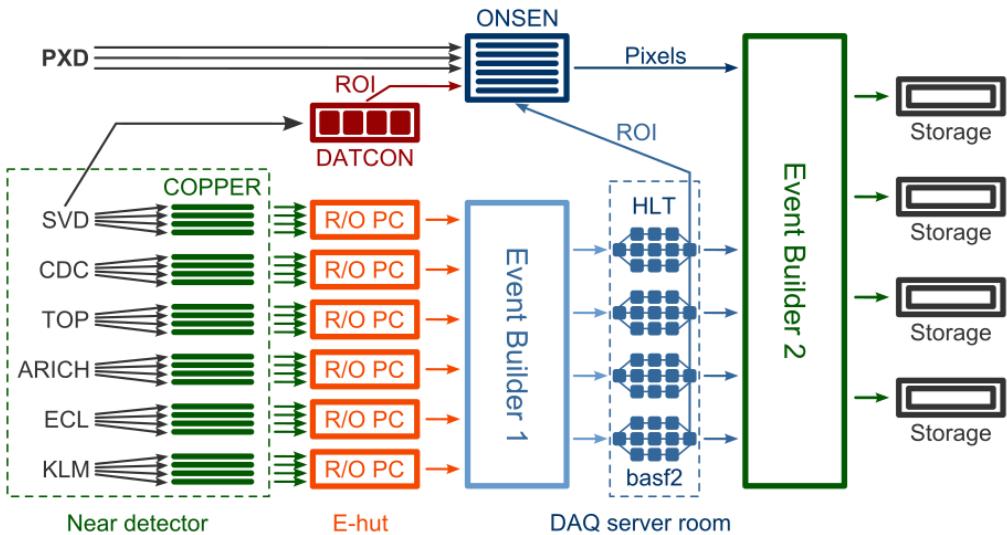

Figure 4.2.: Working principle of the Belle II DAQ. The data is transferred by about 300 COPPER boards to about 30 R/O PCs. The data is then put together by the first event builder and the events are reconstructed by the HLT afterwards. The HLT contains $O(10)$ units with about 400 cores each. Then the reconstructed data is merged with the data coming from the PXD. Finally, the data is saved on about 10 storage units. [30]

The first part of the Belle2Link is the common readout platform (COPPER). This platform transforms the different data formats coming from the sub-detectors into a common data format. The COPPER boards then send their output signal to the event builder, which merges the data coming from the same collision to an event. With the information from the fully reconstructed events, the high level trigger (HLT) is able to finally decide whether the event should be stored or not. If the event should be recorded, it is then merged with the information coming from the PXD data in the second event builder.
Once the PXD receives the trigger signal, the readout starts. These data are stored on on-line selector nodes for up to $5\,\mathrm{s}$. Meanwhile, the HLT performs the event reconstruction. Based on information coming from the SVD and CDC, the charged tracks, reconstructed in the HTL, are transferred back to the PXD and regions of interest (ROI) are formed. Only pixels of the PXD within the ROI are kept and considered in the second event builder. Complementary to the HLT, the data concentrator also searches for ROIs. The HLT is optimized for high momentum and the data concentrator is optimized for low momentum particles. Both systems require hits in all SVD layers. [15]

4.3. Basf2

The software framework used at Belle II is called Basf2 (Belle AnalysiS Framework). It is designed to perform off-line and analysis tasks. The majority of the code is written in C++, but python scripts are used for framework execution. The user specifies a sequence of modules in the python steering file which then process events. It also provides access to external libraries like ROOT which allows processing, statistical analysis, visualization and storage of common data and Geant4 for simulating the full detector.[31]
For the off-line reconstruction to work it has to take into account that the Belle II detector consists of a set of sub-detectors. Each sub-detector has a different geometry, dimension and is made out of different materials buried in a magnetic field. It also exploits the informations on the interactions of the particles with the matter. This information is then used to reconstruct the particle trajectories and the signal they generate in the detectors. This is done using algorithms that model particle propagation.

5 Bhabha Kinematics At Belle II

IN chapter 3 we saw that at Belle II the electron and the positron beams have different energies. Additionally, both beams are colliding with each other under an angle of 1.26°. Therefore, it is interesting to look at the Bhabha kinematics in the lab system of Belle II.
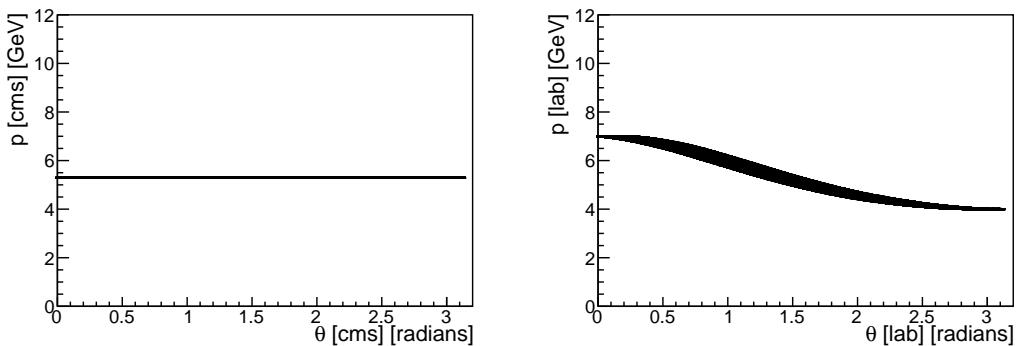

Figure 5.1.: Bhabha scattering in different frames. Left: The momentum of the outgoing particles in a Bhabha process as function of the polar angle θ in the CMS frame is shown. In the CMS frame the particle has the same energy for every value of θ. Right: The momentum of the outgoing particles in a Bhabha process as function of the polar angle θ in the lab frame is shown.

The left plot of figure 5.1 shows the momentum of the outgoing Bhabha particles as function of the polar angle θ in the center-of-mass frame. Since the incoming electron and the positron have the same mass and they are colliding with the same energy, the outgoing particles always have the same momentum independent of the scattering angle in the center-of-mass frame. In the right plot the momentum of the outgoing Bhabha particles after the boost in the lab system is shown. For small θ a higher momentum of the outgoing particles is expected compared to high θ. The width spread of the distribution at fixed θ is caused by the fact that the beams are colliding with each other under an angle at Belle II.

Figure 5.2.: The transverse momentum of the outgoing Bhabha particles in different frames. Left: The transverse momentum of the outgoing particles in a Bhabha process as function of the polar angle θ in the CMS frame is shown. The highest transverse momentum is expected at $\theta \approx \pi/2$. Right: The transverse momentum of the outgoing particles in a Bhabha process as function of the polar angle θ in the lab frame is shown. The highest transverse momentum is shifted a little bit to smaller values of θ.

Figure 5.2 shows the transverse momentum as function of θ for the outgoing Bhabha particles at Belle II. The left plot shows the distribution in the center-of-mass frame, while the right plots shows it for the lab frame. In both frames we expect the highest transverse momentum at a polar angle θ of about $\pi/2$.
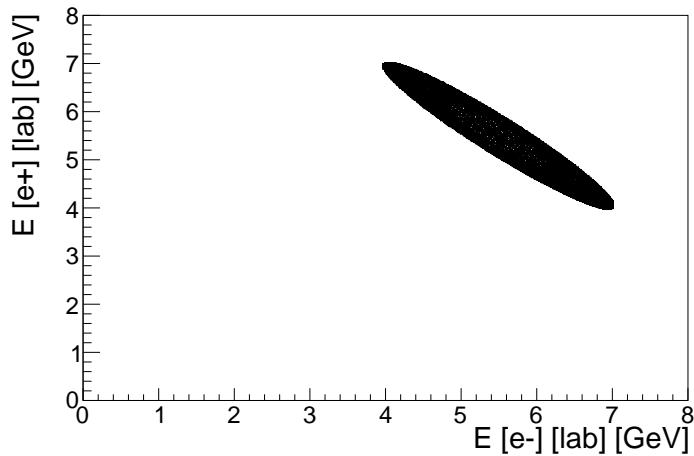

Figure 5.3.: The energies of the two outgoing Bhabha particles in the lab frame at Belle II.

In figure 5.3 the energy of the outgoing Bhabha particles in the lab frame at Belle II are plotted against each other. For example if the electron has an energy of 7 GeV than the positron will have an energy of just about 4 GeV and vice versa.

CHAPTER

6 Preparation For Calculating The Tracking Efficiency Of Phase2

THIS chapter will provide an overview on how the cuts where chosen and which selection was applied in order to calculate a reasonable tracking efficiency on phase2. We will start with a definition of the tracking efficiency we want to calculate. Then the reconstruction and selection of the Bhabha events using only ECL informations will be described. The same selection and cuts used on phase2 will also be used on phase3 later on. During phase2, a test run to optimize the accelerator and to understand the detector better, only a fraction of the VXD was installed. For phase3, the first physics run of Belle II, the complete SVD and most of the PDX were installed.
Phase2 MC will be shown in green and phase2 data in brown.

6.1. Phase2

Phase2 data were taken in the time between March 2018 and July 2018. During this time, only a small azimuthal fraction of the vertex detector was installed at $\phi \approx 0$. A sketch of the installed VXD can be found in the appendix figure A.18. The main focus of this phase was to study the background of the newly installed Belle II detectors, in order to be certain that the operation of the vertex detector is compatible with the much higher luminosity expected for physics data taking. Additionally, hardware controls were tested in this phase.

6.2. Definition Of Tracking Efficiency

First of all, a definition of efficiency has to be declared, since there are several ways to define a tracking efficiency. The physics case we are considering is the Bhabha process $e^+e^- \to e^+e^-$. As described in chapter 3, charged particles leave a track in the detector. Therefore, when we look at an outgoing particle of a Bhabha process with a track, then we know that the other particle should also have a track. If the other particle has no track associated, then this is an inefficiency. If both outgoing particles have a track associated, then this is the efficient case.

The particle we investigate will be called *probe*. The other particle will be called *tag*. We know that *tag* is always reconstructed as a charged particle. Thus, we will calculate the efficiency for two different cases:

- Electron Tracking Efficiency: *tag* is reconstructed as a positron

- Positron Tracking Efficiency: *tag* is reconstructed as an electron

So for this work, we will use the following definition for the tracking efficiency:

$$\epsilon = \frac{\text{Number of times } probe \text{ is reconstructed as a charged particle}}{\text{Total number of } probe \text{ particles}} \tag{6.1}$$

To calculate an efficiency according to equation 6.1 one needs two histograms. One histogram filled with *probe* information when *probe* is reconstructed as a charged particle and a histogram filled with information from all *probe* particles. The first will be referred to as *enumerator* histograms and the later will be referred to as *denominator* histograms.

6.3. Reconstructing Bhabha Events With Basf2

To analyze a Monte Carlo or data file, a python script using Basf2 has to be written. The following code is a simplified version of the steering file I wrote. The whole steering file is located on KEKCC at:
/home/belle2/msobotzi/bhabha/bhabha_vpho.py

The goal of this steering file is to reconstruct the virtual photon in a Bhabha event. This virtual photon decays into two daughters which then hit the ECL. Since we want to calculate the tracking efficiency, we need to be able to reconstruct the virtual photon from two daughters both associated with a track, and two daughters one associated with a track (reconstructed as a charged particle by the framework) and one with no track associated (reconstructed as a photon by the framework).
The same steering file is used for data and MC.

```
1  fillParticleList('gamma:all', 'clusterE > 0.01', path=mypath)
   fillParticleList('e+:all', 'clusterE > 0.01', path=mypath)
3
   reconstructDecay('vpho:gamma -> gamma:all', '', path=mypath)
5  reconstructDecay('vpho:elec -> e+:all', '', path=mypath)

7  copyLists(outputListName = 'vpho:ECLObjectUnranked', inputListNames=['
       ↪ vpho:elec', 'vpho:gamma'], path=mypath)

9  rankByHighest('vpho:ECLObjectUnranked', 'daughter(0,clusterE)', path=
       ↪ mypath)
```

```
cutAndCopyList('vpho:ECLObject', 'vpho:ECLObjectUnranked', '', path=
    ↪ mypath)

reconstructDecay('vpho:bhabha -> vpho:ECLObject vpho:ECLObject', '',
    ↪ path=mypath)

variablesToNtuple('vpho:bhabha', variables, treename = 'vpho_bhabha',
    ↪ filename = output.root, path=mypath)
```

In the first line of code all particles which hit the ECL and have no associated track are filled into a photon list called `gamma:all`. The clusters created by those particles must have a cluster energy in the ECL (clusterE) of at least 0.01 GeV. In the second line a list called `e+:all` is created. All particles with an associated track are filled in this list. Thus, this list contains e.g. electrons, positrons and even muons. So, a cut on the cluster energy makes more sense compared to a cut on the energy of the particles.

Due to the fact that we want to calculate a tracking efficiency, we need to somehow combine the `e+:all` and the `gamma:all` lists. As mentioned earlier, we need to be able to reconstruct the virtual photon from particles reconstructed as electrons/positrons and photons. Unfortunately, the Basf2 framework prevents a combination of two different particle lists, like `e+:all` and `gamma:all`. Therefore, we need to use a trick. This is shown in lines 4 and 5. In line 4 we tell the framework that the reconstructed photon is the only daughter of a virtual photon called `vpho:gamma`. The same is done for the electron list in line 5. Here the virtual photon is called `vpho:elec`.

Now, these two lists can be combined to one list called `vpho:ECLObjectUnranked`. This is done in line 7.

In line 9 and 10 the daughters in the `vpho:ECLObjectUnranked` list are sorted by their cluster energy and filled in a new list called `vpho:ECLObject`.

In line 12 the virtual photon of the Bhabha event is reconstructed from the ECL objects in the `vpho:ECLObject` list. The number of reconstructed virtual photon candidates per event n_cand can be calculated by the following equation[32]:

$$n_\text{cand} = \frac{n_\text{p}(n_\text{p} - 1)}{2} \tag{6.2}$$

n_p is the number of reconstructed particles per event. Equation 6.2 is also known as the equation to calculate *triangular numbers*. For example, if five ECL particles are reconstructed in a single event then ten virtual photon candidates are reconstructed according to equation 6.2. Since we only expect one virtual Bhabha photon per event, we have to select the best candidate in each event. This will be done in section 6.4.

Since the entries in the `vpho:ECLObject` list are sorted by their cluster energy, the first daughter of the reconstructed virtual Bhabha photon always has a higher cluster energy compared to the second daughter. The first daughter will be referred to as *HclE* (High cluster Energy) and the second daughter as *LclE* (Low cluster Energy).

As illustrated in figure A.1, the HclE daughter has always a higher energy compared to the LclE daughter. Here the clusterE(LclE) is subtracted from the clusterE(HclE) and only positive values remain. Therefore, HclE is the daughter with the higher cluster energy.

Finally, in the last line of code, all variables of the candidates like mass, momentum, cluster energy of each daughter, does the daughter have a track and so on are written out in a tree called `vpho_bhabha` in a file with the name `outputname`. This name depends on whether the steering file is running on data or MC.

6.4. Best Candidate Selection On Phase2 Monte Carlo

We use Monte Carlo simulation due to the fact that on MC we know everything about the generated and reconstructed particles. Thus, on MC it is possible to select only Bhabha events which pass the tracking detectors and with this knowledge we can introduce cuts in such a way that we reconstruct only these Bhabha events. To calculate a tracking efficiency it is extremely important to select solely Bhabha events. At first, we are running on only one $e^+e^- \rightarrow e^+e^-$ MC file.

6.4.1. CDC-Cut

Due to the fact that charged particles are reconstructed using information coming from the inner tracking detectors, we are only interested in events which pass these detectors. Thus, we apply a selection on the polar angle θ on the generated daughters (generated daughters means the true generated Monte Carlo daughters). This cut has to be introduced since the ECL has a wider θ detection range compared to the tracking detectors.[1] Therefore, some outgoing charged particles are detected by the ECL but they did not pass the tracking detectors. Events containing these particles would always be labeled as inefficient events. The tracking detectors have a polar angle region of:

$$17.0° < \theta_{\text{HclE, LclE}} < 150.0° \tag{6.3}$$

All of the events which survive this cut are written into a list (*mcEvtCDC*). The cut was named after the CDC because it was the only completely installed tracking detector during phase2. We know that the Monte Carlo file contains 140000 generated Bhabha events. After this cut only 24286 Bhabha events remain. In section 2.3.1 we saw that Bhabha events have a very high cross section in forward and backward direction. Thus, we expect that a lot of the generated daughters do not pass the CDC.

Now we will take a look at the reconstructed Monte Carlo events. All of these reconstructed events have to appear in the mcEvtCDC list because we know that only in these events both daughters are passing the CDC. A total of 24100 events have at least one reconstructed candidate.

[1]The ECL covers a polar angle region of $12.4° < \theta < 155.1°$
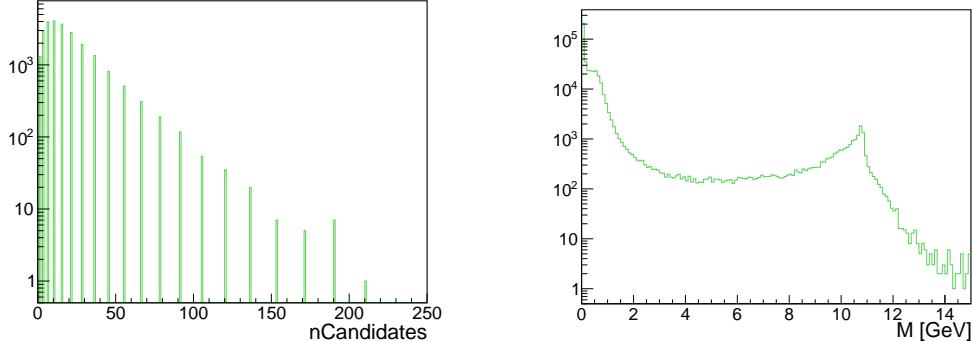
Figure 6.1.: Left: The number of reconstructed candidates per event is shown. We select 24100 events. Right: The invariant mass of the reconstructed candidates is shown. We reconstruct 417899 candidates.

In figure 6.1 on the left, we see the number of reconstructed candidates per event. Since we do not have a cut on the reconstruction, the number of reconstructed candidates n_{cand} follows equation 6.2. On the right we see the invariant mass of the reconstructed candidates. Note that we are now looking at candidates and as we can see on the left we oftentimes have more than one candidate per event. Therefore, the numbers of entries for the reconstructed invariant mass is way higher then for the number of candidates per event. Consequently, we need some cuts to select the best candidate in each event and thereby reduce the number of candidates per event to one.

6.4.2. Mass-Cut

The first cut to reduce the number of reconstructed candidates per event is a mass cut (The cut is called M). As we saw in figure 6.1, a lot of candidates are reconstructed with a low invariant mass and we know from section 3 that the invariant mass of the $e^+e^- \rightarrow e^+e^-$ events should be around $10.58\,\mathrm{GeV}$. The lower-mass cut of $8\,\mathrm{GeV}$ is rather loose.
As can be seen in figure 6.2 on the right, all reconstructed candidates with an invariant mass below $8\,\mathrm{GeV}$ are neglected. Therefore, the number of candidates per event is reduced drastically. This is illustrated in the left plot. However, sometimes we still have two candidates per event and consequently, we have to introduce some more additional cuts.

6.4.3. Additional Cuts

To reduce the number of candidates per event to one, some additional cuts are needed. Sometimes it can happen that two reconstructed particles are associated to one Monte Carlo particle. Some examples of this effect can be seen in table 6.1.
This table shows that the generated energy (mcE) for both HclE and LclE is the same and the reconstructed energy (E) of the HclE and the LclE particle sum up roughly
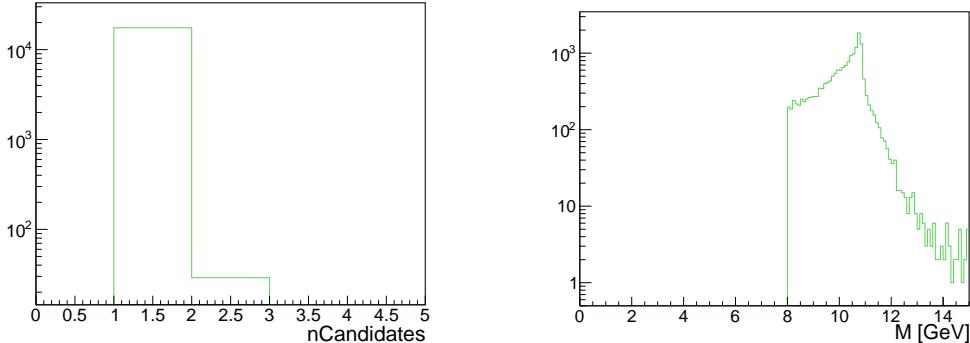
Figure 6.2.: A cut on the invariant mass is applied. The reconstructed invariant mass has to be bigger than 8 GeV. Left: The number of reconstructed candidates per event is shown. We select 17539 events. Right: The invariant mass of the reconstructed candidates is shown. We reconstruct 17558 candidates.

Table 6.1.: Some examples for events with cluster splitting. mcE is the same for LclE and HclE. The energies are in GeV.

Event Number	HclE				LclE			
	E	mcE	PDG	mcPDG	E	mcE	PDG	mcPDG
41890065	0.9432	4.1278	11	11	3.1900	4.1278	22	-11
41890118	1.5993	4.3465	22	11	2.6462	4.3465	-11	-11
41890668	3.1758	6.8878	22	-11	3.1059	6.8878	11	11
41891214	2.3290	6.1585	22	-11	3.9079	6.1585	11	11
41892596	1.4193	4.2997	22	11	2.9673	4.2997	-11	-11

to their respectively mcE. This table also shows that the generated particle is always an electron or positron and that the *additionally* reconstructed particle is always a photon.

In figure 6.3 the angular distributions of this effect can be seen. For these plots no cuts on the reconstruction were applied. It was just checked if exactly two reconstructed particles have the same generated Monte Carlo particle associated. Then the cluster-Phi (ϕ_{cluster}) and clusterTheta (θ_{cluster}) values of these particles were filled into their histograms. The left plot shows that both reconstructed particles have the same angle θ_{cluster}. The right plot shows that they have a slightly different angle ϕ_{cluster}. Therefore, the *original* cluster is separated into two clusters with the same angle θ_{Cluster} and a different angle ϕ_{cluster}. One cluster is associated with a track produced by the generated particle and for the other cluster no track is left, therefore, it is labeled as a photon. This effect will be referred to as *cluster splitting*.

The energy of the particles in a cluster splitting process can be seen in figure 6.4. Since we only want to select Bhabha events, we want to neglect these kinds of events.
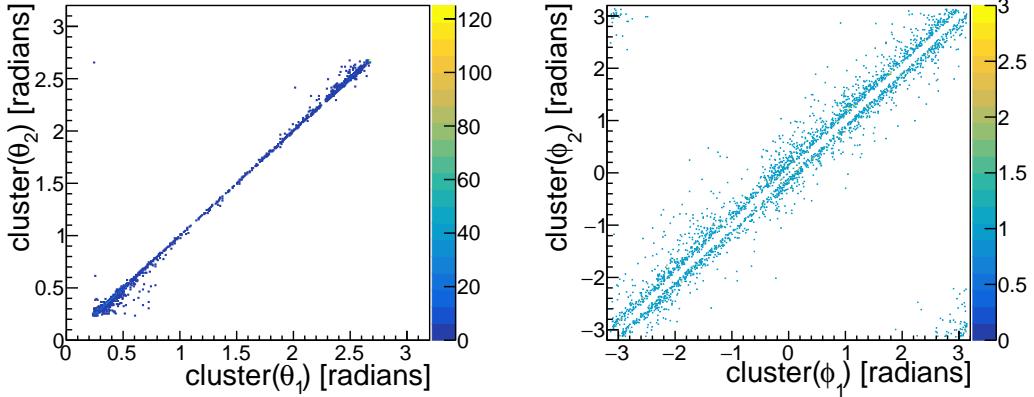
Figure 6.3.: Left: The polar angle $\theta_{\mathrm{Cluster}}$ of the clusters after the *cluster splitting*. Almost all the time, both clusters have the same polar angle $\theta_{\mathrm{Cluster}}$. Right: The azimuthal angle ϕ_{Cluster} of the clusters after the *cluster splitting*. The angle ϕ_{Cluster} of both clusters are always slightly different. Therefore, *cluster splitting* always occurs along the polar angle.
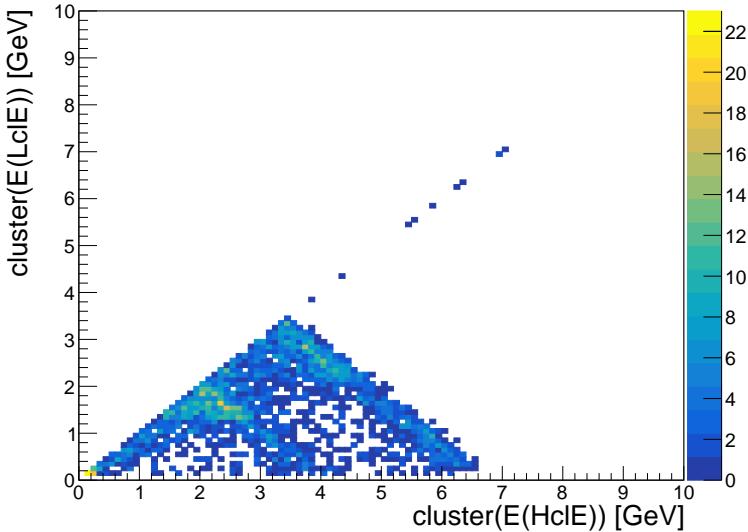

Figure 6.4.: Cluster Energy(HclE) vs. Cluster Energy(LclE) in the case that both particles are associated to the same Monte Carlo particle. Here, no cuts are applied. The total number of entries is 2891.

In section 5 we saw that the particles have an energy of at least 4 GeV. Therefore, we are able to apply a cut on the cluster energy. We are now requiring a cluster energy

of at least 3.5 GeV (The cut is called `MclE`). This cut also contains the mass cut `M`. With this cut almost all events with cluster splitting should be neglected.

Next, we require that we have exactly two clusters per event, each with an energy of at least 3.5 GeV, since we only expect two high energetic particles in the ECL. Additionally, due to the kinematics at Belle II, we can require that one of the outgoing particles has to have a cluster energy of at least 4.5 GeV. (The cut is called `MclE2H` and contains both previously introduced cuts.) This is required due to the trigger cut we will add in section 6.7.

As an additional safety net, a cut on the number of reconstructed tracks per event is applied. On data it can happen that there are way more than two tracks reconstructed in an event. To select only *clean* events we apply a cut on the number of reconstructed charged particles per event (The cut is called `MclE2HnT`). This number should not be greater than six. It contains all of the previously introduced cuts.

Table 6.2.: Some examples for events with too much energy in the ECL.
Note: Here the energy of the particles is shown not clusterE. The mass and the energies are in GeV.

Event Number	M	Energy(`HclE`)	Energy(`LclE`)	Total Energy ECL
41890917	30.6657	33.8368	7.2455	41.0823
26574414	108.4056	235.3918	13.0644	248.4563
21222871	11.6553	2.1733	15.6648	17.8381
26372406	10.3229	0.2465	190.2663	194.5971

Table 6.2 shows that sometimes the invariant mass of the reconstructed candidates is way higher than 10.58 GeV. To neglect these candidates an upper cut on the reconstructed invariant mass is introduced. Now the reconstructed invariant mass also has to be smaller than 12 GeV.

Additionally, sometimes the total energy in the ECL is way higher than expected. To exclude these events an upper cut on the total energy per event in the ECL is added (The cut is called `MclE2HnTSumE`). The total energy in the ECL must not exceed 15 GeV. Again, this cut includes all previously mentioned cuts.

After applying all mentioned cuts, the number of reconstructed candidates per event is shown in figure 6.5. It shows that now we only select one virtual photon candidate per event. Therefore, we select 14545 events and reconstructed candidates.

There is no cut on the reconstructed position of the interaction point since this would require a backtracking of the particles. To backtrack a charged particle, information from the tracking detectors are used and this can not be done since we want to use ECL information only.
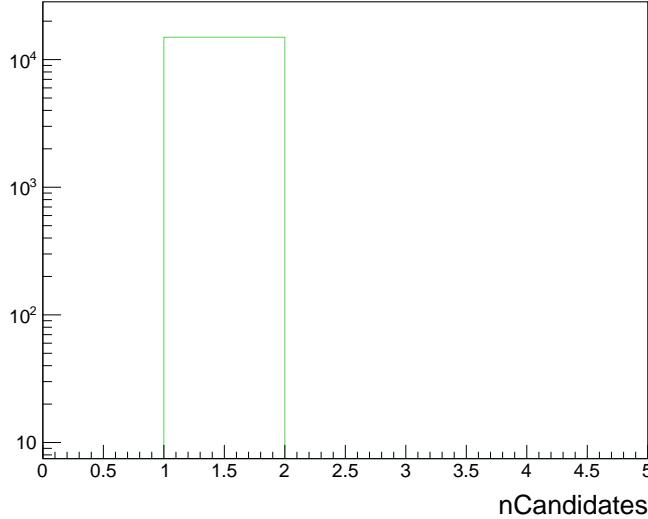
Figure 6.5.: Number of candidates per event after applying all cuts for a single phase2 MC file. $n = 14545$

6.4.4. Cut Efficiency

In this section we want to discuss different efficiencies of the previously introduced cuts. We will take a look at the relative and the total efficiency. The results can be seen in table 6.3.

$$\epsilon_{\text{tot}} = \frac{n_{\text{cut}}}{n_{\text{total}}} \tag{6.4}$$

To calculate the total efficiency of a cut we have to use equation 6.4. Here the number of events after a cut n_{cut} is divided by the total number of events n_{total} before all cuts[2].

$$\epsilon_{\text{rel; Cut B}} = \frac{n_{\text{Cut B}}}{n_{\text{Cut A}}} \tag{6.5}$$

Equation 6.5 shows the equation used to calculate the relative efficiency. To calculate the relative efficiency of cut B we have to divide the number of events after cut B by the number of events after the previous cut A. The relative efficiency with no cut is defined to be 1.

Table 6.3 shows the relative and total efficiency of the cuts. After applying all of the cuts, a total of about 62% of the generated Bhabha events are reconstructed (both outgoing particles of the Bhabha event have to pass through to CDC). [3]

---

[2]The cut that requires that the generated particles have to pass the CDC is still applied → $n_{\text{total}} = 24100$

[3]Originally, the file contained 140000 Bhabha events. In the end only about 10 % of them were reconstructed

Table 6.3.: A table with the total number of events after the respective cuts. Also the relative and the total efficiency of these cuts are shown. The total number of entries in the *mcEvtCDC*-list is 24286.

Cut	Number Of Events	Relative Efficiency	Total Efficiency
No Cut	24100	1.0000	1.0000
M	17529	0.7273	0.7273
MclE	14903	0.8502	0.6183
MclE2H	14896	0.9995	0.6180
MclE2HnT	14896	1.0000	0.6180
MclE2HnTSumE	14545	0.9764	0.6035

6.4.5. No MC-Truth Information

In the previous sections we saw that we are able to select only one candidate in a Bhabha event under the condition that we know that the true properties of these particles. However, we do not have this information on phase2 data. Therefore, we also have to check how many candidates we reconstruct if we do not have MC-Truth information. We will analyze the same MC-file as before to compare the number of reconstructed events.
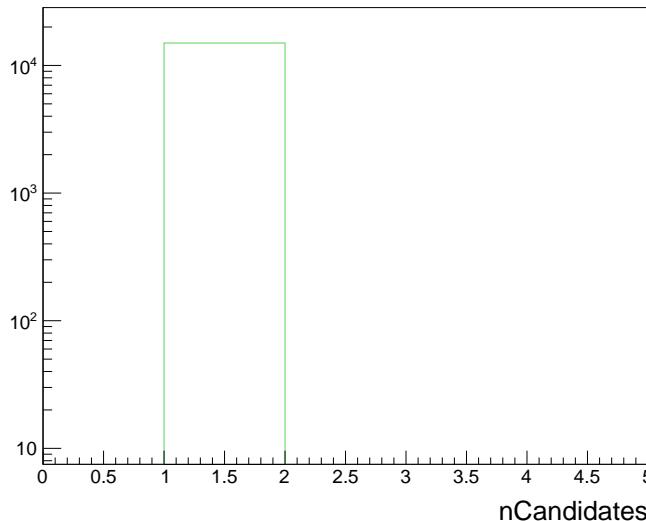
Figure 6.6.: Number of candidates per events with no MC-Truth information and all cuts. Same MC file as before. We also select just one reconstructed candidate per event. The total number of selected events is 14581.

In figure 6.6 we see that we reconstruct a total number of 14581 events. Therefore, we reconstruct only 36 events more with no MC-Truth information. Additionally, we are still able to select only one reconstructed candidate per event.

Since we only reconstruct a few more events and still only one candidate per event, we can be very confident that we only select almost exclusively Bhabha events.

6.5. Best Candidate Selection on Phase2 Data

Up until now we only ran on phase2 MC, but ultimately we want to calculate the tracking efficiency of phase2 data. Therefore, we have to test the selection also on phase2 data. The same steering file as described in section 6.3 is used and run over a single phase2 data file.
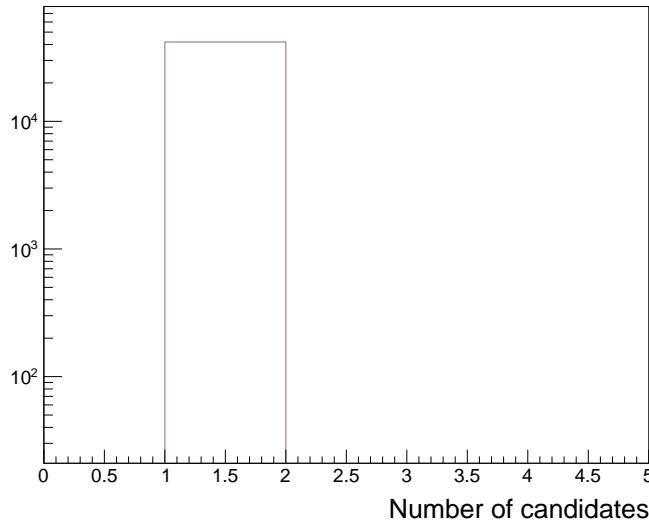
Figure 6.7.: Number of candidates per event for phase2 data. All introduced cuts are applied. We also select only one candidate per event on phase2 data. A total number of 41853 events and candidates is selected.

Figure 6.7 shows the number of reconstructed candidates on phase2 data after the `MclE2HnTSumE` cut. As illustrated in this figure, we reconstruct only one candidate per event even on phase2 data.

6.6. Selecting Bhabha Events

Now, that we are satisfied with the selection of events and candidates we need to be sure that we only select $e^+e^- \rightarrow e^+e^-$ events and not for example $e^+e^- \rightarrow \gamma\gamma$ events. This is important on phase2 data. On phase2 MC there are no $e^+e^- \rightarrow \gamma\gamma$ events because only $e^+e^- \rightarrow e^+e^-$ events are generated. To do this we can use the so-called b2b-variable (back-to-back).
A simplified sketch on how to calculate the b2bClusterPhi ($\phi_{\mathrm{pred,b2bcl}}^{\mathrm{LclE}}$) variable for the LclE particle is shown in figure 6.8. This sketch shows the ECL in beam direction,
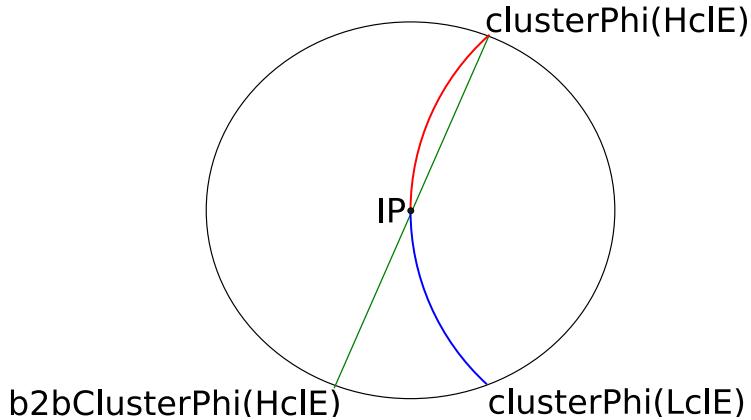
Figure 6.8.: Simplified representation of the b2bClusterPhi variable in the transverse plane of the detector. The track of charged particles are bent in the detector. The colors have no deeper meaning.

so the magnetic field in the ECL is pointing into the paper. At the interaction point an electron (in this example the red line) and a positron (in this example the blue line) are created. Since both particles are charged their trajectories are bended by the magnetic field. The electron hits the ECL and creates a cluster with an azimuthal cluster angle $\phi_{\text{Cluster}}^{\text{HcL}}$. As described in section 5 the center-of-mass frame at Belle II has a non zero x-y fraction. Therefore, the variable $\phi_{\text{pred,b2bcl}}^{\text{LclE}}$ is not just $\phi_{\text{Cluster}}^{\text{HclE}} - \pi$ (as in the sketch). To calculate $\phi_{\text{pred,b2bcl}}^{\text{LclE}}$ we have to boost the particle in the center-of-mass frame then calculate $\phi_{\text{CMS}}^{\text{HclE}} - \pi$ and finally we have to boost it back in the lab frame. With this variable we can predict the azimuthal angle of the cluster of the other particle.

This sketch shows that there is a difference between the predicted cluster angle $\phi_{\text{pred,b2bcl}}^{\text{LclE}}$ (calculated with informations from the electron) and the reconstructed cluster angle $\phi_{\text{Cluster}}^{\text{LclE}}$ of the positron due to the magnetic field. This also means that in an $e^+e^- \to \gamma\gamma$ event, the predicted and the reconstructed cluster angles are the same because the trajectory of photons are not bend in the magnetic field. Therefore, we are able to differ between $e^+e^- \to e^+e^-$ and $e^+e^- \to \gamma\gamma$ events.

In figure 6.9 the difference between the predicted and the reconstructed cluster angle ($\Delta\phi_{\text{pred - reco}}$) for phase2 data is shown. In the left plot the reconstructed angle $\phi_{\text{Cluster}}^{\text{LclE}}$ angle of the LclE particle is subtracted from the angle $\phi_{\text{pred,b2bcl}}^{\text{LclE}}$ calculated with informations from the HclE particle (the resulting angle difference is called $\Delta\phi_{\text{pred - reco}}^{\text{LclE}}$). In the right plot it is vice versa. There are three peaks in both plots. The middle peak is created by $e^+e^- \to \gamma\gamma$ events since the predicted and the reconstructed cluster angles are the same. Thus, these are events we want to cut away. The left peak is caused by electrons (most of the HclE particles are electrons, therefore, the left peak on the right plot is significantly higher[4]), the right peak by

---

[4]As described in section 6.3, the HclE daughter is the daughter with the higher cluster energy
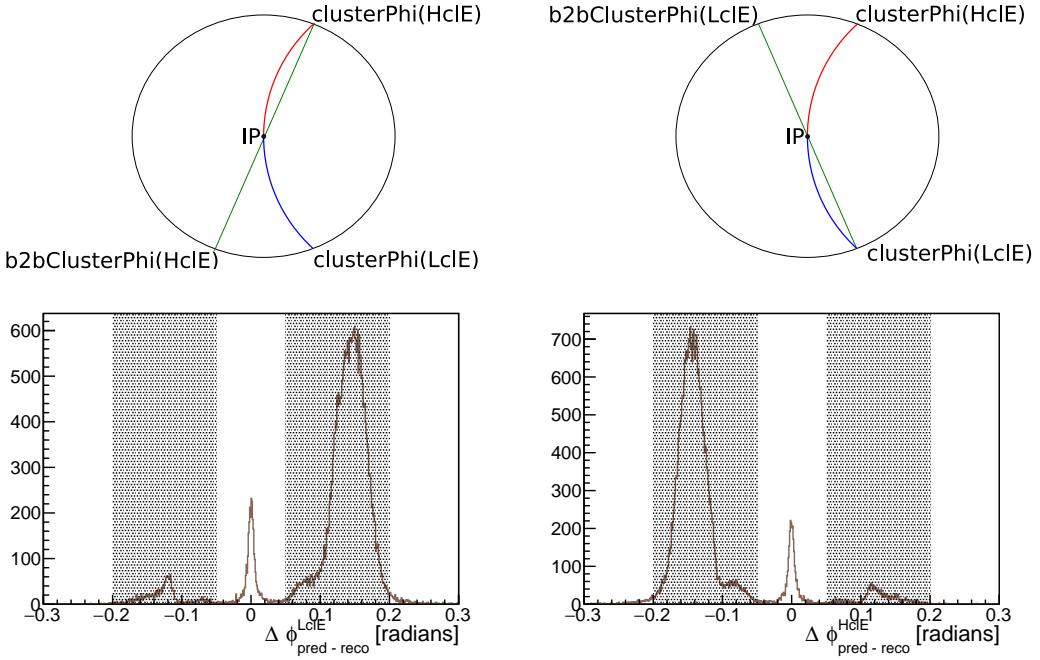
Figure 6.9.: Left: $\Delta\phi^{\text{LclE}}_{\text{pred-reco}}$. Right: $\Delta\phi^{\text{HclE}}_{\text{pred-reco}}$. Only particles within the gray area are taken into account. The two top sketches represent what is calculated. The middle peak in both plots are created by $e^+e^- \to \gamma\gamma$ events.

positrons. This means that if e.g. we only cut on the left peak we are only selecting electron particles even if they are wrongly reconstructed as photons, using ECL information only. Therefore, the last cut we will add is a cut on $\Delta\phi_{\text{pred-reco}}$. We will only consider events with:

$$0.05 \le |\Delta\phi^{\text{LclE}}_{\text{pred-reco}}| \le 0.2 \text{ and } 0.05 \le |\Delta\phi^{\text{HclE}}_{\text{pred-reco}}| \le 0.2$$

A special case occurs for $\phi \approx \pi$ or $\phi \approx -\pi$. It can happen that the angle ϕ_{Cluster} is around π but the angle $\phi_{\text{pred,b2bcl}}$ is calculated to be around $-\pi$, then the difference between the predicted cluster angle $\phi_{\text{pred,b2bcl}}$ and reconstructed cluster angle ϕ_{Cluster} is around 2π. This can be seen in figure A.2
Finally, the $\Delta\phi_{\text{pred-reco}}$ cut can be summarized in the following three conditions. Each event has to fulfill one of them to be taken into account.

(a) $0.05 \le |\Delta\phi^{\text{LclE}}_{\text{pred-reco}}| \le 0.2$ and $0.05 \le |\Delta\phi^{\text{HclE}}_{\text{pred-reco}}| \le 0.2$

(b) $2\pi - 0.2 \le |\Delta\phi^{\text{LclE}}_{\text{pred-reco}}| \le 2\pi - 0.05$ and $0.05 \le |\Delta\phi^{\text{HclE}}_{\text{pred-reco}}| \le 0.2$

(c) $0.05 \le |\Delta\phi^{\text{LclE}}_{\text{pred-reco}}| \le 0.2$ and $2\pi - 0.2 \le |\Delta\phi^{\text{HclE}}_{\text{pred-reco}}| \le 2\pi - 0.05$

These cuts are visualized by the gray area in figure 6.9 and A.2. Only particles within these areas are taken into account.
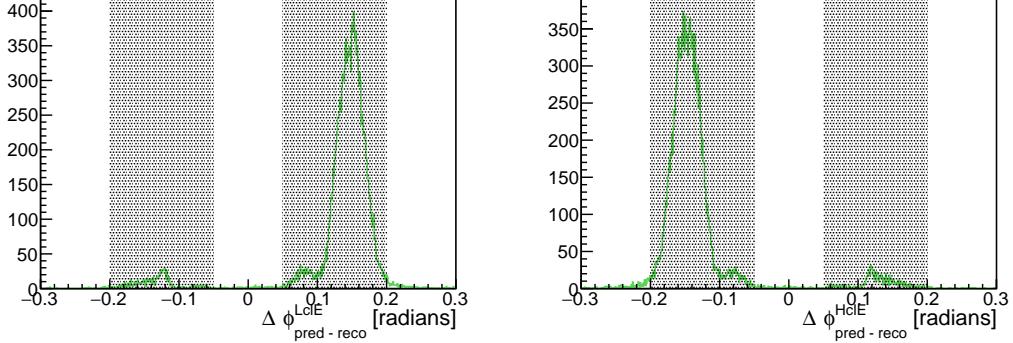
Figure 6.10.: Left: $\Delta\phi^{\mathrm{LclE}}_{\mathrm{pred-reco}}$. Right: $\Delta\phi^{\mathrm{HclE}}_{\mathrm{pred-reco}}$. Only particles within the gray area are taken into account. Both plots are created with phase2 MC. There is no middle peak because only ee $\rightarrow$ ee events were generated.

Figure 6.10 shows the same plots as figure 6.9 but with phase2 MC. Note that there is no middle peak because only $\mathrm{e^+e^-} \rightarrow \mathrm{e^+e^-}$ events were generated. In figure A.3 the same plots but with full range are shown for phase2 MC.

Later we will present the efficiencies as function of $\phi_{\mathrm{pred,b2b}}$ and $\theta_{\mathrm{pred,b2b}}$. $\phi_{\mathrm{pred,b2b}}$ is the true predicted azimuthal angle of the *probe* particle. It is calculated similar to the angle $\phi_{\mathrm{pred,b2bcl}}$ but the charges of the particles are taken into account. (The same is true for the angle $\theta_{\mathrm{pred,b2b}}$.) This means that e.g. $\phi^{\mathrm{LclE}}_{\mathrm{pred,b2b}}$ is equal to the reconstructed polar angle of the LclE particle in the case that LclE is reconstructed as a charged particle.

Figure 6.11.: Left: $\Delta\phi^{\mathrm{LclE}}_{\mathrm{True(pred)-reco}}$. Right: $\Delta\phi^{\mathrm{HclE}}_{\mathrm{True(pred)-reco}}$. Both plots are created with phase2 MC. The side peaks are created by inefficiencies.

In figure 6.11 in the left plot, $\phi^{\mathrm{LclE}}_{\mathrm{cluster}}$ is subtracted from $\phi^{\mathrm{LclE}}_{\mathrm{pred,b2b}}$ (the angle difference is called $\Delta\phi^{\mathrm{LclE}}_{\mathrm{True(pred)-reco}}$). The small side peak is created by inefficiencies. As mentioned,

the charges of the particles are taken into account while predicting the true angles. The azimuthal angle of an uncharged particle corresponds to the reconstructed azimuthal cluster angle. On the other hand, the azimuthal angle of a charged particle corresponds to the azimuthal angle of the particle before it was bend by the magnetic field. Thus, if there is an inefficiency then the *probe* particle is reconstructed as an uncharged particle and then the predicted and the reconstructed angles differ a bit, because the azimuthal angle of the reconstructed cluster is used instead of the azimuthal angle the particle had before it was bent by the magnetic field. The right plot shows the difference between $\phi_{\text{pred,b2b}}^{\text{HclE}}$ and $\phi_{\text{cluster}}^{\text{HclE}}$.
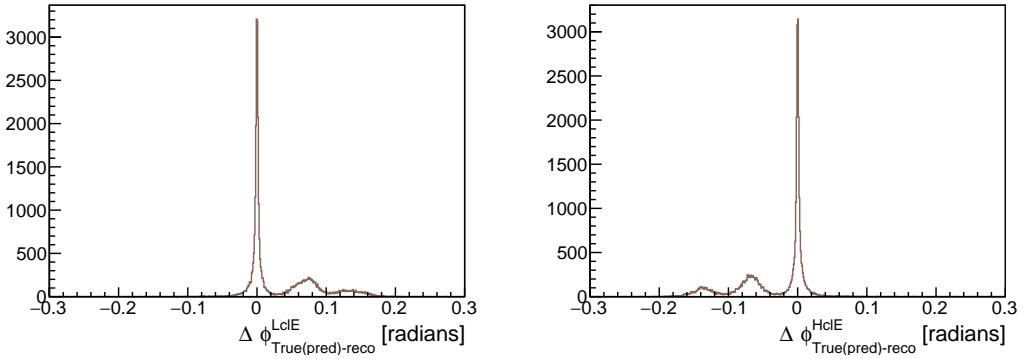
Figure 6.12.: Left: $\Delta\phi_{\text{True(pred)}-\text{reco}}^{\text{LclE}}$. Right: $\Delta\phi_{\text{True(pred)}-\text{reco}}^{\text{HclE}}$. Both plots are created with phase2 data. The peaks at $|\Delta\phi_{\text{True(pred)}-\text{reco}}| \approx 0.08$ are created by inefficiencies. The peaks at $|\Delta\phi_{\text{True(pred)}-\text{reco}}| \approx 0.16$ are created when the *tag* particle is reconstructed as the wrong charged particle.

Figure 6.12 shows the same plots as figure 6.11 but with phase2 data. Similar to figure 6.11, the peaks at $|\Delta\phi_{\text{True(pred)}-\text{reco}}| \approx 0.08$ are created by inefficiencies. The peaks at $|\Delta\phi_{\text{True(pred)}-\text{reco}}| \approx 0.16$ are created when the *tag* particle is reconstructed as the wrong charged particle. For example, if the *tag* particle is an electron but it is reconstructed as a positron, then $\phi_{\text{pred,b2b}}$ is calculated under the assumption that the *probe* particle is an electron.

The $\Delta\theta_{\text{True(pred)}-\text{reco}}$ plots can be found in the appendix in figure A.4 (phase2 MC) and A.5 (phase2 data).

6.7. ECL-Trigger

Last but not least, we need to be sure that each event has a trigger signal coming from the ECL. Otherwise, the trigger signal could come only from the tracking detectors. Then, there would be a bias on the efficiency, since the tracking detectors require at least one track. Therefore, a cut on the trigger called `bhabha` is introduced. This trigger requires a signal coming from the ECL and some additional conditions. Both reconstructed particles have to have an energy of at least 2.5 GeV each and one of

them has to have an energy of 4 GeV or more. Additionally, two conditions have to be fulfilled.

- $160° < \sum \theta_{cms} < 200°$

- $140° < \Delta\phi_{cms} < 220°$

The `bhabha` trigger returns a 1, only if all three conditions are fulfilled. [33]
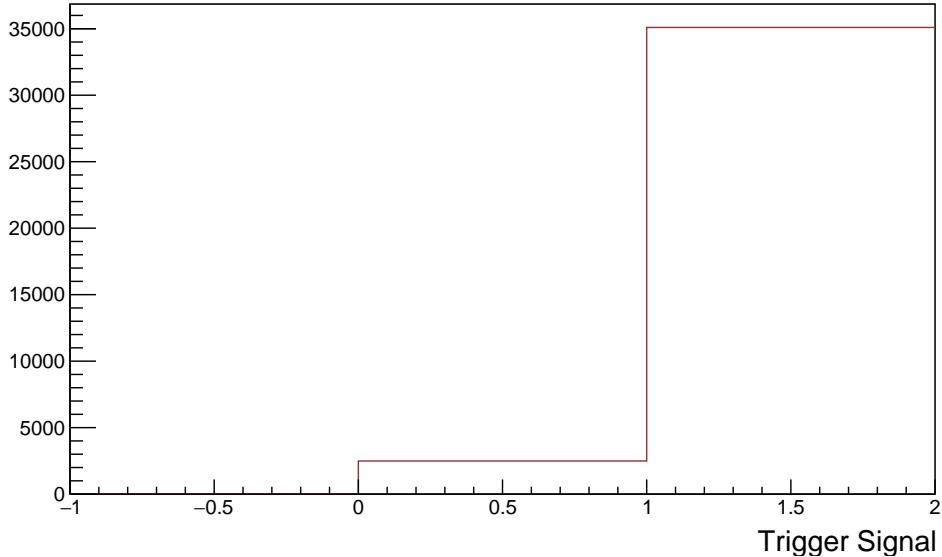
Figure 6.13.: `bhabha` trigger signal for a single phase2 data file after the selection. Trigger Signal = 0 means that there was no trigger signal in the event. Trigger Signal = 1 means that there was a trigger signal in the event. (Trigger Signal = -1 means that there are no trigger informations in the file.) In over 90 % of the selected events there is a trigger signal coming from the ECL.

As shown in figure 6.13, the `bhabha` trigger signal for a single phase2 data file after the selection. Most of the time, there was an ECL trigger signal and in only about 8 % of the events there was no trigger signal coming from the ECL. These events have to be cut away.

This is not done for phase2 Monte Carlo, since the trigger simulation does not work reliably and we only look at events we want to consider because only Bhabha events are generated. Therefore, a trigger cut is only used for phase2 data (and phase3 data in later on). This is also the reason why the cuts on the cluster energy were chosen as they are. Otherwise, a comparison of phase2 MC and phase2 data would be impossible.

6.8. More Events

The efficiency errors are calculated with the following equation:

$$\Delta\epsilon = \sqrt{\frac{\epsilon(1-\epsilon)}{n}} \tag{6.6}$$

In equation 6.6, ϵ is the calculated efficiency and n is the total number of reconstructed *probe* particles with and without an associated track in the investigated bin. This equation is only true for large n, and since, according to this equation, a calculated efficiency of 1 has always an error of zero it is easy to see that a more precise calculation is required. Therefore, the efficiency will be calculated by the root class TEfficiency. This class is able to calculate the right efficiency error even for small n. [34]
To reduce the error on the calculated efficiency, n has to be as big as possible. Therefore, we will consider all available phase2 data and phase2 MC files.
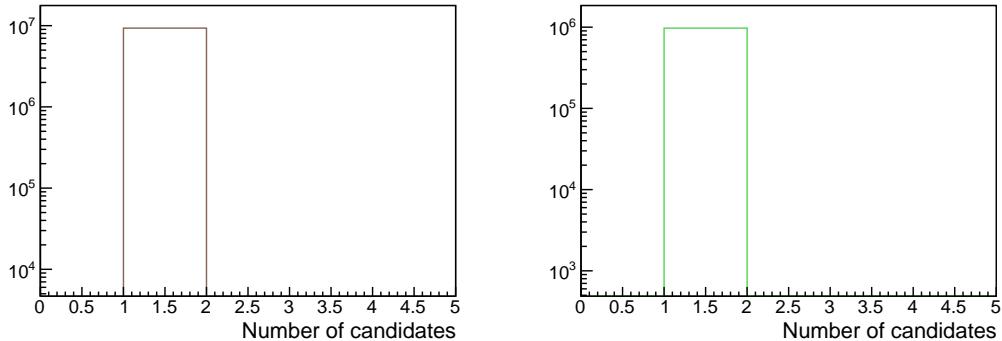
Figure 6.14.: The number of candidates per event after the selection is shown. Left: Phase2 Data. Right: Phase2 MC. A total of 9323903 candidates are selected for phase2 data and 973181 candidates are selected for phase2 MC. Originally, 10^7 $e^+e^- \rightarrow e^+e^-$ events were generated on Monte Carlo.

Figure 6.14 shows the number of candidates per event after the selection using all files. As illustrated in this figure, we reconstruct only one candidate per event on both phase2 data (left) and phase2 MC (right).

6.9. Dividing The ECL In Areas Of Interest

As described in section 3.7, the ECL is divided in three areas, the barrel, the forward end-cap and the backward end-cap. Therefore, we will take a look at the efficiency of these areas separately. The first area will only contain the forward end-cap. This means that only particles with a predicted polar angle of $0° < \theta_{\mathrm{pred,b2b}} < 32°$ will be taken into account. The second area of interest is the barrel. Here the predicted polar angle $\theta_{\mathrm{pred,b2b}}$ of the investigated particle has to be $32° < \theta_{\mathrm{pred,b2b}} < 130°$.

The last area of interest is the backward end-cap with a predicted polar angle of $130° < \theta_{\mathrm{pred,b2b}} < 180°$.

In section 5, we saw that the the polar angle and the momentum of the particles are correlated in the lab frame. Therefore, we need to look at momentum intervals.
Figure 6.15 shows the *denominator* histograms for the electron. In these plots, the predicted polar angle $\theta_{\mathrm{pred,b2b}}$ and predicted azimuthal angle $\phi_{\mathrm{pred,b2b}}$ for different momenta for phase2 MC electrons are shown. Additionally, the three areas of interest are indicated in these plots by a pink line.
Figure A.6 shows the same plots but for phase2 data. Small differences for momenta between $4\,\mathrm{GeV}$ and more at an angle $\phi_{\mathrm{pred,b2b}}$ of about $0°$ are probably caused by the geometry of the vertex detector. As already mentioned in section 6.1, only a small azimuthal fraction was installed at $\phi \approx 0$. The corresponding phase2 data plots for positrons are shown in figure A.9.

In these four figures, one can also see that it makes sense to look only at some momenta for different areas of interest. The different momenta regions are listed in table 6.4. Phase2 MC was used to determine the momenta ranges because the statistics are lower on phase2 MC compared to phase2 data.

Table 6.4.: Momenta ranges for different *probe* cases and different areas of interest as function of $\phi_{\mathrm{pred,b2b}}$.

	e^-	e^+
Forward End-Cap	$4\,\mathrm{GeV} - 8\,\mathrm{GeV}$	/
Barrel	$4\,\mathrm{GeV} - 7\,\mathrm{GeV}$	$3\,\mathrm{GeV} - 7\,\mathrm{GeV}$
Backward End-Cap	/	$2\,\mathrm{GeV} - 6\,\mathrm{GeV}$

The same is done for the transverse momenta for the three different cases. The denominator plots of phase2 MC for the electrons can be seen in figure 6.17. Figure 6.18 shows the denominator plots for phase2 MC positrons. The different transverse momenta regions are listed in table 6.5.

Table 6.5.: Transverse Momenta ranges for different *probe* cases and different areas of interest as function of $\phi_{\mathrm{pred,b2b}}$.

	e^-	e^+
Forward End-Cap	$1\,\mathrm{GeV} - 4\,\mathrm{GeV}$	/
Barrel	$2\,\mathrm{GeV} - 6\,\mathrm{GeV}$	$3\,\mathrm{GeV} - 6\,\mathrm{GeV}$
Backward End-Cap	/	$1\,\mathrm{GeV} - 4\,\mathrm{GeV}$

We will also look at the tracking efficiency as function of $\theta_{\mathrm{pred,b2b}}$. For this, we also have to choose momenta regions. They can be determined by the same plots as before. The selected ranges can be found in table 6.6.

Table 6.6.: Momenta and transverse momenta ranges for the tracking efficiency as function of $\theta_{\mathrm{pred,b2b}}$ for different *probe* cases.

	e^-	e^+
Momentum	$4\,\mathrm{GeV} - 9\,\mathrm{GeV}$	$2\,\mathrm{GeV} - 7\,\mathrm{GeV}$
Transverse Momentum	$1\,\mathrm{GeV} - 6\,\mathrm{GeV}$	$1\,\mathrm{GeV} - 6\,\mathrm{GeV}$

Figure 6.15.: Predicted $\theta_{\mathrm{pred,b2b}}$ and $\phi_{\mathrm{pred,b2b}}$ denominator histograms of the electron for different momenta for phase2 MC are shown. The different areas of interest are indicated by the pink line.

Figure 6.16.: Predicted $\theta_{\mathrm{pred,b2b}}$ and $\phi_{\mathrm{pred,b2b}}$ denominator histograms of the positron for different momenta phase2 MC are shown. The different areas of interest are indicated by the pink line.

Figure 6.17.: Predicted $\theta_{\mathrm{pred,b2b}}$ and $\phi_{\mathrm{pred,b2b}}$ denominator histograms of the electron for different transverse momenta for phase2 MC are shown. The different areas of interest are indicated by the pink line.

Figure 6.18.: Predicted $\theta_{\mathrm{pred,b2b}}$ and $\phi_{\mathrm{pred,b2b}}$ denominator histograms of the positron for different transverse momenta for phase2 MC are shown. The different areas of interest are indicated by the pink line.

CHAPTER 7
Phase2 Tracking Efficiency

I~N~ this chapter the tracking efficiency studies on phase2 will be presented. The selection described in chapter 6 will be applied. Phase2 data will be shown in brown together with phase2 Monte Carlo in green, in order to make the comparison of these two easier. Additionally, only tracking efficiencies with an error of $\Delta\epsilon < 0.4$ are plotted to make the plots more easy to read.

We will see that the tracking efficiencies for phase2 MC will be higher than the tracking efficiencies for phase2 data. This is expected because on Monte Carlo the detector is simulated as a whole and it is impossible to consider every single aspect of the structure of the detector like cabling, screws and even impurities of the material which we have in reality. These additional materials can interact with the outgoing particles, and these particles could scatter an additional time or could be absorbed by the material producing bremsstrahlung, for example. In addition, there is no dead time of the detector in MC. Each event is simulated individually. This is another error source for real data. Additionally, on MC the detector is working under optimal conditions. Only one event is happening at a time, there are no fluctuations in the power supplies etc. For real data, all of these issues result in a lower tracking efficiency. Therefore, phase2 MC should have a higher tracking efficiency compared to phase2 data. Otherwise, it will be noted. In addition, the noise, produced by the electronics and beam, may not be simulated realistically and a misalignment of detector parts in the simulation may affect the reconstruction algorithm. This is also true for phase3.

7.1. Tracking Efficiencies As Function Of $\theta_{\mathrm{pred,b2b}}$-$\phi_{\mathrm{pred,b2b}}$

Figure 7.1 shows the tracking efficiency as function of $\theta_{\mathrm{pred,b2b}}$-$\phi_{\mathrm{pred,b2b}}$ for phase2 MC on the left and phase2 data on the right. The efficiencies for electrons are shown in the first row and positrons in the second row. These plots combine all momenta of the particles. For electrons there is a difference between phase2 MC and phase2 data in the forward end-cap. For phase2 MC there is almost no drop of the efficiency in the forward end-cap in contrast to phase2 data.

For positrons the differences occur in the backward end-cap. The transition between high and low tracking efficiency is way more sharp on phase2 MC compared to phase2 data. Additionally, at around $\phi_{\mathrm{pred,b2b}} \approx 0$ and $\theta_{\mathrm{pred,b2b}} \approx 2.4$ there is something like a *horn* structure in phase2 data. We will discuss this structure in section 7.2.3 for positrons with momenta between $3\,\mathrm{GeV}$ and $5\,\mathrm{GeV}$.
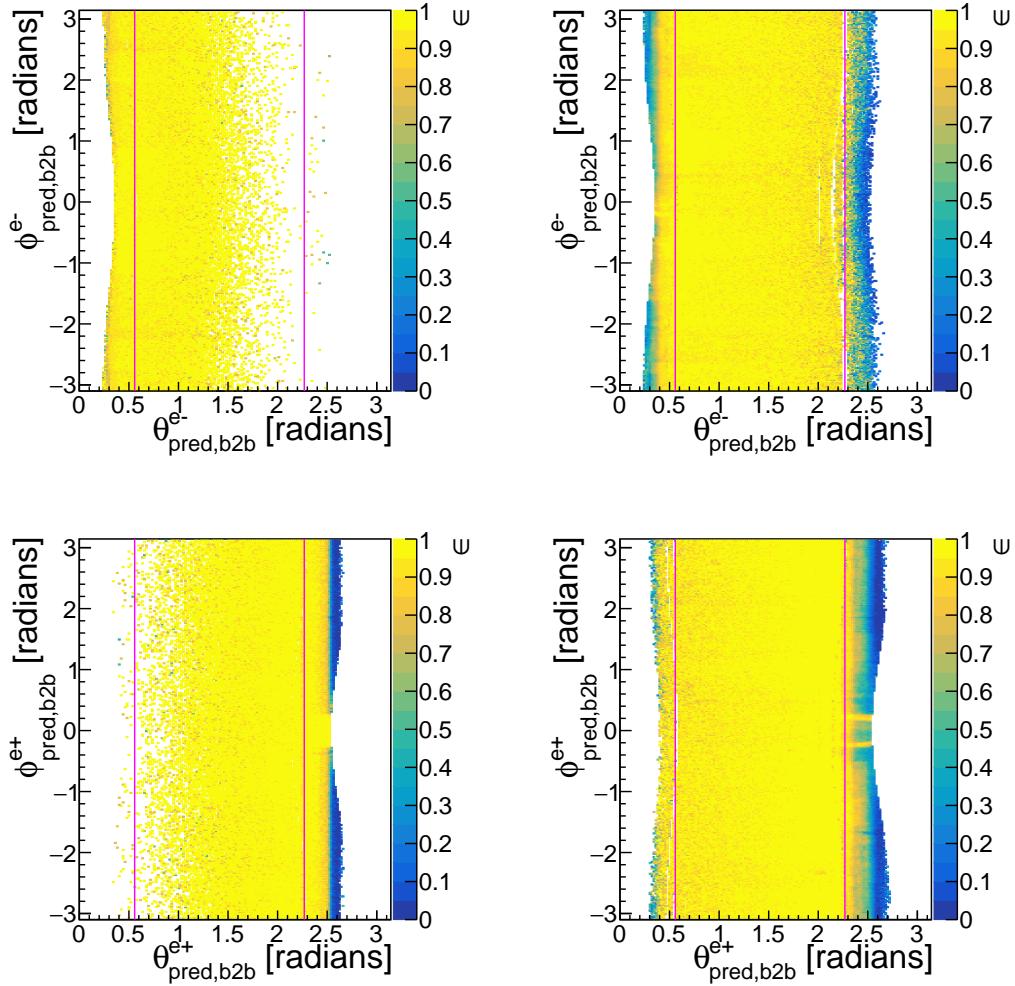
Figure 7.1.: Tracking efficiency as function of $\theta_{\mathrm{pred},b2b}$-$\phi_{\mathrm{pred},b2b}$ for phase2. Left: Phase2 MC. Right: Phase2 data. First row: electron efficiencies. Second row: positron efficiencies. The 2D plots with the corresponding error can be found in the appendix figure A.19. The pink line indicates the different sectors of the ECL.

7.2. ϵ In Bins Of Track Momentum

7.2.1. Forward End-Cap

Figure 7.2 shows the calculated electron tracking efficiency for different momenta. As expected, the tracking efficiency for phase2 data is almost all of the time worse than the efficiency for phase2 MC for all momenta in the forward end-cap. For momenta between 4 GeV and 5 GeV phase2 MC and phase2 data have a similar tracking efficiency. In both cases, the lowest efficiency occurs at $\phi_{\mathrm{pred,b2b}} \approx 0$. According to figures 6.15 and A.6, we expect that most electrons have a momentum between 5 GeV and 8 GeV. For momenta between 5 GeV and 6 GeV phase2 data and phase2 MC have some differences in the calculated tracking efficiency. Phase2 MC has an efficiency between ~ 0.80 and ~ 0.95 with an exception of an efficiency drop at $\phi_{\mathrm{pred,b2b}} \approx 0$. This drop also appears on phase2 data, but for $|\phi_{\mathrm{pred,b2b}}| \gtrsim 1.5$ the efficiency on phase2 data is much worse compared to the tracking efficiency of phase2 MC. Here the efficiency drops partially below 0.7 for phase2 data. The biggest difference occurs for momenta between 6 GeV and 7 GeV. For phase2 MC the tracking efficiency ranges between ~ 0.90 and almost 1. But the efficiency oscillates heavily between ~ 0.6 and 0.95 for phase2 data. In both cases the highest efficiency occurs at $\phi_{\mathrm{pred,b2b}} \approx 0$. For momenta between 7 GeV and 8 GeV phase2 MC has a tracking efficiency of above 0.98 for all angles of $\phi_{\mathrm{pred,b2b}}$ except for $\phi_{\mathrm{pred,b2b}} \approx 0$. Here the efficiency is still high but the errors are larger. For phase2 data, the efficiency is also very high for $|\phi_{\mathrm{pred,b2b}}| \gtrsim 1$. But for $|\phi_{\mathrm{pred,b2b}}| \lesssim 1$ the efficiency falls down by over 10 %.
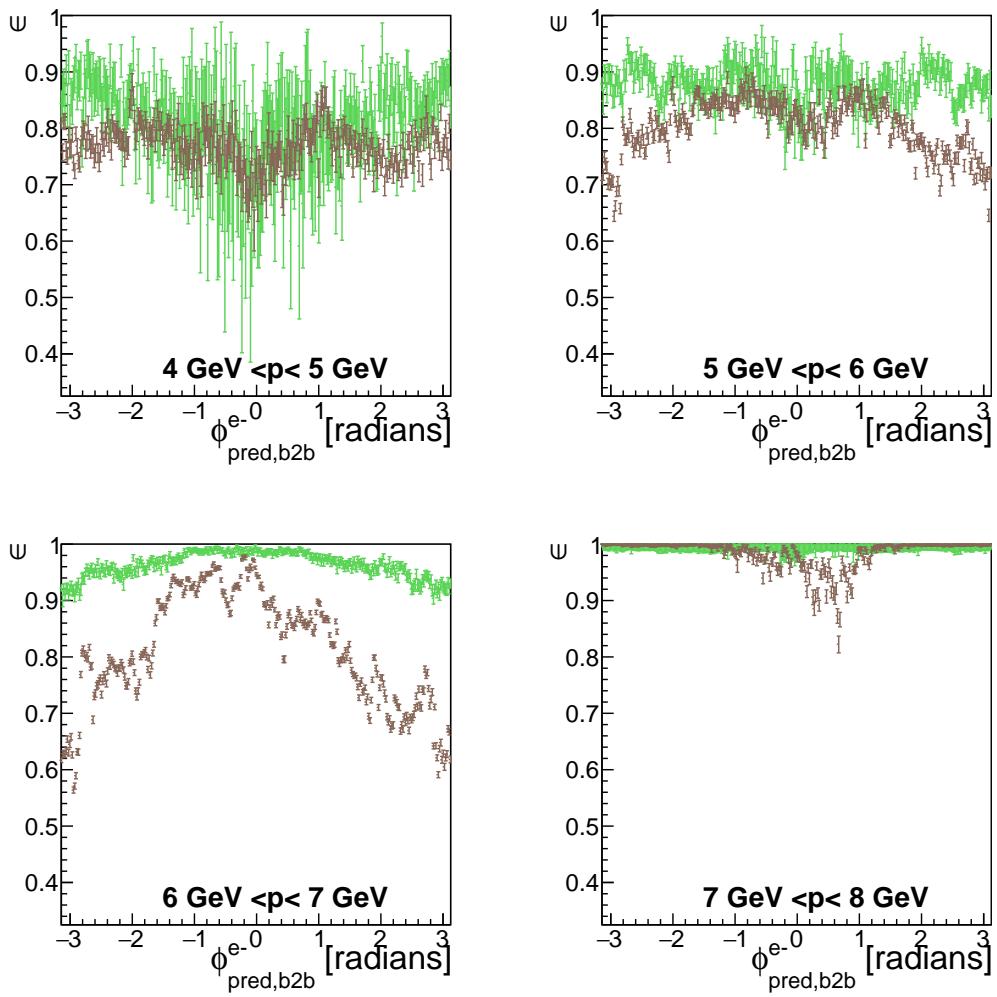
Figure 7.2.: Electron tracking efficiency plots as function of $\phi_{\mathrm{pred,b2b}}$ for different momenta in the forward end-cap. The tracking efficiency for phase2 data is shown in brown and phase2 MC in green.

7.2.2. Barrel

In figure 7.3 the calculated electron tracking efficiency in the barrel is shown. For momenta between $4\,\text{GeV}$ and $5\,\text{GeV}$ the tracking efficiency ranges between 0.75 and 0.98 for phase2 MC and between ~ 0.75 and 0.93 for phase2 data. For phase2 data the efficiency has its minimum at $\phi_{\text{pred,b2b}} \approx 0$. For momenta between $5\,\text{GeV}$ and $6\,\text{GeV}$ the efficiency gets better. The tracking efficiency ranges between 0.90 and 0.99 for phase2 MC and between 0.91 and 0.98 for phase2 data. The structure of this efficiency is very similar compared to the tracking efficiency for momenta between $4\,\text{GeV}$ and $5\,\text{GeV}$. In both cases the lowest efficiency occurs at $\phi_{\text{pred,b2b}} \approx 0$ for phase2 data. The best tracking efficiencies for electrons in the barrel appear at momenta between $6\,\text{GeV}$ and $7\,\text{GeV}$. Here the efficiency for phase2 MC ranges between 0.98 and 1 and for phase2 data between ~ 0.955 and ~ 0.995. Again, the lowest calculated tracking efficiency occurs at $\phi_{\text{pred,b2b}} \approx 0.5$. Without this drop, the tracking efficiency of phase2 data is between ~ 0.98 and 1.

The calculated tracking efficiencies for positrons in the barrel can be found in figure 7.4. For momenta between $3\,\text{GeV}$ and $4\,\text{GeV}$ the calculated tracking efficiency is between ~ 0.7 and ~ 0.98 for phase2 MC and between ~ 0.7 and 0.92 for phase2 data. The efficiency for phase2 MC stays more or less the same over all values of $\phi_{\text{pred,b2b}}$. For phase2 data, there is an efficiency drop at $\phi_{\text{pred,b2b}} \approx 0$. For momenta between $4\,\text{GeV}$ and $5\,\text{GeV}$ the tracking efficiency ranges between 0.97 and 1 for phase2 MC and between 0.96 and 0.99 for phase2 data. Phase2 data has almost always a lower calculated tracking efficiency than phase2 MC. The biggest difference between phase2 data and phase2 MC appears at $\phi_{\text{pred,b2b}} \approx 0.5$. Here the efficiency for phase2 data falls down significantly. For momenta between $5\,\text{GeV}$ and $6\,\text{GeV}$ the tracking efficiency ranges between 0.93 and 1 for phase2 MC and 0.95 and 0.99 for phase2 data. The tracking efficiency for phase2 MC is higher by ~ 0.02 compared to phase2 data for almost all angles of $\phi_{\text{pred,b2b}}$. For momenta between $6\,\text{GeV}$ and $7\,\text{GeV}$ the phase2 MC tracking efficiency ranges between ~ 0.75 and 1. This wide range is a result of the low statistic for positrons at this momentum. The calculated tracking efficiency for phase2 data ranges between ~ 0.9 and 1. For all tracking efficiencies with momenta between $4\,\text{GeV}$ and $7\,\text{GeV}$ a dip at $\phi_{\text{pred,b2b}} \approx 0.5$ can be seen.
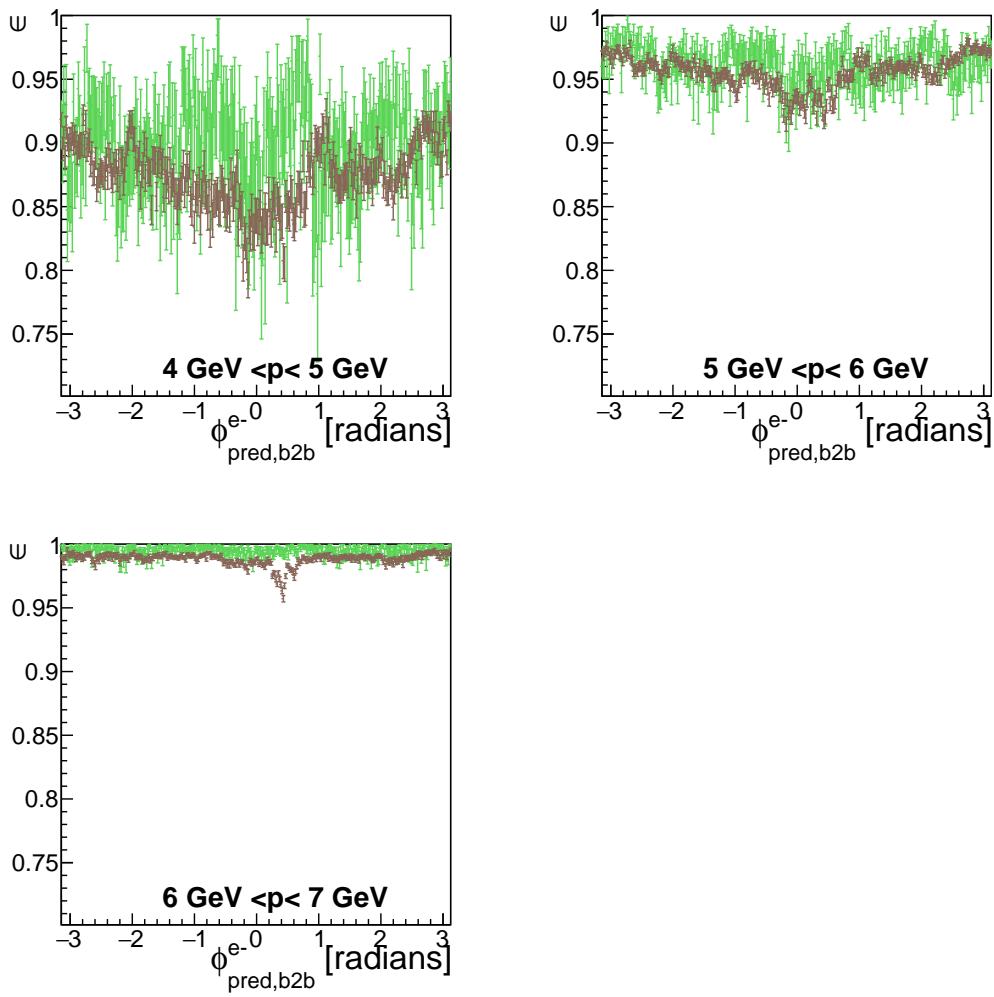
Figure 7.3.: Electron tracking efficiency plots as function of $\phi_{\mathrm{pred,b2b}}$ for different momenta in the barrel. The tracking efficiency for phase2 data is shown in brown and phase2 MC in green.
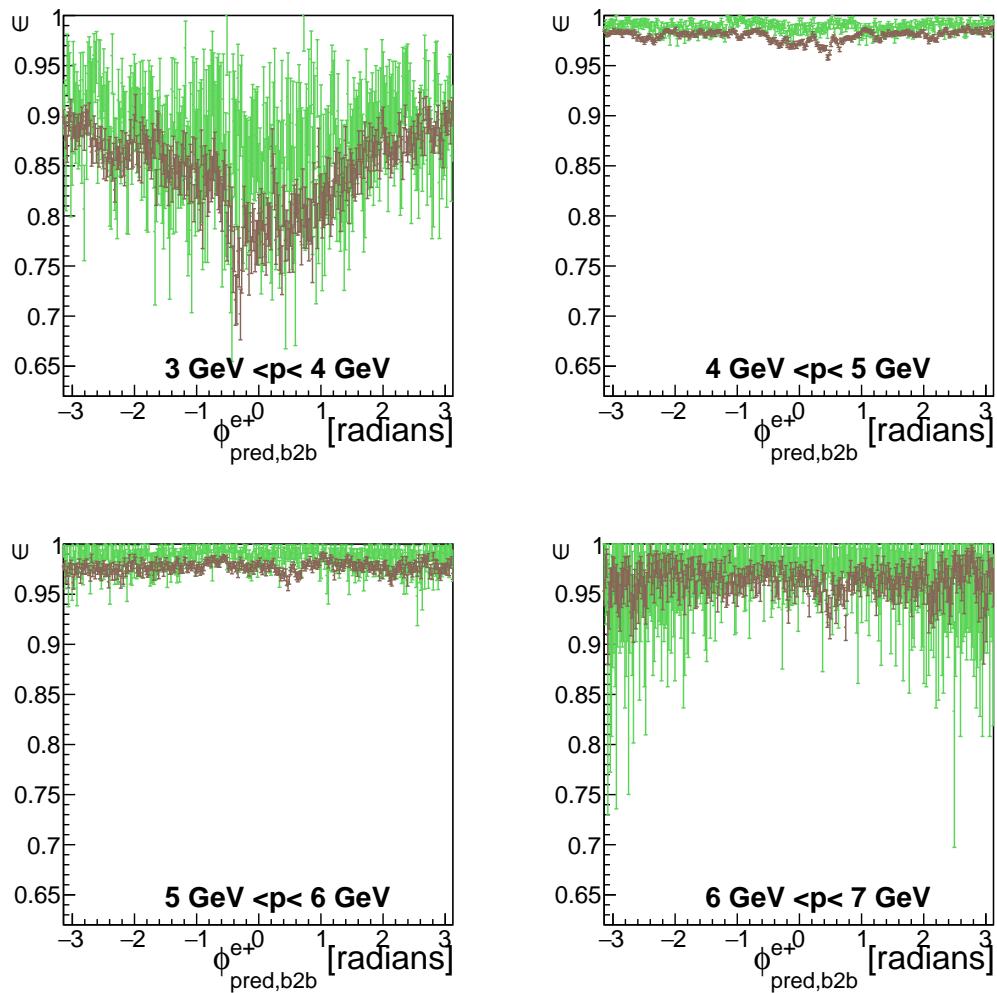
Figure 7.4.: Positron tracking efficiency plots as function of $\phi_{\mathrm{pred,b2b}}$ for different momenta in the barrel. The tracking efficiency for phase2 data is shown in brown and phase2 MC in green.

7.2.3. Backward End-Cap

Figure 7.5 shows the calculated positron tracking efficiency for different momenta in the backward end-cap as function of $\phi_{\mathrm{pred,b2b}}$. Due to the kinematics at Belle II, almost no electrons are detected in the backward end-cap. For momenta between $2\,\mathrm{GeV}$ and $3\,\mathrm{GeV}$ the calculated tracking efficiency is between 0.95 and 1 for phase2 data and between ~ 0.85 and 1 for phase2 MC. An exception occurs at $\phi_{\mathrm{pred,b2b}} \approx 0$, here the error bars for phase2 MC are noticeably large. For momenta between $3\,\mathrm{GeV}$ and $4\,\mathrm{GeV}$ the tracking efficiency covers a very large range. For phase2 MC the efficiency is between ~ 0.4 and ~ 0.95 and for phase2 data between ~ 0.2 and ~ 0.85. For $\phi_{\mathrm{pred,b2b}} \lesssim -1$, the efficiency is slightly higher for phase2 data compared to phase2 MC. A strange structure occurs at $\phi_{\mathrm{pred,b2b}} \approx 0$ for phase2 data. Starting at $\phi_{\mathrm{pred,b2b}} \approx -1.7$ the efficiency goes up from ~ 0.4 to ~ 0.65 at $\phi_{\mathrm{pred,b2b}} \approx -0.8$, then it goes back down to ~ 0.4 before it reaches a maximum of ~ 0.8 at $\phi_{\mathrm{pred,b2b}} \lesssim 0$. At $\phi_{\mathrm{pred,b2b}} = 0$ the efficiency is down to ~ 0.6. At $\phi_{\mathrm{pred,b2b}} \gtrsim 0$, the efficiency is back to a maximum of ~ 0.85 before it drops to ~ 0.4. After that the efficiency stays constant until it starts to drop down again at $\phi_{\mathrm{pred,b2b}} \approx 1.5$. It reaches its minimum at $\phi_{\mathrm{pred,b2b}} \approx 2$. For phase2 MC the calculated tracking efficiency starts similar to phase2 data at around 0.5 and it slowly increases up to $\phi_{\mathrm{pred,b2b}} \approx -1$. Then it starts to vary from phase2 data. For phase2 MC the efficiency increases rapidly until it reaches its maximum at $\phi_{\mathrm{pred,b2b}} = 0$. Then it drops back to ~ 0.6 at $\phi_{\mathrm{pred,b2b}} \approx 1$. A similar structure can be found for momenta between $4\,\mathrm{GeV}$ and $5\,\mathrm{GeV}$. The only difference is that the efficiency is higher compared to the lower momenta ranges. For example, phase2 MC reaches a calculated tracking efficiency of almost 1 at $\phi_{\mathrm{pred,b2b}} = 0$. For momenta between $5\,\mathrm{GeV}$ and $6\,\mathrm{GeV}$ the efficiency is above 0.9 for phase2 MC and above 0.98 for phase2 data with the exception of $\phi_{\mathrm{pred,b2b}} \approx 0$. Here the error of the calculated efficiencies are very large in both cases due to the low statistics.
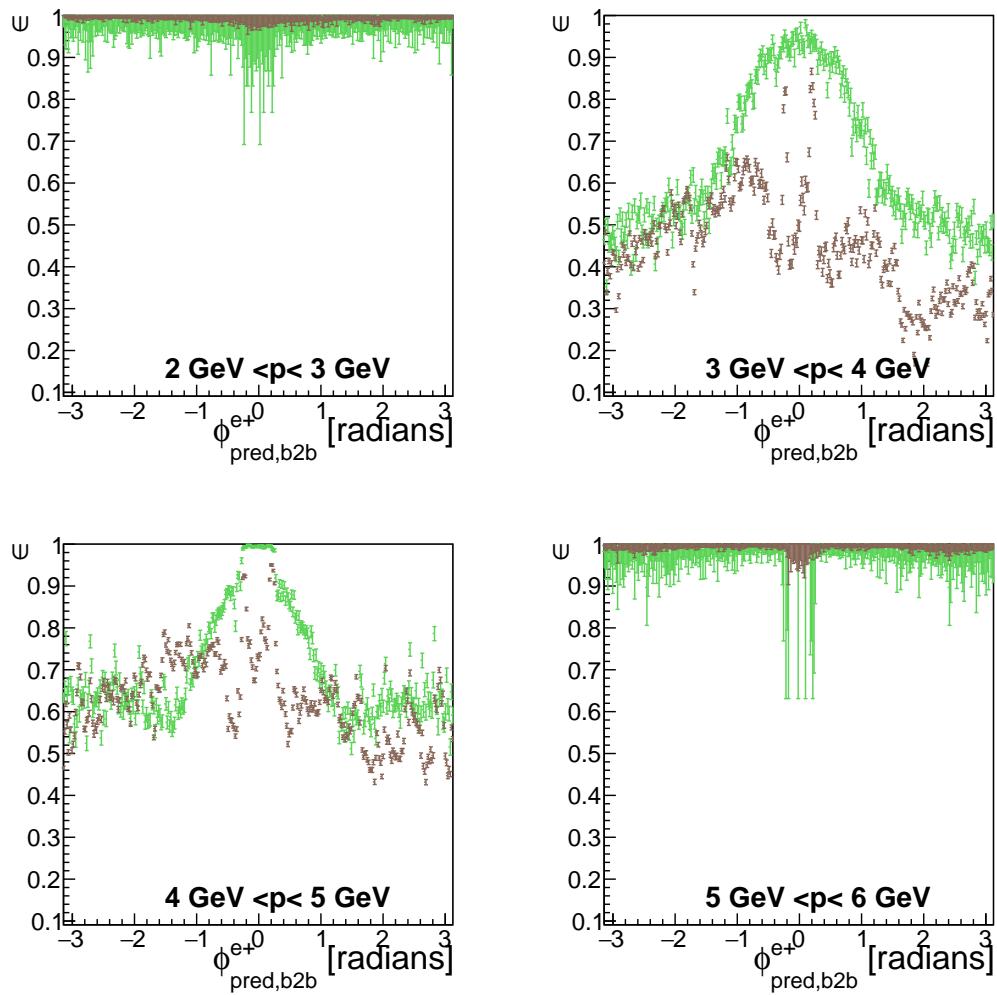
Figure 7.5.: Positron tracking efficiency plots as function of $\phi_{\mathrm{pred,b2b}}$ for different momenta in the backward end-cap. The tracking efficiency for phase2 data is shown in brown and phase2 MC in green.

7.2.4. Tracking Efficiencies As Function Of $\theta_{\mathrm{pred,b2b}}$

This section will present the calculated tracking efficiencies as function of $\theta_{\mathrm{pred,b2b}}$. The pink lines in each of the following plots will indicate the different areas of the ECL.

Figure 7.6 shows the calculated electron tracking efficiency for different momenta as function of the polar angle. For momenta between 3 GeV and 4 GeV the calculated tracking efficiency starts high for small angles of $\theta_{\mathrm{pred,b2b}}$. For phase2 MC and phase2 data the highest efficiency is in the forward end-cap with over 0.9. But it drops very quickly with increasing $\theta_{\mathrm{pred,b2b}}$. At the transition between the forward end-cap and the barrel the efficiency has a local minimum of only about 0.2 for phase2 data and almost 0 for phase2 MC. For $0.5 \lesssim \theta_{\mathrm{pred,b2b}} \lesssim 0.7$ the efficiency goes back up to ~ 0.6 very quickly. After this, the efficiency increases slowly to around 0.85 for phase2 data and 0.9 for phase2 MC at $\theta_{\mathrm{pred,b2b}} \approx 2.2$. At this angle the barrel ends and the backward end-cap begins. In the backward end-cap the efficiency goes up to over 0.9 at first for phase2 MC before it falls down to 0 rather quickly. In contrast, the phase2 data tracking efficiency drops down strictly monotonic in the backward end-cap. For momenta between 4 GeV and 5 GeV the structure of the efficiency is similar to the momentum region we just looked at. The only differences are that the efficiency drops at the forward end-cap to barrel transition is not as dominant as before. Here the efficiency only drops to ~ 0.6. Additionally, phase2 MC has a higher tracking efficiency in the forward end-cap compared to phase2 data. In addition, the highest efficiency is reached in the barrel at $1.7 \lesssim \theta_{\mathrm{pred,b2b}} \lesssim 2.3$ for phase2 MC and $1.7 \lesssim \theta_{\mathrm{pred,b2b}} \lesssim 2.2$ for phase2 data. The biggest difference between phase2 MC and phase2 data occurs again in the backward end-cap. Here the phase2 data tracking efficiency drops down noticeably earlier compared to phase2 MC. The phase2 data tracking efficiency is lower compared to phase2 MC for almost all values of $\theta_{\mathrm{pred,b2b}}$. For momenta between 5 GeV and 6 GeV there is no dip in the efficiency at the transition between forward end-cap and barrel. In the forward end-cap the efficiency of phase2 data starts lower compared to the phase2 MC efficiency. But they meet at $\theta_{\mathrm{pred,b2b}} \approx 0.4$ and increase up to approximately 0.95 and more at $\theta_{\mathrm{pred,b2b}} \approx 1$. For higher $\theta_{\mathrm{pred,b2b}}$ values the efficiency in the barrel stays more or less the same. One can argue that there is a small dip in phase2 data at $\theta_{\mathrm{pred,b2b}} \approx 1.9$. In the plot for the momentum range between 6 GeV and 7 GeV the efficiency for phase2 data starts lower compared to phase2 MC efficiency. In the barrel both efficiencies stay above 0.98 with an exception of a small dip for phase2 data at $\theta_{\mathrm{pred,b2b}} \approx 1.25$. For momenta between 7 GeV and 8 GeV the tracking efficiency for phase2 MC is about 0.99. This was already discussed in section 7.2.1. For phase2 the tracking efficiency is slightly lower. Again for phase2 data, a small dip in the tracking efficiency at $\theta_{\mathrm{pred,b2b}} \approx 0.4$ appears. For the last momentum range, similar to the previous momenta range, the tracking efficiencies for phase2 MC and phase2 MC are above 0.95.

In figure 7.7 the calculated tracking efficiency for positrons as function of $\theta_{\mathrm{pred,b2b}}$ is shown. For momenta between 2 GeV and 3 GeV almost all positrons are detected in the backward end-cap, with a tracking efficiency of over 0.98 for phase2 MC and

phase2 data. For momenta between $3\,\mathrm{GeV}$ and $4\,\mathrm{GeV}$ the tracking efficiency increases slowly in the barrel with increasing values of $\theta_{\mathrm{pred,b2b}}$. It reaches its maximum of ~ 0.9 at $\theta_{\mathrm{pred,b2b}} \approx 2.2$. Then the tracking efficiency drops for phase2 data and it continues to drop in the backward end-cap. For phase2 MC the efficiency has a small peak in the backward end-cap before it also falls down. For momenta between $4\,\mathrm{GeV}$ and $5\,\mathrm{GeV}$ the tracking efficiency has a similar structure compared to the previous momenta range except it is overall higher. The calculated tracking efficiency also slowly increases in the barrel until it reaches its maximum of over 0.95 for phase2 MC and phase2 data at $\theta_{\mathrm{pred,b2b}} \approx 1.6$. The tracking efficiency stays more or less constant with increasing $\theta_{\mathrm{pred,b2b}}$ in the barrel. As soon as the backward end-cap starts the phase2 data efficiency drops down. Phase2 MC tracking efficiency stays very high up to $\theta_{\mathrm{pred,b2b}} \approx 2.4$. For momenta between $5\,\mathrm{GeV}$ and $6\,\mathrm{GeV}$ the calculated tracking efficiency also gets higher in the barrel. It reaches its maximum at $\theta_{\mathrm{pred,b2b}} \approx 1$. After this it stays more or less the same, even in the backward end-cap. At $\theta_{\mathrm{pred,b2b}} \approx 1.9$ there is a small dip for phase2 data. We saw this also for electrons at the same momenta range. The last positron momenta range is between $6\,\mathrm{GeV}$ and $7\,\mathrm{GeV}$. Here the calculated tracking efficiency increases rapidly in the forward end-cap. It reaches its maximum of over 0.95 for phase2 MC and around 0.95 for phase2 data in the barrel. In contrast to the forward end-cap and the barrel, the tracking efficiency in the backward end-cap is higher for phase2 data compared to phase2 MC. This is probably due to the larger error bars of phase2 MC. Similar to the phase2 data tracking efficiency for electrons with the same momenta range, there is a small dip at $\theta_{\mathrm{pred,b2b}} \approx 1.25$.
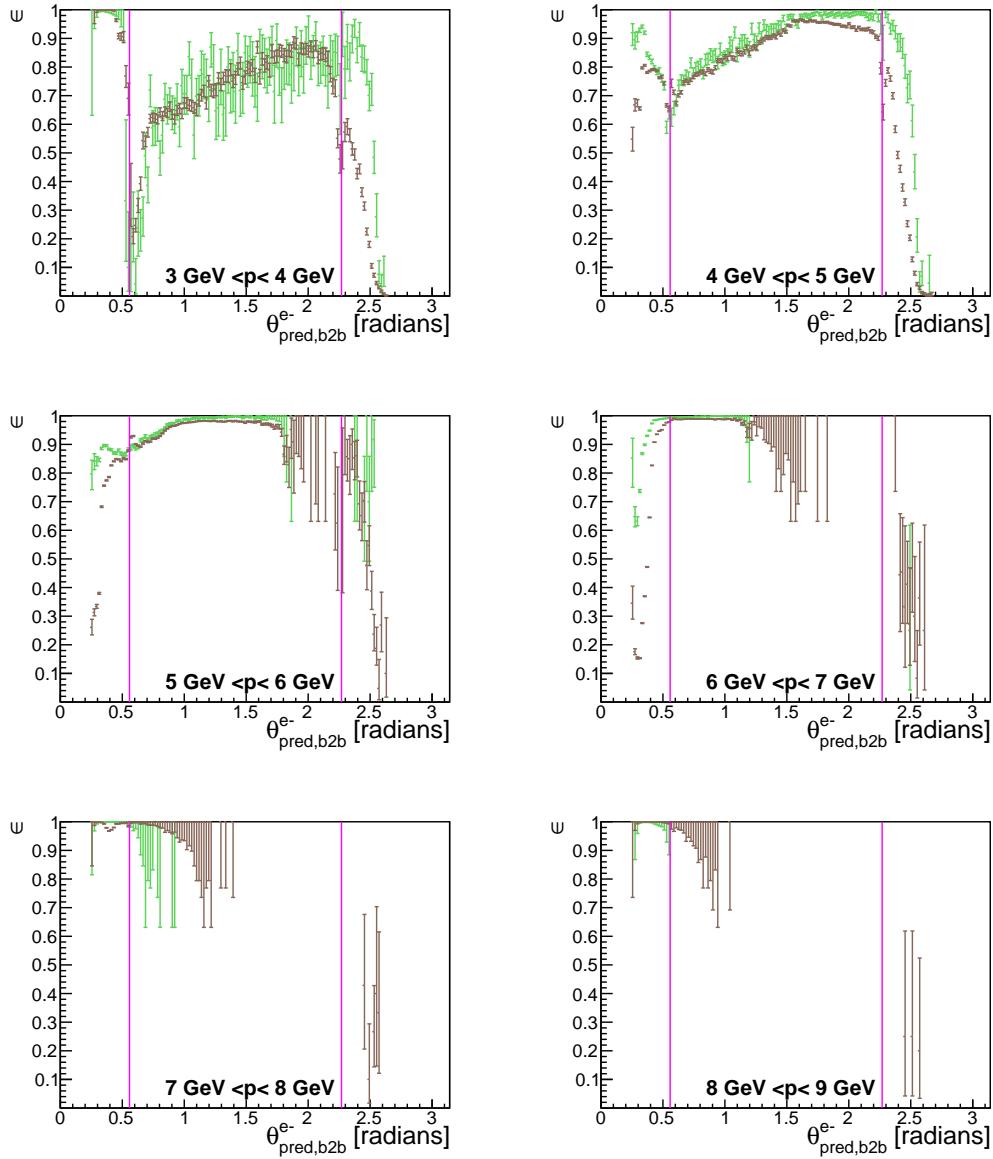
Figure 7.6.: Electron tracking efficiency plots as function of $\theta_{\mathrm{pred,b2b}}$ for different momenta. The tracking efficiency for phase2 data is shown in brown and phase2 MC in green. The pink line indicates the different sectors of the ECL.
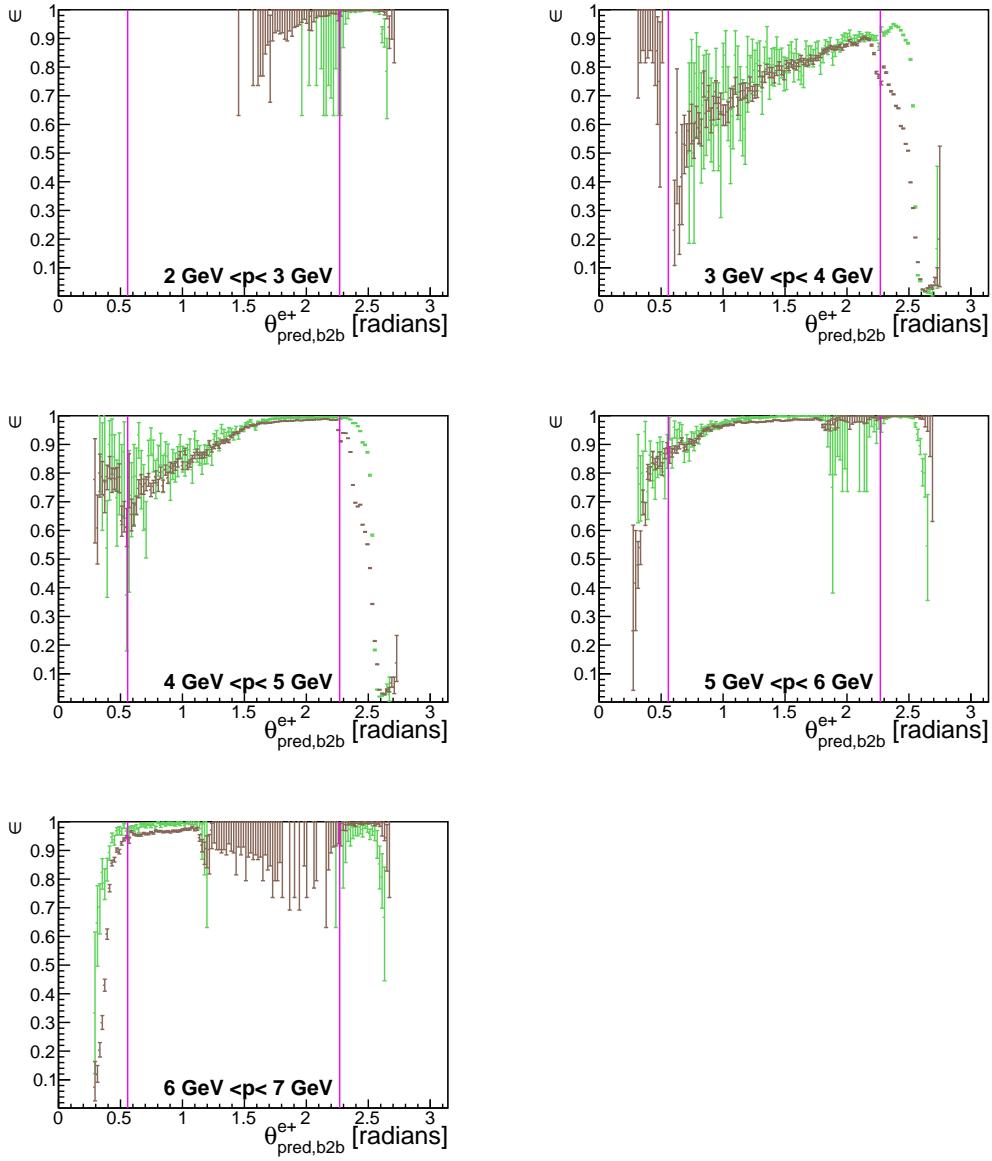
Figure 7.7.: Positron tracking efficiency plots as function of $\theta_{\mathrm{pred,b2b}}$ for different momenta. The tracking efficiency for phase2 data is shown in brown and phase2 MC in green. The pink line indicates the different sectors of the ECL.

7.3. ϵ In Bins Of Track Transverse Momentum

7.3.1. Forward End-Cap

Figure 7.8 shows the calculated tracking efficiency for electrons in the forward end-cap as function of $\phi_{\mathrm{pred,b2b}}$ for different transverse momenta. For transverse momenta between $1\,\mathrm{GeV}$ and $2\,\mathrm{GeV}$ the biggest differences between phase2 MC and phase2 data occur at $|\phi_{\mathrm{pred,b2b}}| \gtrsim 1$. For these angles the phase2 data efficiency is noticeably worse compared to phase2 MC. The phase2 data tracking efficiency is between 0.42 and 0.95 and between ~ 0.4 and 1 for phase2 MC. For transverse momenta between $2\,\mathrm{GeV}$ and $3\,\mathrm{GeV}$ the tracking efficiency for phase2 MC stays above 0.9 for all values of $\phi_{\mathrm{pred,b2b}}$. For phase2 data, the structure of the tracking efficiency looks more random. The lowest efficiency of approximately 0.65 occurs at $|\phi_{\mathrm{pred,b2b}}| \approx 3$ and the highest efficiency with ~ 0.9 at $\phi_{\mathrm{pred,b2b}} \approx 0$. Additionally, the efficiency has a lot of local minima and maxima. For transverse momenta between $3\,\mathrm{GeV}$ and $4\,\mathrm{GeV}$ phase2 MC has an efficiency of over 0.97 for almost all values of $\phi_{\mathrm{pred,b2b}}$. The tracking efficiency for phase2 data also has an efficiency of over ~ 0.97 for most values of $\phi_{\mathrm{pred,b2b}}$ with the exceptions of $|\phi_{\mathrm{pred,b2b}}| \approx 0.5$, $\phi_{\mathrm{pred,b2b}} \approx 1$ and $\phi_{\mathrm{pred,b2b}} \approx 2.9$. In all of these cases the tracking efficiency drops down significantly and in the $\phi_{\mathrm{pred,b2b}} \approx 0.5$ case even down to ~ 0.92.
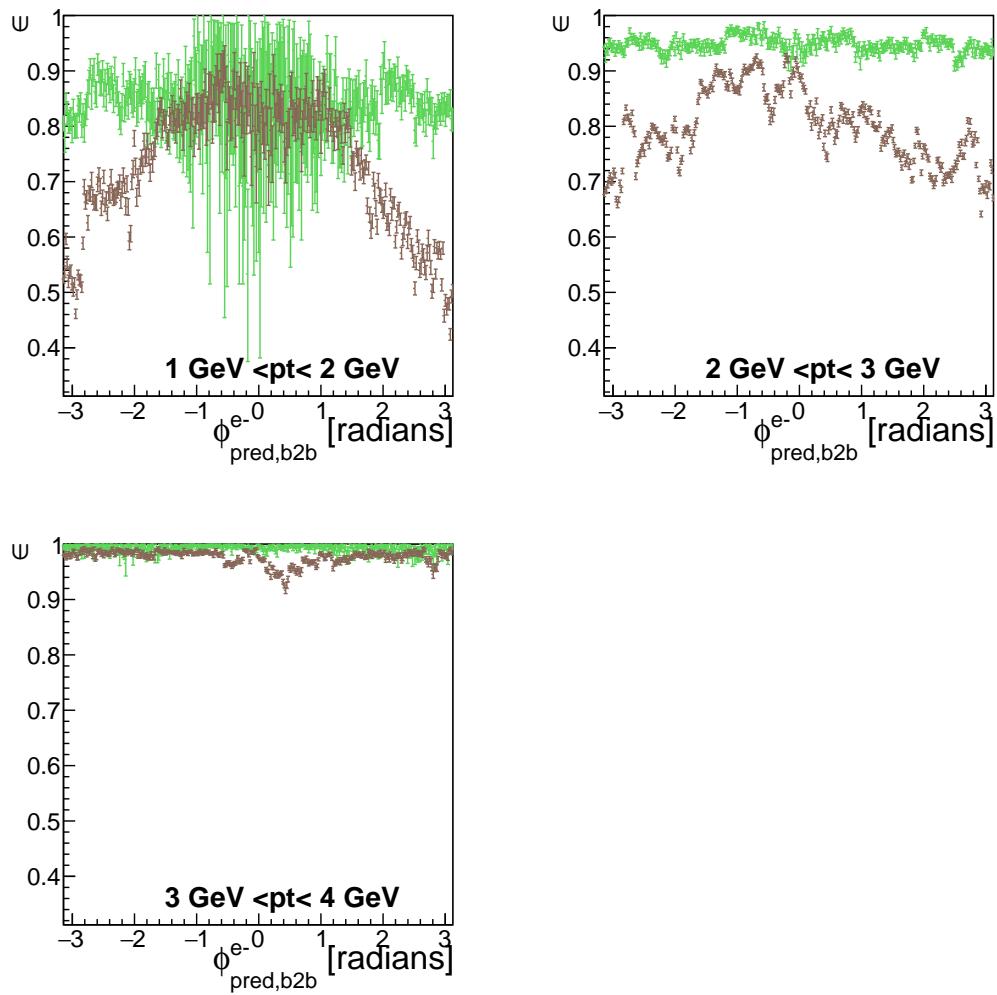
Figure 7.8.: Electron tracking efficiency plots as function of $\phi_{\mathrm{pred,b2b}}$ with different transverse momentum in the forward end-cap. The tracking efficiency for phase2 data is shown in brown and phase2 MC in green.

7.3.2. Barrel

Figure 7.9 shows the calculated phase2 electron tracking efficiency for different transverse momenta as function of $\phi_{\mathrm{pred,b2b}}$ in the barrel. For transverse momenta between $2\,\mathrm{GeV}$ and $3\,\mathrm{GeV}$ the tracking efficiency of phase2 MC and phase2 data has a very similar structure. In both cases the lowest tracking efficiency occurs at $\phi_{\mathrm{pred,b2b}} \approx 0$. For transverse momenta between $3\,\mathrm{GeV}$ and $5\,\mathrm{GeV}$ the structure of the efficiency of phase2 MC and phase2 data differ. For phase2 MC and phase2 data the tracking efficiency is above ~ 0.92. The tracking efficiency becomes higher with increasing transverse momentum. The highest tracking efficiency occurs at transverse momenta between $5\,\mathrm{GeV}$ and $6\,\mathrm{GeV}$. The efficiency of phase2 MC and phase2 data never falls below ~ 0.95. For phase2 data the lowest tracking efficiency appears at $\phi_{\mathrm{pred,b2b}} \approx 0$. The error bars for phase2 MC are smaller for $\phi_{\mathrm{pred,b2b}} \approx 0$.

Figure 7.10 shows the positrons tracking efficiencies in the barrel for different transverse momenta as function of $\phi_{\mathrm{pred,b2b}}$. For transverse momenta between $3\,\mathrm{GeV}$ and $4\,\mathrm{GeV}$ the calculated tracking efficiency is above ~ 0.94 for both phase2 MC and phase2 data. The tracking efficiency for phase2 data is lower compared to phase2 MC for almost all values of $\phi_{\mathrm{pred,b2b}}$. Additionally, there are some noticeable dips in the efficiency at $\phi_{\mathrm{pred,b2b}} \approx -2.2$, $\lesssim 0$, ≈ 0.5 and ≈ 2.2. For transverse momenta between $4\,\mathrm{GeV}$ and $5\,\mathrm{GeV}$ the structure of the phase2 data efficiency looks similar to the structure of the lower transverse momenta with the exception that the tracking efficiency is overall higher with at least ~ 0.96 and the dips on phase2 data are not that dominant. For transverse momenta between $5\,\mathrm{GeV}$ and $6\,\mathrm{GeV}$ the phase2 data tracking efficiency is almost always above ~ 0.96. Again, there is a small dip at $\phi_{\mathrm{pred,b2b}} \approx 0.5$. For phase2 MC the tracking efficiency is almost always above ~ 0.95.
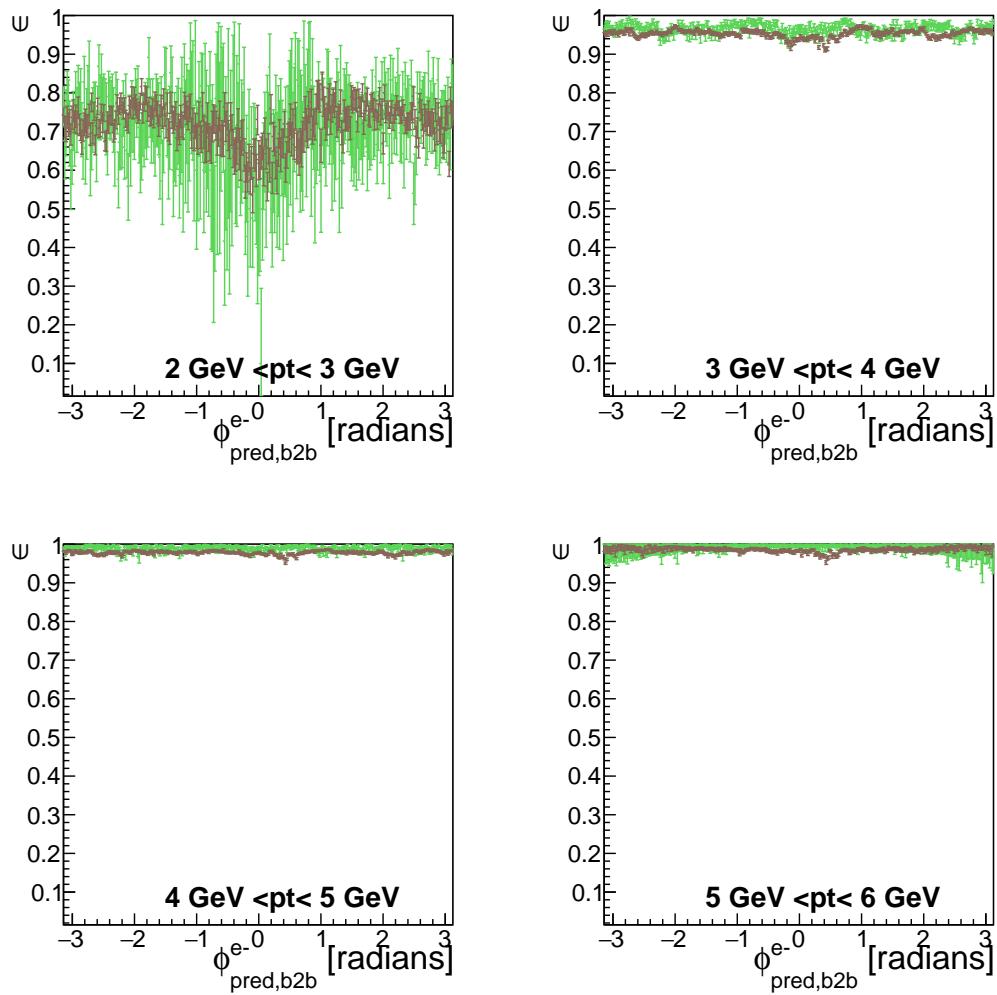
Figure 7.9.: Electron tracking efficiency plots as function of $\phi_{\mathrm{pred,b2b}}$ for different transverse momenta in the barrel. The tracking efficiency for phase2 data is shown in brown and phase2 MC in green.
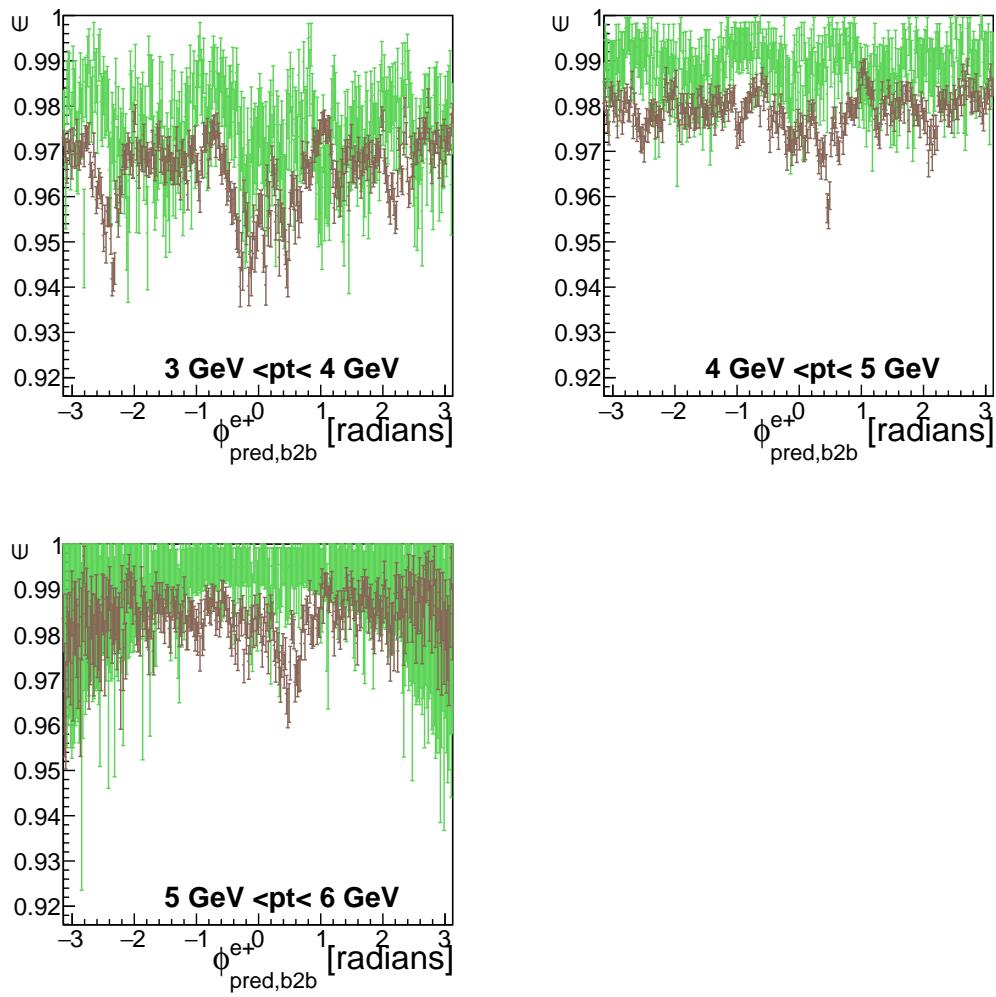
Figure 7.10.: Positron tracking efficiency plots as function of $\phi_{\mathrm{pred,b2b}}$ for different transverse momenta in the barrel. The tracking efficiency for phase2 data is shown in brown and phase2 MC in green.

7.3.3. Backward End-Cap

Figure 7.11 shows the calculated positron tracking efficiencies for different transverse momenta as function of $\phi_{\mathrm{pred,b2b}}$ in the backward end-cap. For transverse momenta between $1\,\mathrm{GeV}$ and $2\,\mathrm{GeV}$ the tracking efficiency of phase2 MC and phase2 data are very close to each other. Some sort of plateau at $|\phi_{\mathrm{pred,b2b}}| \lesssim 1.5$ can be seen. Here the tracking efficiency is very high compared to the efficiency of the remaining angles of $\phi_{\mathrm{pred,b2b}}$. One half of the backward end-cap appears to have a significantly better efficiency. It is also worth noting that for $\phi_{\mathrm{pred,b2b}} \lesssim 1.5$ phase2 data appears to have a higher efficiency compared to phase2 MC and for $\phi_{\mathrm{pred,b2b}} \gtrsim 1.5$ it is the other way around. For transverse momenta between $2\,\mathrm{GeV}$ and $3\,\mathrm{GeV}$ the tracking efficiency for $|\phi_{\mathrm{pred,b2b}}| \gtrsim 1.5$ is again very low with just about 0.6. The plateau we saw before is also way more narrow and it only appears on phase2 MC. For phase2 data the tracking efficiency oscillates heavily at $\phi_{\mathrm{pred,b2b}} \approx 0$. It starts with a drop of the efficiency down to ~ 0.4 at $\phi_{\mathrm{pred,b2b}} \approx -0.5$ followed by a local maximum of ~ 0.9 at $\phi_{\mathrm{pred,b2b}} \lesssim 0$. At $\phi_{\mathrm{pred,b2b}} \approx 0$ the efficiency falls down to ~ 0.6 and goes back up to ~ 0.9 at $\phi_{\mathrm{pred,b2b}} \gtrsim 0$. Finally, it falls back down to around 0.4 at $\phi_{\mathrm{pred,b2b}} \approx 0.5$. The last efficiency drop for phase2 data appears at $\phi_{\mathrm{pred,b2b}} \approx 2$. Here the efficiency falls down to ~ 0.3. For transverse momenta between $3\,\mathrm{GeV}$ and $4\,\mathrm{GeV}$ the calculated tracking efficiency for phase2 MC is above 0.98 for all values of $\phi_{\mathrm{pred,b2b}}$. For phase2 data the tracking efficiency is above 0.95 for $|\phi_{\mathrm{pred,b2b}}| \gtrsim 1$, but the structure in the efficiency we saw in the previous transverse momenta range can be seen once again. This time the drops of the efficiency is not as dominant and it never falls below 0.85.
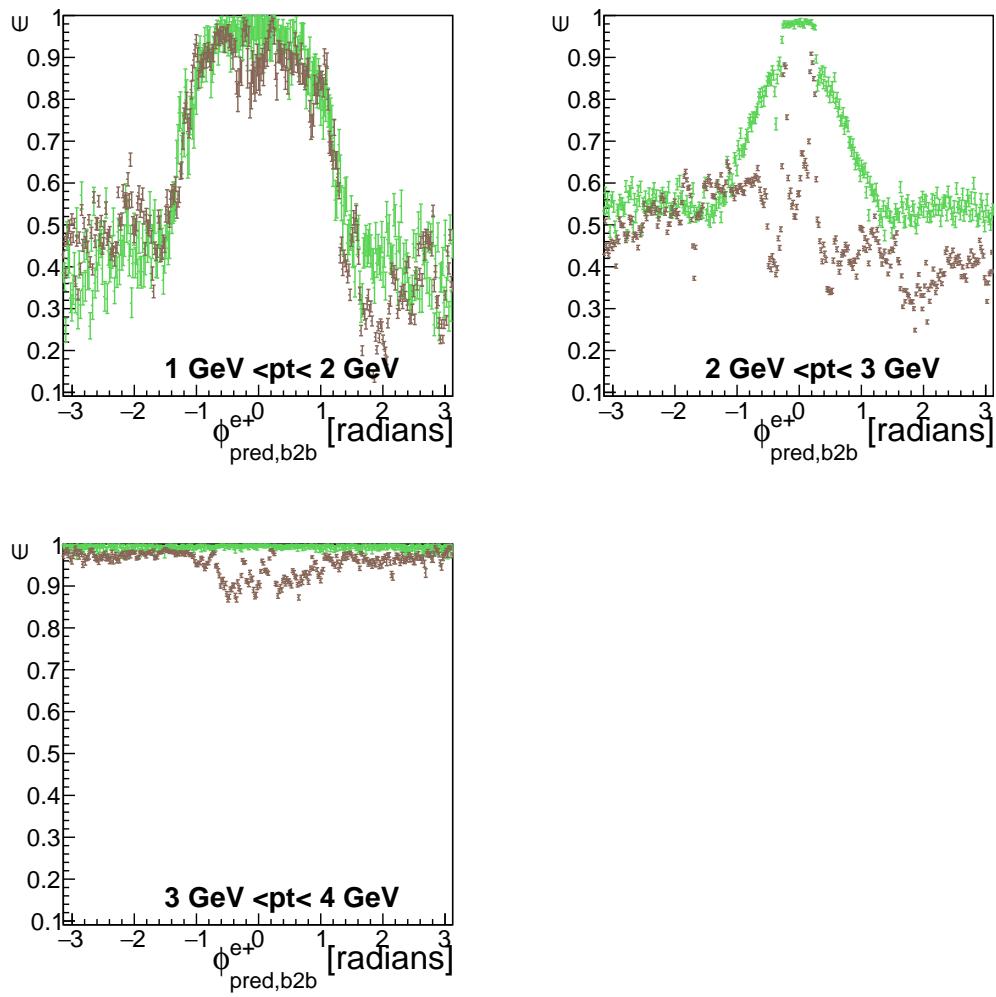
Figure 7.11.: Positron tracking efficiency plots as function of $\phi_{\mathrm{pred,b2b}}$ for different transverse momenta in the backward end-cap. The tracking efficiency for phase2 data is shown in brown and phase2 MC in green.

7.3.4. Tracking Efficiencies As Function Of $\theta_{\mathrm{pred,b2b}}$

Figure 7.12 shows the calculated electron tracking efficiencies for different transverse momenta as function of $\theta_{\mathrm{pred,b2b}}$. For transverse momenta between $1\,\mathrm{GeV}$ and $2\,\mathrm{GeV}$ almost all electrons are detected in the forward end-cap. The tracking efficiency for phase2 data is very low with only about 0.3 at $\theta_{\mathrm{pred,b2b}} \approx 0.25$. Then it jumps up to ~ 0.75 at $\theta_{\mathrm{pred,b2b}} \approx 0.3$. After this it increases further until it reaches its maximum of about 0.9 at $\theta_{\mathrm{pred,b2b}} \approx 0.5$. The tracking efficiency for phase2 MC starts high with 0.9 at $\theta_{\mathrm{pred,b2b}} \approx 0.25$ but it first falls down to ~ 0.7 at $\theta_{\mathrm{pred,b2b}} \approx 0.3$. After this it immediately jumps back up to ~ 0.9. Then it falls back to ~ 0.8 at $\theta_{\mathrm{pred,b2b}} \approx 0.4$ and after this it rises back up to over 0.9 at $\theta_{\mathrm{pred,b2b}} \approx 0.5$. For transverse momenta between $2\,\mathrm{GeV}$ and $3\,\mathrm{GeV}$ the tracking efficiency of phase2 data starts with ~ 0.7 at $\theta_{\mathrm{pred,b2b}} \approx 0.25$. It reaches its local minimum of ~ 0.4 at $\theta_{\mathrm{pred,b2b}} \approx 0.3$. After this the efficiency increases and has a maximum of over 0.9 at $\theta_{\mathrm{pred,b2b}} \approx 0.5$. The efficiency drops for increasing values of $\theta_{\mathrm{pred,b2b}}$. First, rapidly in the forward end-cap then slowly in the barrel. It reaches a local minimum of ~ 0.6 at $\theta_{\mathrm{pred,b2b}} \approx 1.0$. The tracking efficiency of phase2 MC starts with ~ 0.85 and reaches a local maximum of ~ 0.95 at $\theta_{\mathrm{pred,b2b}} \approx 0.5$. Similar to phase2 data, it falls down after this and reaches a local minimum of ~ 0.6 at $\theta_{\mathrm{pred,b2b}} \approx 1.0$. In the backward end-cap the tracking efficiency of phase2 MC starts with 0.9 and falls down rapidly to 0 at $\theta_{\mathrm{pred,b2b}} \approx 2.6$. The tracking efficiency of phase2 data has a similar structure but it is lower by about 0.4. Therefore, it reaches 0 earlier. For transverse momenta between $3\,\mathrm{GeV}$ and $4\,\mathrm{GeV}$ the tracking efficiency for both phase2 MC and phase2 data start with almost 1 in the forward end-cap. They are close to each other and they decrease a little with increasing $\theta_{\mathrm{pred,b2b}}$. Starting at $\theta_{\mathrm{pred,b2b}} \approx 0.7$, both tracking efficiencies fall down rapidly and they both reach a local minimum of ~ 0.7 at $\theta_{\mathrm{pred,b2b}} \approx 1.0$. After this the phase2 data tracking efficiency slowly gets back up reaching a local maximum at $\theta_{\mathrm{pred,b2b}} \approx 2.0$. After this maximum the efficiency of phase2 data falls down and has a dip at the transition between the barrel and the backward end-cap. Phase2 MC on the other hand stays the same in the middle region of the barrel. But it also has a local maximum starting at $\theta_{\mathrm{pred,b2b}} \approx 2.0$. The tracking efficiency starts to fall down at $\theta_{\mathrm{pred,b2b}} \approx 2.3$. For transverse momenta between $4\,\mathrm{GeV}$ and $5\,\mathrm{GeV}$ most electrons only hit the barrel and the forward end-cap. the tracking efficiency of phase2 data in the forward end-cap is always above 0.9. The efficiency for phase2 MC is worse for some values of $\theta_{\mathrm{pred,b2b}}$ due to the large errors. In the barrel both tracking efficiencies stay above 0.95 with the exception of a wide local minimum of 0.9 at $\theta_{\mathrm{pred,b2b}} \approx 1.3$. Additionally, the tracking efficiency for phase2 data is almost always a little worse than the tracking efficiency of phase2 MC. For transverse momenta between $5\,\mathrm{GeV}$ and $6\,\mathrm{GeV}$ almost all electrons are detected in the barrel. Except for some angles of $\theta_{\mathrm{pred,b2b}}$, the tracking efficiency for phase2 MC and phase2 data stays above 0.96. The tracking efficiency of phase2 data is always a little lower than the phase2 MC tracking efficiency.

Figure 7.13 shows the calculated positron tracking efficiency for different transverse momenta as function of $\theta_{\mathrm{pred,b2b}}$. For transverse momenta between $1\,\mathrm{GeV}$ and $2\,\mathrm{GeV}$

most of the positrons are detected in the backward end-cap. The tracking efficiency of phase2 data is about 0.85 before it falls down at the end of the backward end-cap. The tracking efficiency for phase2 MC has a similar structure but it is also a little higher. For transverse momenta between 2 GeV and 3 GeV the tracking efficiency for phase2 data starts low but it increases rapidly until it reaches a local maximum of about 0.85 at $\theta_{\text{pred,b2b}} \approx 0.5$. After this the tracking efficiency drops down. It has a local minimum of about 0.6 at $\theta_{\text{pred,b2b}} \approx 1.0$. For $\theta_{\text{pred,b2b}} \approx 2.0$ the tracking efficiency is over 0.9 but it falls down for increasing $\theta_{\text{pred,b2b}}$ and it has a significant dip at the barrel and backward end-cap transition. Then it goes back up until it finally drops down to 0 at the end of the backward end-cap. The phase2 MC tracking efficiency has a similar structure. But the calculated tracking efficiency of phase2 MC is higher compared to phase2 data for almost all values of $\theta_{\text{pred,b2b}}$. Additionally, the dip of the tracking efficiency at the transition between barrel and backward end-cap is not as dominant in phase2 MC. For transverse momenta between 3 GeV and 4 GeV the tracking efficiency for phase2 data starts with ~ 0.9 at $\theta_{\text{pred,b2b}} \approx 0.5$ and rises to a local maximum of ~ 0.95 at the forward end-cap and barrel transition. After this the tracking efficiency drops and reaches a local minimum at $\theta_{\text{pred,b2b}} \approx 1.0$. Then it slowly increases until it reaches an efficiency of over 0.95 at $\theta_{\text{pred,b2b}} \approx 2.1$. The efficiency stays at this value until the transition between the barrel and the backward end-cap. Here it falls down a little and the efficiency reaches a local minimum of ~ 0.88 in the backward end-cap at $\theta_{\text{pred,b2b}} \approx 2.4$. Finally, the efficiency goes back up to over 0.99. The tracking efficiency for phase2 MC follows a similar path. With the exception that it starts in the forward end-cap at a higher value of over 0.95. Additionally, there is no local minimum for phase2 MC in the backward end-cap. But it appears to fall down at the end of the backward end-cap. For transverse momenta between 4 GeV and 5 GeV the tracking efficiency for phase2 MC and phase2 data are close to each other. In the barrel both are constantly above 0.92 with a wide minimum at $\theta_{\text{pred,b2b}} \approx 1.0$. At $\theta_{\text{pred,b2b}} \approx 2.0$, the tracking efficiency even reaches above 0.98 for both phase2 data and phase2 MC. In the backward end-cap the tracking efficiency of phase2 MC appears to fall down earlier than the phase2 data tracking efficiency. For transverse momenta between 5 GeV and 6 GeV almost all positrons hit the barrel. The tracking efficiency for both phase2 data and phase2 MC stays above 0.95 for all values with high statistic.
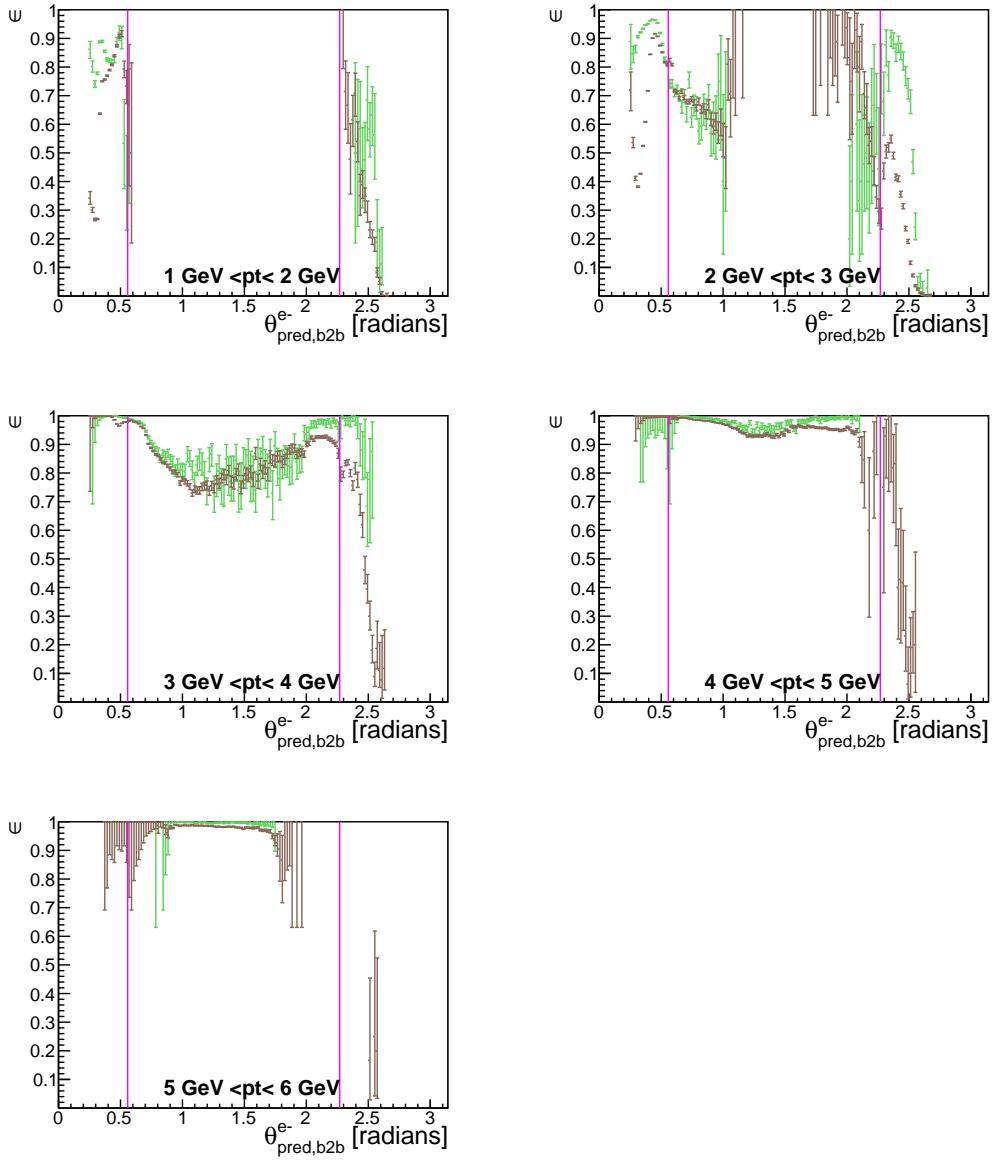
Figure 7.12.: Electron tracking efficiency plots as function of $\theta_{\mathrm{pred,b2b}}$ for different transverse momenta. The tracking efficiency for phase2 data is shown in brown and phase2 MC in green. The pink line indicates the different sectors of the ECL.
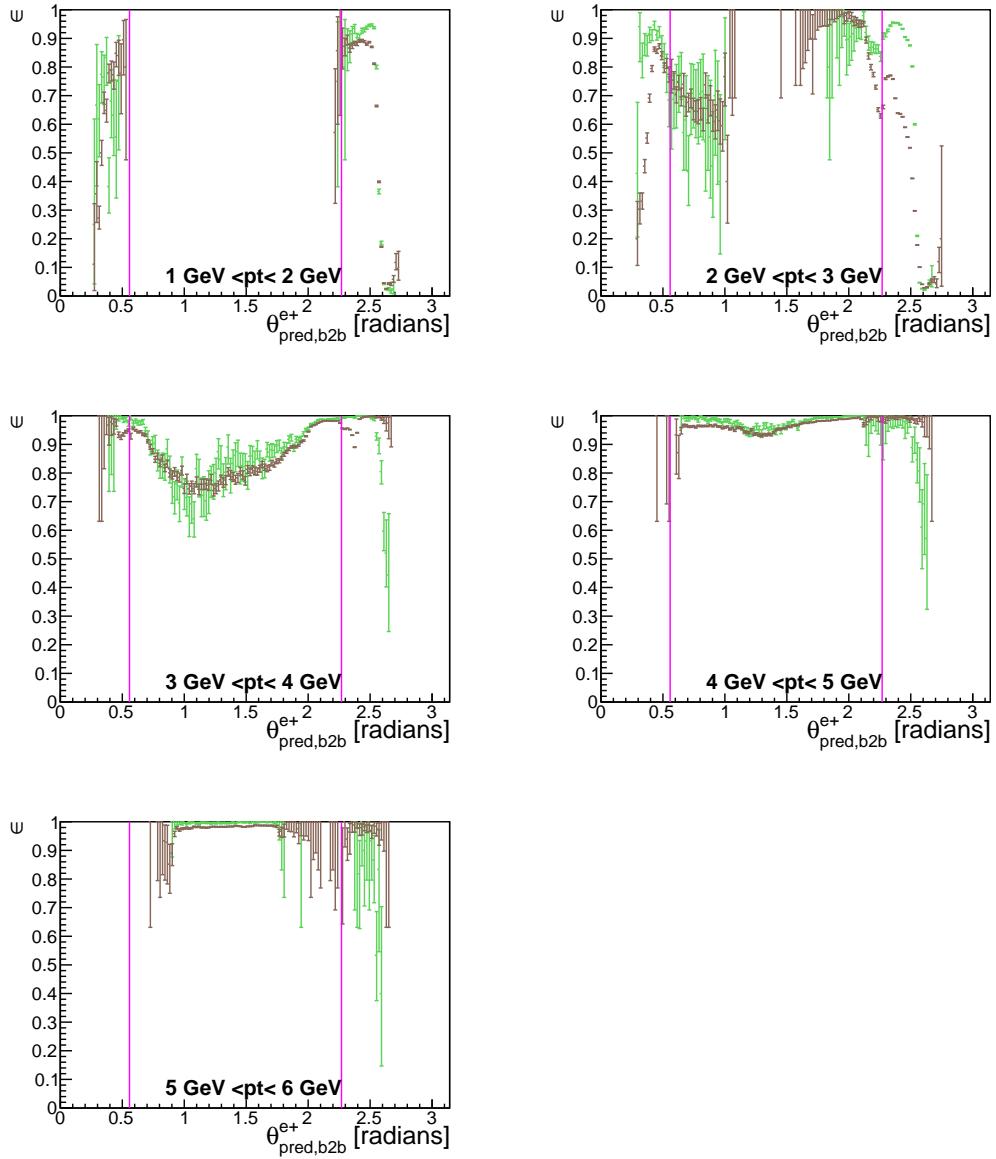
Figure 7.13.: Positron tracking efficiency plots as function of $\theta_{\mathrm{pred,b2b}}$ for different transverse momenta tracking efficiency plots. The tracking efficiency for phase2 data is shown in brown and phase2 MC in green. The pink line indicates the different sectors of the ECL.

8 Phase3 Tracking Efficiency

THIS chapter will start with a brief description of phase3. Then the selection will be applied to phase3 data and phase3 MC. Finally, the calculated tracking efficiency of electrons and positrons will be presented.

8.1. Phase3

Phase3 started successfully on March 11th, 2019. In contrast to phase2 the whole SVD and all ladders of the innermost in addition to two ladders of the outermost layer of the PXD were installed during phase3. A sketch of the PXD arrangement is shown in the appendix figure A.22. Due to construction problems, it was not possible the install the whole PXD. Phase3 is the first physics run of the Belle II project, in which the Belle II experiment takes data with a mostly fully equipped detector.[35]

8.2. Tracking Efficiencies

In this section the calculated tracking efficiencies for phase3 will be presented. To have as many events as possible, all phase3 data and phase3 MC files are taken into account. The selection described in chapter 6 will be applied to select Bhabha events. Figure 8.1 shows the number of selected virtual photon candidates per event after the selection. As shown in this figure, in both phase3 MC and phase3 data only one candidate is selected per event.

Phase3 data will be shown in blue together with phase3 MC in red. Only efficiencies with $\Delta\epsilon < 0.4$ are plotted.
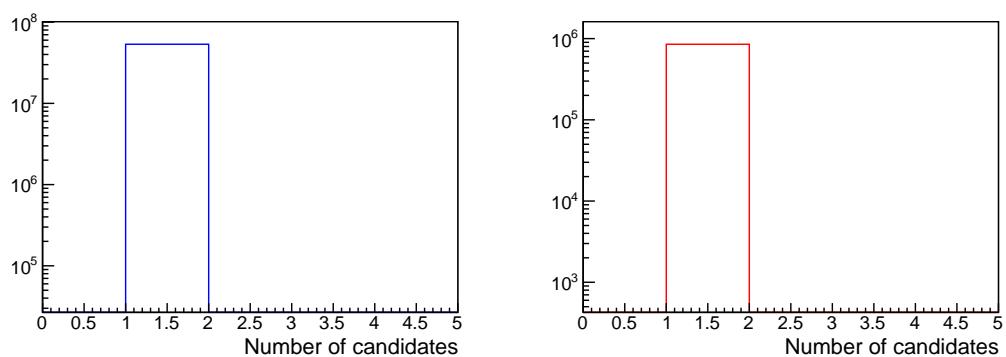
Figure 8.1.: The number of candidates per event after the selection is shown. Left: Phase3 data. Right: Phase3 MC. A total of 852093 candidates are selected for phase3 MC and $5.3 \cdot 10^7$ candidates are selected for phase3 data. Originally, 10^7 $e^+e^- \rightarrow e^+e^-$ events were generated on Monte Carlo.

8.2.1. Tracking Efficiencies As Function Of $\theta_{\mathbf{pred,b2b}}$-$\phi_{\mathbf{pred,b2b}}$

Figure 8.2 shows the calculated tracking efficiencies of phase3 as function of $\theta_{\mathrm{pred,b2b}}$-$\phi_{\mathrm{pred,b2b}}$. Similar to section 7.1, the phase3 MC efficiency is shown on the left and phase3 data on the right. The electron efficiencies are presented in the first row and the positron in the second row. Again, these plots combine all momenta.

For the phase3 data electron tracking efficiency horizontal efficiency drops can be seen in the forward end-cap and in the barrel at $\phi_{\mathrm{pred,b2b}} \approx -1.8, -1.0, -0.2, 0.6, 0.1$ and 3.0.

As can be seen in this figure, there are also horizontal efficiency losses for the positron phase3 data tracking efficiency. But they only appear in the backward end-cap at $\phi_{\mathrm{pred,b2b}} \approx -3.0, -1.7, -0.5, 1.4$ and 2.6. On phase3 MC there are no horizontal efficiency drops in the backward end-cap. These horizontal efficiency drops in the backward end-cap can also be seen in the electron phase3 data tracking efficiency plots but unfortunately the statistics on phase3 MC is too low to see efficiencies in the backward end-cap at all.
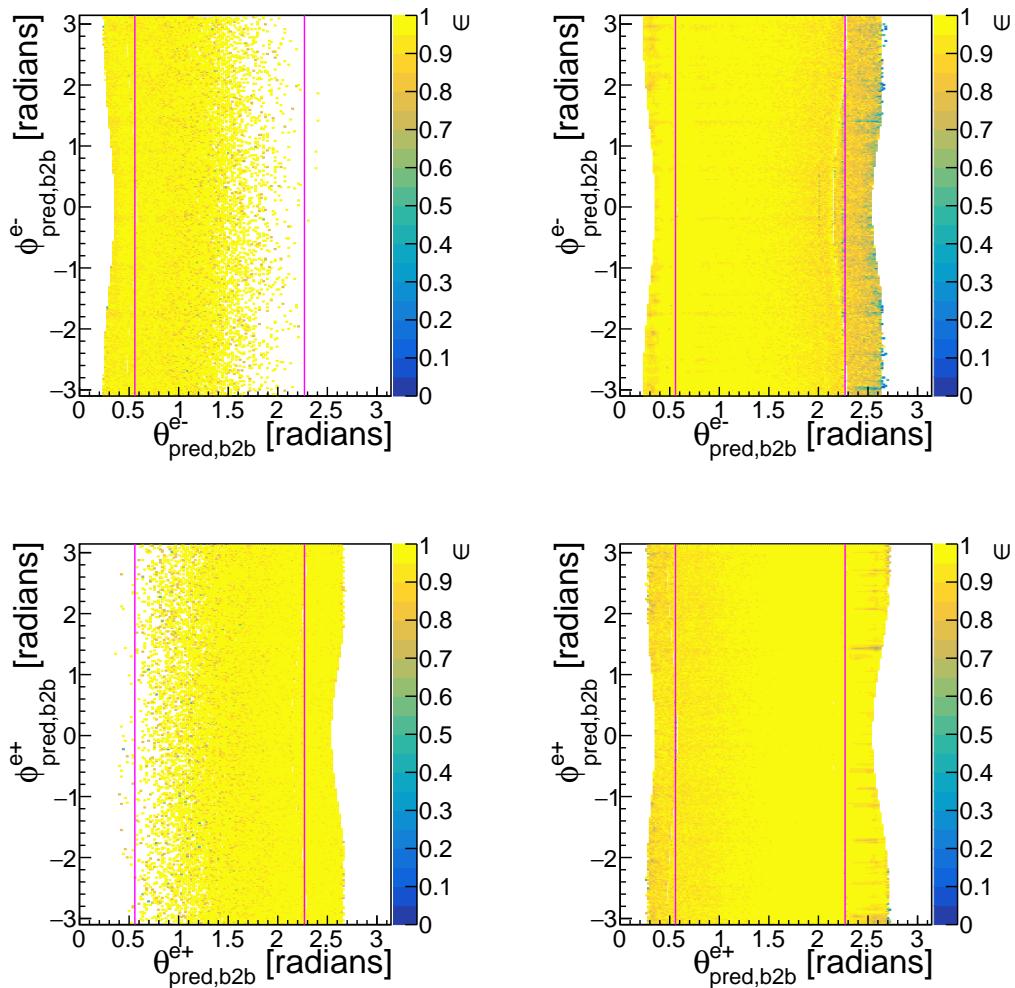
Figure 8.2.: Tracking efficiency plots as function of $\theta_{\mathrm{pred,b2b}}$-$\phi_{\mathrm{pred,b2b}}$ for phase3. Left: Phase3 MC. Right: Phase3 data. First row: electron efficiencies. Second row: positron efficiencies. The 2D plots with the corresponding error can be found in the appendix figure A.23. The pink line indicates the different sectors of the ECL.

8.2.2. ϵ In Bins Of Track Momentum

8.2.2.1. Forward End-Cap

Figure 8.3 shows the calculated electron tracking efficiency for different momenta as function of $\phi_{\mathrm{pred,b2b}}$ in the forward end-cap. For momenta between $4\,\mathrm{GeV}$ and $5\,\mathrm{GeV}$ the tracking efficiency for phase3 data starts at ~ 0.85 and drops until it reaches a minimum of ~ 0.7 at $\phi_{\mathrm{pred,b2b}} \approx 0$. After this it goes back up to ~ 0.85. An unusual structure occurs for the phase3 data tracking efficiency. It seems like the tracking efficiency drops by ~ 0.1 every other value of $\phi_{\mathrm{pred,b2b}}$. The result are two *ribbons* of efficiency in this region. The tracking efficiency of phase3 MC may has a similar structure but due to the lower statistics the error bars are way bigger. For momenta between $5\,\mathrm{GeV}$ and $6\,\mathrm{GeV}$ the structure of the tracking efficiencies are similar to the ones of the previous momentum range. But this time, the tracking efficiency starts at ~ 0.9 for phase3 data and an efficiency of about ~ 0.82 is reached in the minimum at $\phi_{\mathrm{pred,b2b}} \approx 0$. Additionally, for this momentum range, there are no *ribbons* of efficiency in the minimum. For momenta between $6\,\mathrm{GeV}$ and $7\,\mathrm{GeV}$ the tracking efficiency for phase3 MC stays above 0.95 for almost all values of $\phi_{\mathrm{pred,b2b}}$. The tracking efficiency for phase3 data ranges between ~ 0.89 and ~ 0.98. Some efficiencies appear to be scattered randomly in this range. For momenta between $7\,\mathrm{GeV}$ and $8\,\mathrm{GeV}$ the tracking efficiency for phase3 data is almost 1 for $|\phi_{\mathrm{pred,b2b}}| \gtrsim 1.5$. For $|\phi_{\mathrm{pred,b2b}}| \lesssim 1.5$, the tracking efficiency varies between 0.99 and 1. The phase3 MC tracking efficiency ranges from 0.97 to 1 for most values of $\phi_{\mathrm{pred,b2b}}$. The error bars are significantly larger for $|\phi_{\mathrm{pred,b2b}}| \gtrsim 1.5$. The best electron tracking efficiency for phase3 in the forward end-cap is obtained for electrons with a momentum between $7\,\mathrm{GeV}$ and $8\,\mathrm{GeV}$.
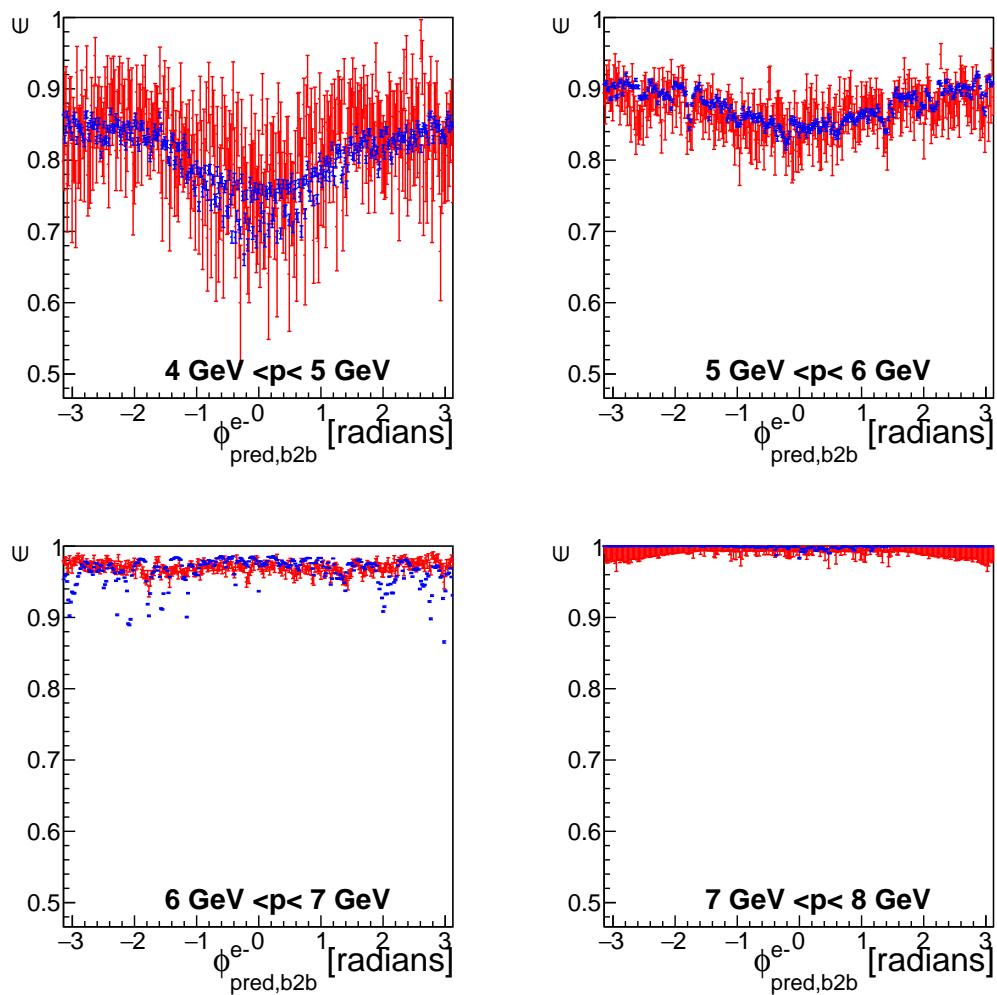
Figure 8.3.: Electron tracking efficiency plots as function of $\phi_{\mathrm{pred,b2b}}$ for different momenta in the forward end-cap. The tracking efficiency for phase3 data is shown in blue and phase3 MC in red.

8.2.2.2. Barrel

Figure 8.4 shows the electron tracking efficiencies for different momenta as function of $\phi_{\mathrm{pred,b2b}}$ in the barrel. For momenta between $4\,\mathrm{GeV}$ and $5\,\mathrm{GeV}$ the phase3 MC tracking efficiency ranges between 0.75 and 0.95. For phase3 data the tracking efficiency ranges between ~ 0.80 and ~ 0.92. The lowest efficiency occurs at $\phi_{\mathrm{pred,b2b}} \approx 0$, the highest efficiency at $|\phi_{\mathrm{pred,b2b}}| \approx \pi$. The tracking efficiencies for higher momenta have a similar structure. For momenta between $5\,\mathrm{GeV}$ and $6\,\mathrm{GeV}$ the tracking efficiency is between ~ 0.90 and ~ 0.99 for phase3 MC and between ~ 0.93 and ~ 0.98. The best tracking efficiency appears at momenta between $6\,\mathrm{GeV}$ and $7\,\mathrm{GeV}$. Here the calculated tracking efficiency is between ~ 0.98 and 1 for phase3 MC and between ~ 0.99 and 1 for phase3 data.

Figure 8.5 shows the positron tracking efficiency for different momenta as function of $\phi_{\mathrm{pred,b2b}}$ in the barrel. For momenta between $3\,\mathrm{GeV}$ and $4\,\mathrm{GeV}$ the calculated tracking efficiency for phase3 MC is between ~ 0.7 and ~ 0.97. The lowest efficiency occurs at $\phi_{\mathrm{pred,b2b}} \approx 0$ and the highest at $|\phi_{\mathrm{pred,b2b}}| \approx \pi$. The phase3 data has a similar structure but the efficiency is between ~ 0.8 and ~ 0.9. For momenta between $4\,\mathrm{GeV}$ and $5\,\mathrm{GeV}$ the tracking efficiency is between ~ 0.96 and 1 for phase3 MC and between ~ 0.98 and ~ 0.99. The structure of the efficiency is similar to the previous momenta but not as dominant. For momenta between $5\,\mathrm{GeV}$ and $6\,\mathrm{GeV}$ the tracking efficiency is between ~ 0.94 and 1 for phase3 MC and between ~ 0.97 and ~ 0.99 for phase3 data. The structure of the efficiency of phase3 data is different compared to the structure of the efficiency for lower momenta. Now the highest efficiency occurs at $\phi_{\mathrm{pred,b2b}} \approx 0$ and the lowest efficiency at $|\phi_{\mathrm{pred,b2b}}| \approx \pi$. For momenta between $6\,\mathrm{GeV}$ and $7\,\mathrm{GeV}$ the calculated positron tracking efficiency is between ~ 0.8 and 1 for phase3 MC and between ~ 0.95 and ~ 0.98 for phase3 data. The efficiency distribution is flat in both cases.
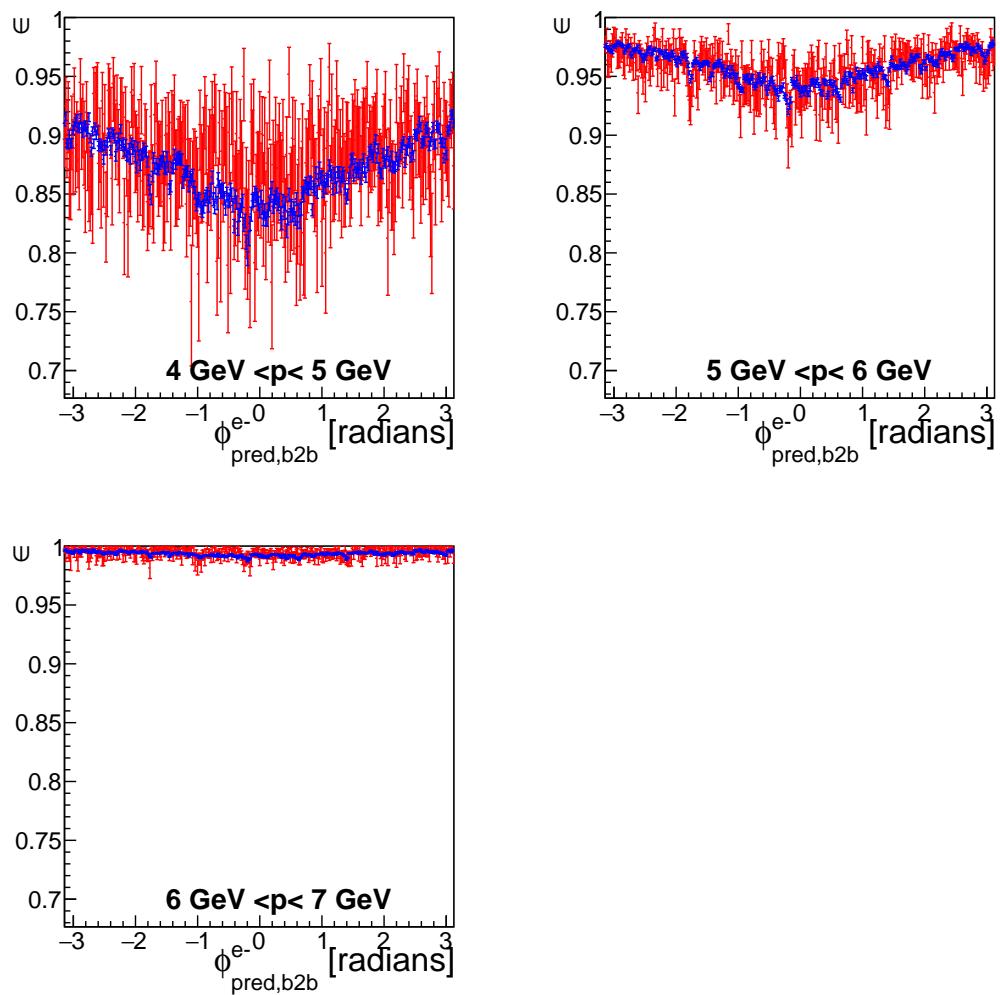
Figure 8.4.: Electron tracking efficiency plots as function of $\phi_{\text{pred,b2b}}$ for different momenta in the barrel. The tracking efficiency for phase3 data is shown in blue and phase3 MC in red.
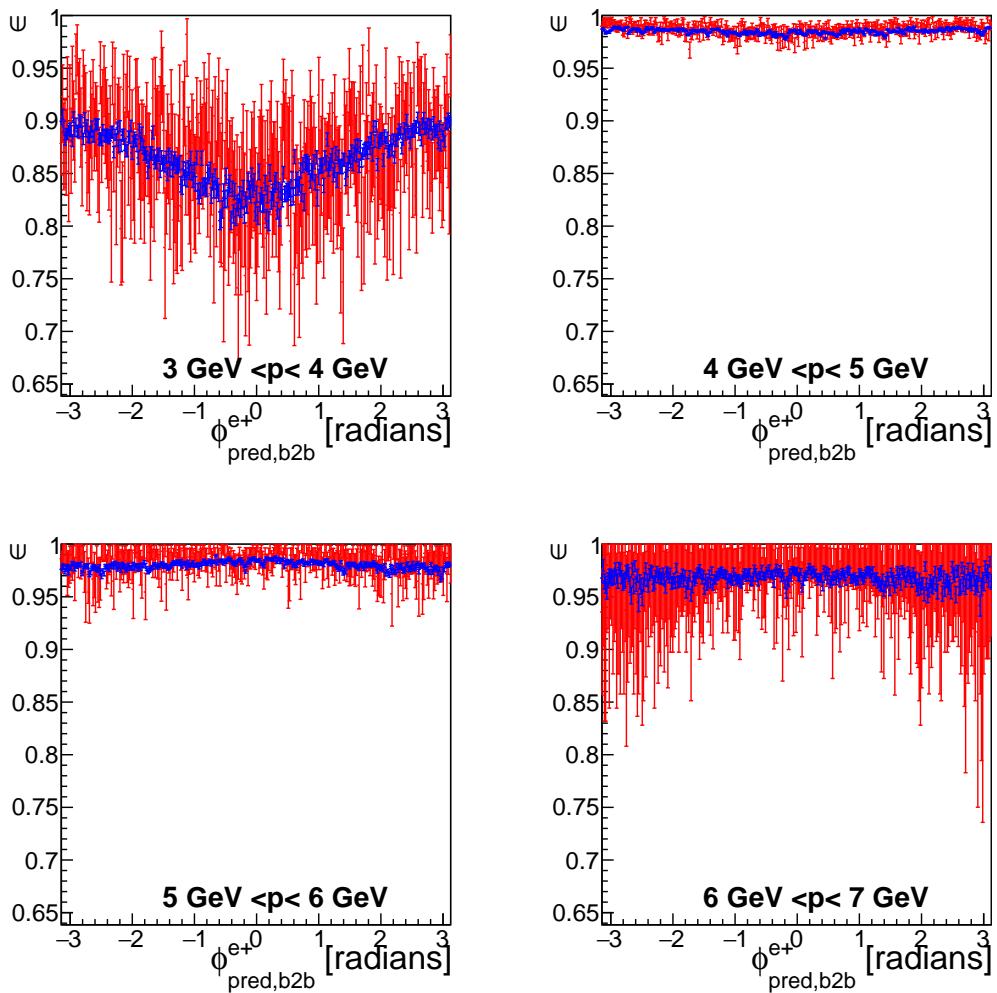
Figure 8.5.: Positron tracking efficiency plots as function of $\phi_{\mathrm{pred,b2b}}$ for different momenta in the barrel. The tracking efficiency for phase3 data is shown in blue and phase3 MC in red.

8.2.2.3. Backward End-Cap

Figure 8.6 shows the positron tracking efficiency for different momenta as function of $\phi_{\mathrm{pred,b2b}}$ in the backward end-cap. For momenta between $2\,\mathrm{GeV}$ and $3\,\mathrm{GeV}$ the phase3 MC tracking efficiency is above 0.9 for most values of $\phi_{\mathrm{pred,b2b}}$. The biggest error bars appear at $\phi_{\mathrm{pred,b2b}} \approx 0$. For phase3 data the tracking efficiency is above 0.99 for all values of $\phi_{\mathrm{pred,b2b}}$. For momenta between $3\,\mathrm{GeV}$ and $4\,\mathrm{GeV}$ the tracking efficiency of phase3 MC ranges between ~ 0.9 and 1. The lowest efficiency occurs at $\phi_{\mathrm{pred,b2b}} \approx 0$ again and the highest efficiency at $|\phi_{\mathrm{pred,b2b}}| \approx \pi$. The tracking efficiency of phase3 data has a strange structure. It is scattered between ~ 0.75 and ~ 0.97 but the error bars are small. Most of the time, the efficiency is above 0.9 but the efficiency drops by over 0.1 every other value of $\phi_{\mathrm{pred,b2b}}$. For momenta between $4\,\mathrm{GeV}$ and $5\,\mathrm{GeV}$ the tracking efficiency for phase3 MC is between 0.95 and 1. Similar to the previous momenta range the lowest tracking efficiency occurs at $\phi_{\mathrm{pred,b2b}} \approx 0$ and the highest efficiency at $|\phi_{\mathrm{pred,b2b}}| \approx \pi$. The tracking efficiency structure for phase3 data is also similar to the previous momenta range. But for this momenta range the tracking efficiency is between 0.9 and ~ 0.99 and without the scattered tracking efficiency values, the efficiency would be around 0.98. Also for this momenta range the number of efficiency drops is smaller compared to the previous momenta range. For momenta between $5\,\mathrm{GeV}$ and $6\,\mathrm{GeV}$ the tracking efficiency for phase3 MC is between ~ 0.6 and 1. But the error bars are very large and therefore a structure in the efficiency can not be determined. For phase3 data the tracking efficiency is above 0.99 for almost all values of $\phi_{\mathrm{pred,b2b}}$.
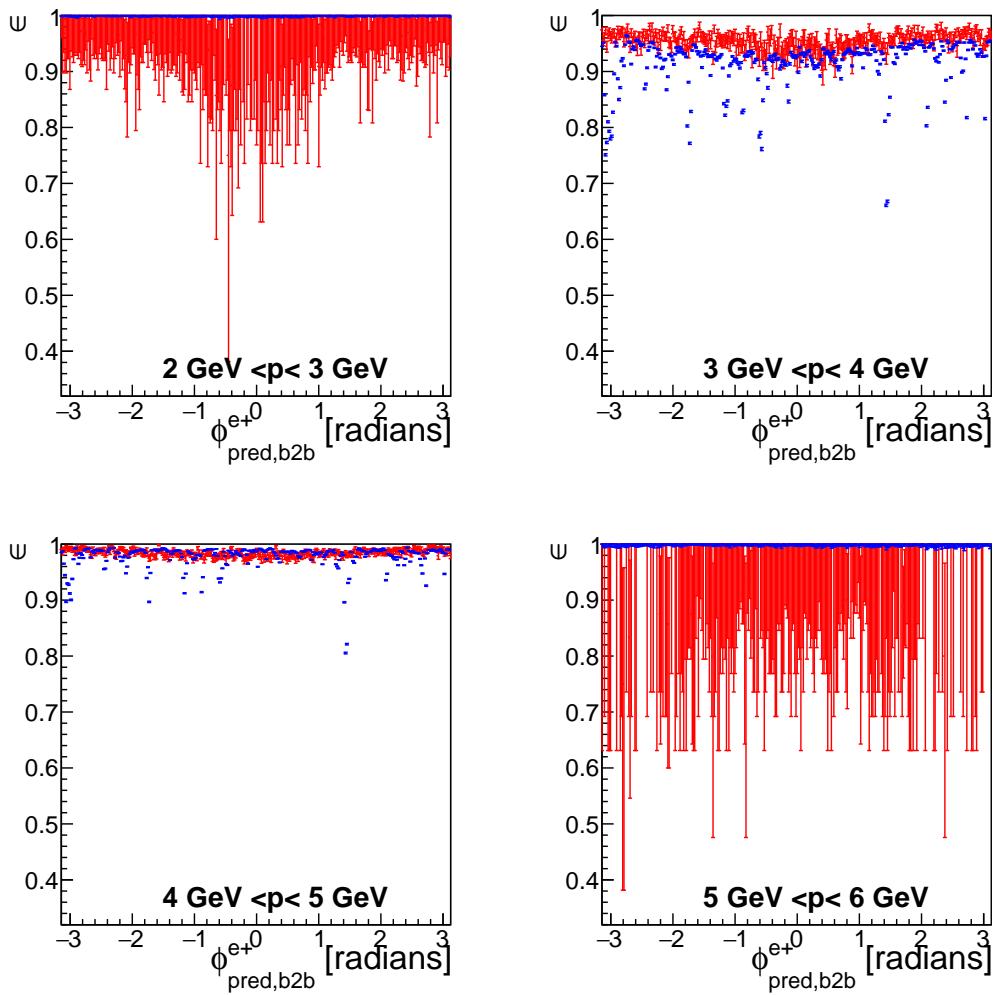
Figure 8.6.: Positron tracking efficiency plots as function of $\phi_{\mathrm{pred,b2b}}$ for different momenta in the backward end-cap. The tracking efficiency for phase3 data is shown in blue and phase3 MC in red.

8.2.2.4. Tracking Efficiencies As Function Of $\theta_{\mathrm{pred,b2b}}$

Figure 8.7 shows the calculated electron tracking efficiency for different momenta as function of $\theta_{\mathrm{pred,b2b}}$. For momenta between $3\,\mathrm{GeV}$ and $4\,\mathrm{GeV}$ the tracking efficiency for phase3 MC starts in the forward end-cap with over 0.95 for most values of $\theta_{\mathrm{pred,b2b}}$. At the forward end-cap and barrel transition the efficiency drops down to 0 and goes back up to ~ 0.6 at $\theta_{\mathrm{pred,b2b}} \approx 0.7$. After this the tracking efficiency slowly increases to between ~ 0.80 and ~ 0.95 at $\theta_{\mathrm{pred,b2b}} \approx 0.4$. Then the efficiency drops drastically down to 0. The tracking efficiency of phase3 data starts even higher with almost 1 in the forward end-cap. Similar to the tracking efficiency of phase3 MC, the phase3 data efficiency drops at the forward end-cap and barrel transition. After this the efficiency follows the phase3 MC efficiency until $\theta_{\mathrm{pred,b2b}} \approx 2.2$. At the barrel and backward end-cap transition the phase3 data tracking efficiency drops down to around 0.55. In the backward end-cap the efficiency goes back up to ~ 0.7 before it finally drops down to 0. For momenta between $4\,\mathrm{GeV}$ and $5\,\mathrm{GeV}$ both the phase3 MC and phase3 tracking efficiency starts at around 0.95 and declines with increasing $\theta_{\mathrm{pred,b2b}}$. A local minimum of $\epsilon \approx 0.6$ appears at the forward end-cap transition. After the transition the tracking efficiency jumps back to around 0.75 and then increases slowly until $\theta_{\mathrm{pred,b2b}} \approx 1.5$. Here the tracking efficiency stops for phase3 MC and it stays at the same height for the rest of the barrel. The tracking efficiency for phase3 MC finally drops down to 0 in the backward end-cap. In contrast, the phase3 data tracking efficiency already starts to fall down slowly at $\theta_{\mathrm{pred,b2b}} \approx 1.5$. At the barrel and backward end-cap transition, the phase3 data tracking efficiency drops down to ~ 0.8. After this it goes back up to ~ 0.85 and it processed to decline until it reaches 0 at the end of the backward end-cap. For momenta between $5\,\mathrm{GeV}$ and $6\,\mathrm{GeV}$ the tracking efficiency for both phase3 MC and phase3 data starts at around 0.95. They then decrease very fast until the transition between forward end-cap and barrel with a tracking efficiency of about 0.85. At this transition a peak in the tracking efficiency occurs. The tracking efficiency jumps up to about 0.95 and falls back down to ~ 0.9 after the transition. Then the efficiency goes up and reaches a plateau at $\theta_{\mathrm{pred,b2b}} \approx 1.3$ with an tracking efficiency of over 0.97. For momenta between $6\,\mathrm{GeV}$ and $7\,\mathrm{GeV}$ the phase3 MC and phase3 data tracking efficiency starts at around 0.95 and directly falls down to ~ 0.9 at $\theta_{\mathrm{pred,b2b}} \approx 0.3$. After this the tracking efficiency goes back up to almost 1 and it stays this high until $\theta_{\mathrm{pred,b2b}} \approx 1.3$. For momenta between $7\,\mathrm{GeV}$ and $8\,\mathrm{GeV}$ almost all electrons hit the forward end-cap. For phase3 data the tracking efficiency starts at almost 1 and stays that high for the whole forward end-cap. The tracking efficiency for phase3 MC also starts at almost 1 but the error bars become very large very fast with increasing $\theta_{\mathrm{pred,b2b}}$.

Figure 8.8 shows the positron tracking efficiency in the backward end-cap as function of $\theta_{\mathrm{pred,b2b}}$ for different momenta. For momenta between $2\,\mathrm{GeV}$ and $3\,\mathrm{GeV}$ most of the positrons are detected in the backward end-cap. For phase3 MC the tracking efficiency is above 0.97 for almost all values of $\theta_{\mathrm{pred,b2b}}$ in the backward end-cap. For phase3 data the tracking efficiency is even higher with over 0.99. For momenta between $3\,\mathrm{GeV}$ and $4\,\mathrm{GeV}$ the tracking efficiency for phase3 data starts in the forward

end-cap with over ~ 0.9 but it decreases with increasing $\theta_{\mathrm{pred,b2b}}$. In the barrel the tracking efficiency for phase3 data starts very low. This probably is due to the transition between forward end-cap and barrel. The efficiency jumps up to around 0.6 at $\theta_{\mathrm{pred,b2b}} \approx 0.7$. After this the tracking efficiency slowly increases. A difference between the tracking efficiency of phase3 MC and phase3 data occurs at the transition between the barrel and the backward end-cap and in the backward end-cap itself. Around the transition the phase3 data efficiency has a small dip while the phase3 MC tracking efficiency has a small peak. In the backward end-cap the phase3 MC tracking efficiency gets higher more quickly than the phase3 data tracking efficiency. A gap between the two of them is created. Additionally, there is another small dip in the phase3 data tracking efficiency at $\theta_{\mathrm{pred,b2b}} \approx 2.6$. For momenta between $4\,\mathrm{GeV}$ and $5\,\mathrm{GeV}$ the tracking efficiency of phase3 MC and phase3 data starts at around 0.9 and it drops down with increasing $\theta_{\mathrm{pred,b2b}}$. It reaches a minimum at the forward end-cap and barrel transition. After this transition the tracking efficiency gets higher until $\theta_{\mathrm{pred,b2b}} \approx 1.6$. After this the tracking efficiency continues to get higher starting with over 0.95 and ending with almost 1 at the transition between barrel and backward end-cap. In the backward end-cap the efficiency decreases slowly before it peaks at the very end of the backward end-cap. For phase3 data there even is a small dip before that very last peak. For momenta between $5\,\mathrm{GeV}$ and $6\,\mathrm{GeV}$ the tracking efficiency starts rather low in the forward end-cap, but in the barrel the tracking efficiency begins to rise. It reaches its plateau of $\epsilon \gtrsim 0.97$ at around $\theta_{\mathrm{pred,b2b}} \approx 1.3$. In the backward end-cap, the phase3 data tracking efficiency is noticeably higher than the phase3 tracking efficiency. Additionally, there is a small dip in the phase3 tracking efficiency at $\theta_{\mathrm{pred,b2b}} \approx 1.9$. For momenta between $6\,\mathrm{GeV}$ and $7\,\mathrm{GeV}$ the tracking efficiency increases in the forward end-cap from about 0.8 to 0.95 for phase3 data and to over 0.97 for phase3 MC. In the barrel the tracking efficiency continues to increase for phase3 data until it reaches 0.99. There is a dip in the tracking efficiency at $\theta_{\mathrm{pred,b2b}} \approx 1.1$ for phase3 data. At $\theta_{\mathrm{pred,b2b}} \approx 1.2$. The efficiency drops by over $5\,\%$. The phase3 MC tracking efficiency stays in the barrel above 0.97. In the backward end-cap phase3 data has a tracking efficiency of over 0.98.
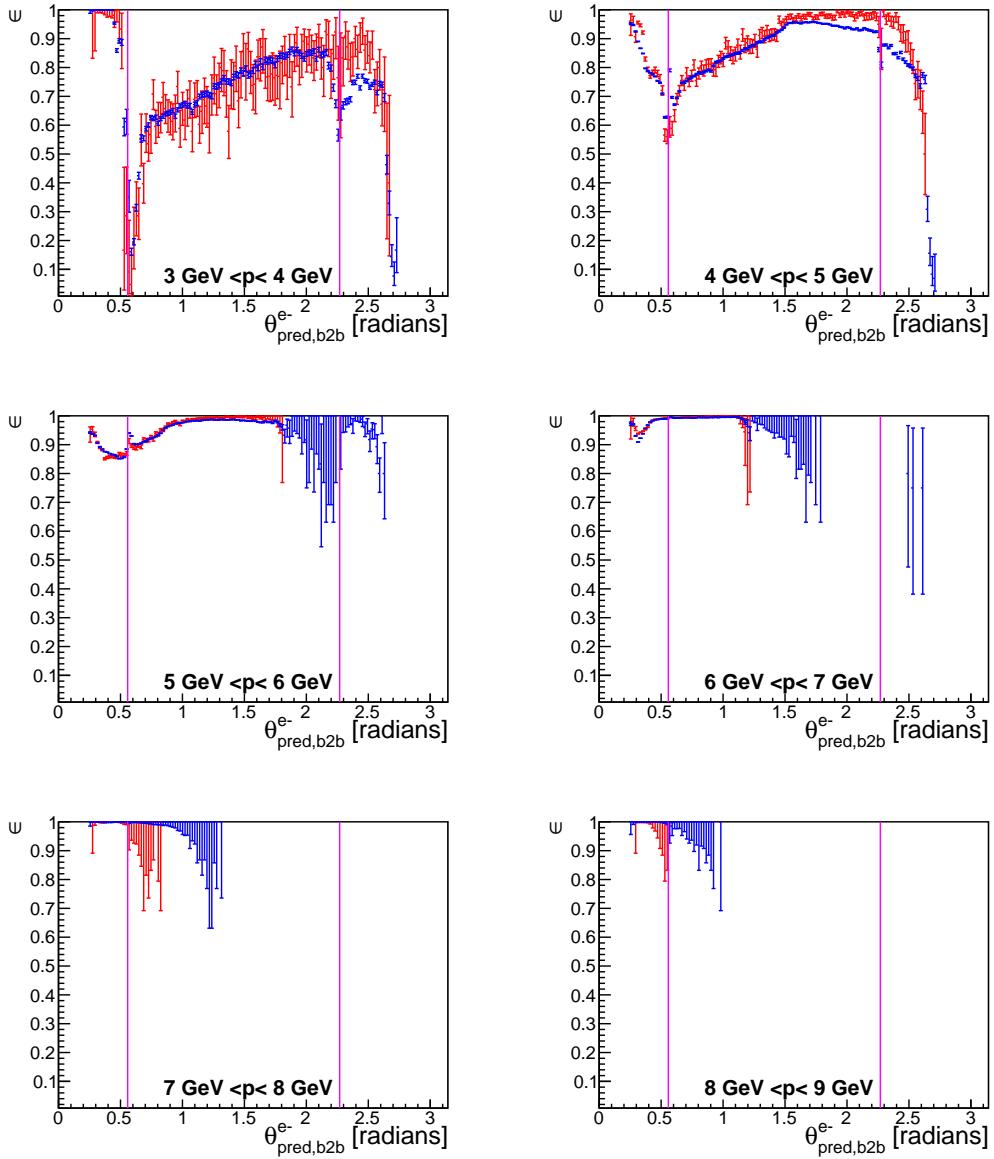
Figure 8.7.: Electron tracking efficiency plots as function of $\theta_{\mathrm{pred,b2b}}$ for different momenta. The tracking efficiency for phase3 data is shown in blue and phase3 MC in red. The pink line indicates the different sectors of the ECL.
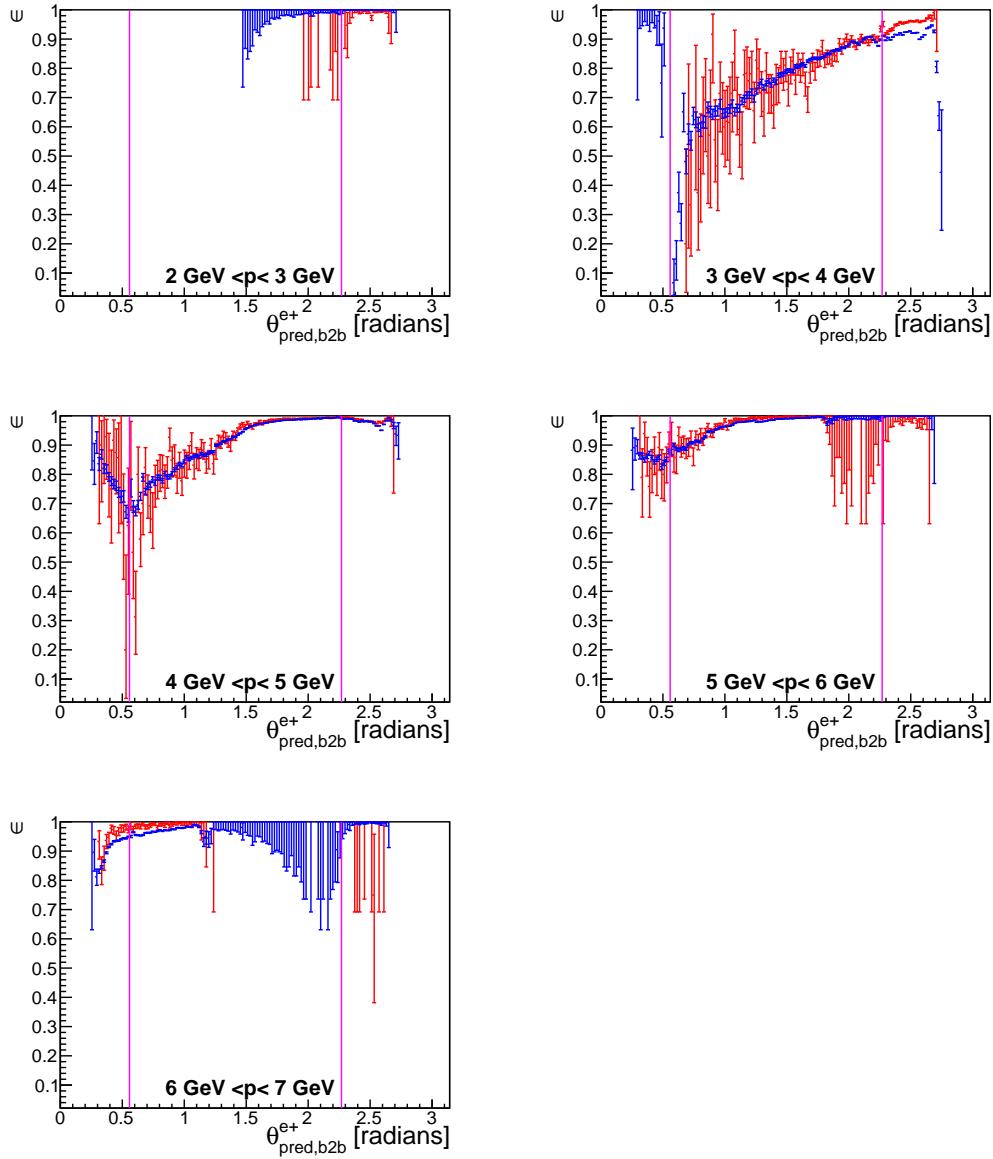
Figure 8.8.: Positron tracking efficiency plots as function of $\theta_{\mathrm{pred,b2b}}$ for different momenta. The tracking efficiency for phase3 data is shown in blue and phase3 MC in red. The pink line indicates the different sectors of the ECL.

8.2.3. ϵ In Bins Of Track Transverse Momentum

8.2.3.1. Forward End-Cap

Figure 8.9 shows the calculated tracking efficiency for electrons in the forward end-cap for different transverse momenta as function of $\phi_{\mathrm{pred,b2b}}$. For transverse momenta between $1\,\mathrm{GeV}$ and $2\,\mathrm{GeV}$ the tracking efficiency for phase3 data and phase3 MC is above ~ 0.85 for $|\phi_{\mathrm{pred,b2b}}| \gtrsim 1.5$. For decreasing $|\phi_{\mathrm{pred,b2b}}|$ the efficiency also decreases resulting in a minimum at $\phi_{\mathrm{pred,b2b}} \approx 0$. Similar to the first momentum plot of figure 8.3[1], there is a *ribbon* structure in the phase3 data tracking efficiency at $\phi_{\mathrm{pred,b2b}} \approx 0$. For transverse momenta between $2\,\mathrm{GeV}$ and $3\,\mathrm{GeV}$ the phase3 MC tracking efficiency is above 0.9 for all values of $\phi_{\mathrm{pred,b2b}}$. It has a minimum at $\phi_{\mathrm{pred,b2b}} \approx 0$ and the highest efficiencies are reached at $\phi_{\mathrm{pred,b2b}} \approx \pi$. The tracking efficiency for phase3 data is between ~ 0.88 and ~ 0.98. Again, some efficiencies appear to be scattered more or less randomly at this range. For transverse momenta between $3\,\mathrm{GeV}$ and $4\,\mathrm{GeV}$ the tracking efficiency for phase3 MC is above 0.96 for all values of $\phi_{\mathrm{pred,b2b}}$. For phase3 data the tracking efficiency even is above 0.98 for almost all values of $\phi_{\mathrm{pred,b2b}}$. There are some exceptions, which again appear to be scattered.

---

[1]This figure shows the phase3 electron tracking efficiencies for different momenta in the forward end-cap
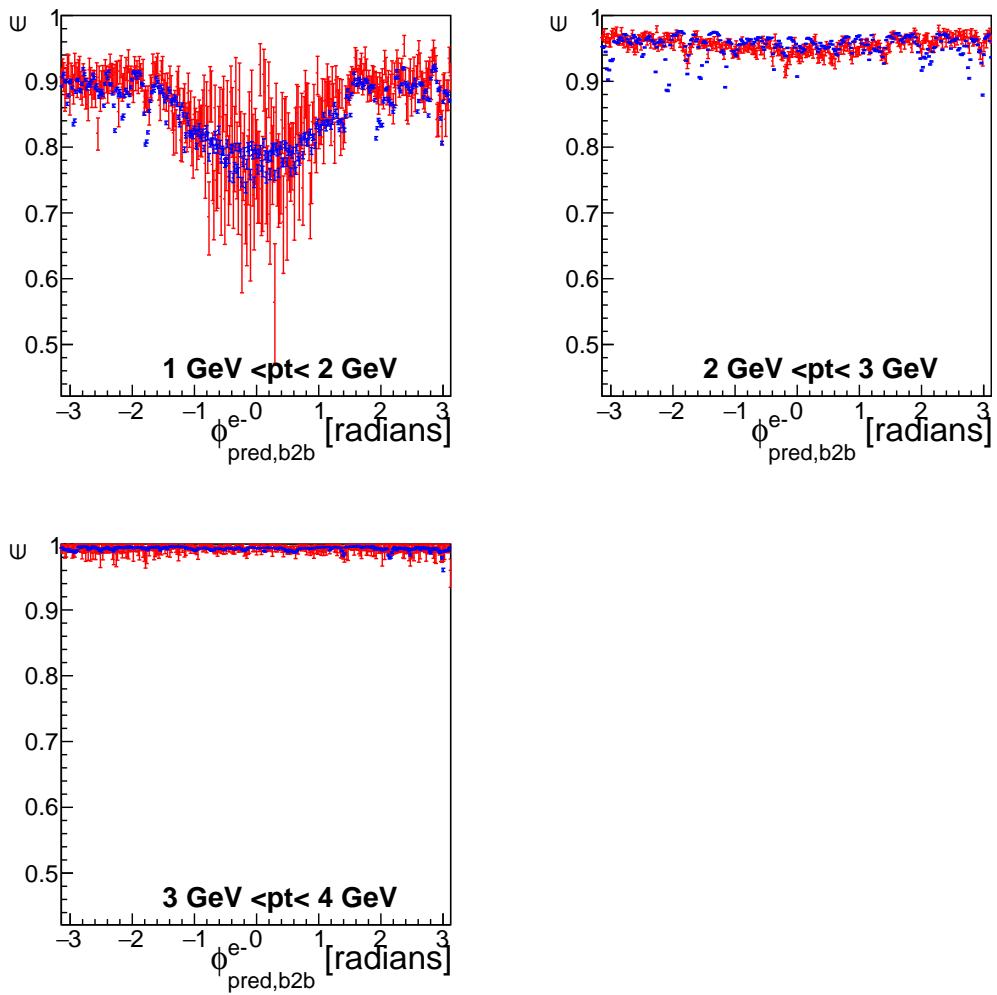
Figure 8.9.: Electron tracking efficiency plots as function of $\phi_{\mathrm{pred,b2b}}$ for different transverse momenta in the forward end-cap. The tracking efficiency for phase3 data is shown in blue and phase3 MC in red.

8.2.3.2. Barrel

Figure 8.10 shows the calculated electron tracking efficiency in the barrel for different transverse momenta. For transverse momenta between $2\,\mathrm{GeV}$ and $3\,\mathrm{GeV}$ the tracking efficiency for phase3 MC the errors are rather large but it is still possible to see that the minimum of the tracking efficiency is at $\phi_{\mathrm{pred,b2b}} \approx 0$. The tracking efficiency for phase3 data seems to oscillate between ~ 0.6 and ~ 0.8. The two maxima appear at $|\phi_{\mathrm{pred,b2b}}| \approx 2.0$ and the two minima at $\phi_{\mathrm{pred,b2b}} \approx 0$ and $|\phi_{\mathrm{pred,b2b}}| \approx \pi$. For transverse momenta between $3\,\mathrm{GeV}$ and $4\,\mathrm{GeV}$ the oscillation is still visible for phase3 data and phase3 MC, but it is not as dominant. The tracking efficiency oscillates between ~ 0.93 and ~ 0.97 for phase3 data and between ~ 0.90 and ~ 0.99 for phase3 MC. For transverse momenta between $4\,\mathrm{GeV}$ and $5\,\mathrm{GeV}$ the tracking efficiency stays flat for both phase3 data and phase3 MC. The efficiency is between ~ 0.97 and ~ 0.99 for phase3 data and between ~ 0.95 and ~ 1 for phase3 MC. For transverse momenta between $5\,\mathrm{GeV}$ and $6\,\mathrm{GeV}$ the calculated tracking efficiency is between ~ 0.98 and almost 1 for phase3 data and between ~ 0.95 and 1 for phase3 MC. Phase3 data has the best tracking efficiency at $|\phi_{\mathrm{pred,b2b}}| \approx \pi$ in contrast to phase3 MC which has the best tracking efficiency at $\phi_{\mathrm{pred,b2b}} \approx 0$ due to the large errors at $|\phi_{\mathrm{pred,b2b}}| \approx \pi$.
Figure 8.11 shows the calculated positron tracking efficiency in the barrel for different transverse momenta as function of $\phi_{\mathrm{pred,b2b}}$. For transverse momenta between $3\,\mathrm{GeV}$ and $4\,\mathrm{GeV}$ the calculated tracking efficiency ranges between ~ 0.93 and ~ 0.99 for phase3 MC and between ~ 0.96 and ~ 0.98 for phase3 data. Again, the lowest efficiencies occurs at $\phi_{\mathrm{pred,b2b}} \approx 0$. For transverse momenta between $4\,\mathrm{GeV}$ and $5\,\mathrm{GeV}$ the calculated tracking efficiency for phase3 MC is between ~ 0.96 and 1 and between ~ 0.97 and ~ 0.99 for phase3 data. For transverse momenta between $5\,\mathrm{GeV}$ and $6\,\mathrm{GeV}$ the tracking efficiency is between ~ 0.98 and 1 for phase3 data and between ~ 0.94 and 1 for phase3 MC. The error bars for phase3 MC are increasing in length with increasing $|\phi_{\mathrm{pred,b2b}}|$.
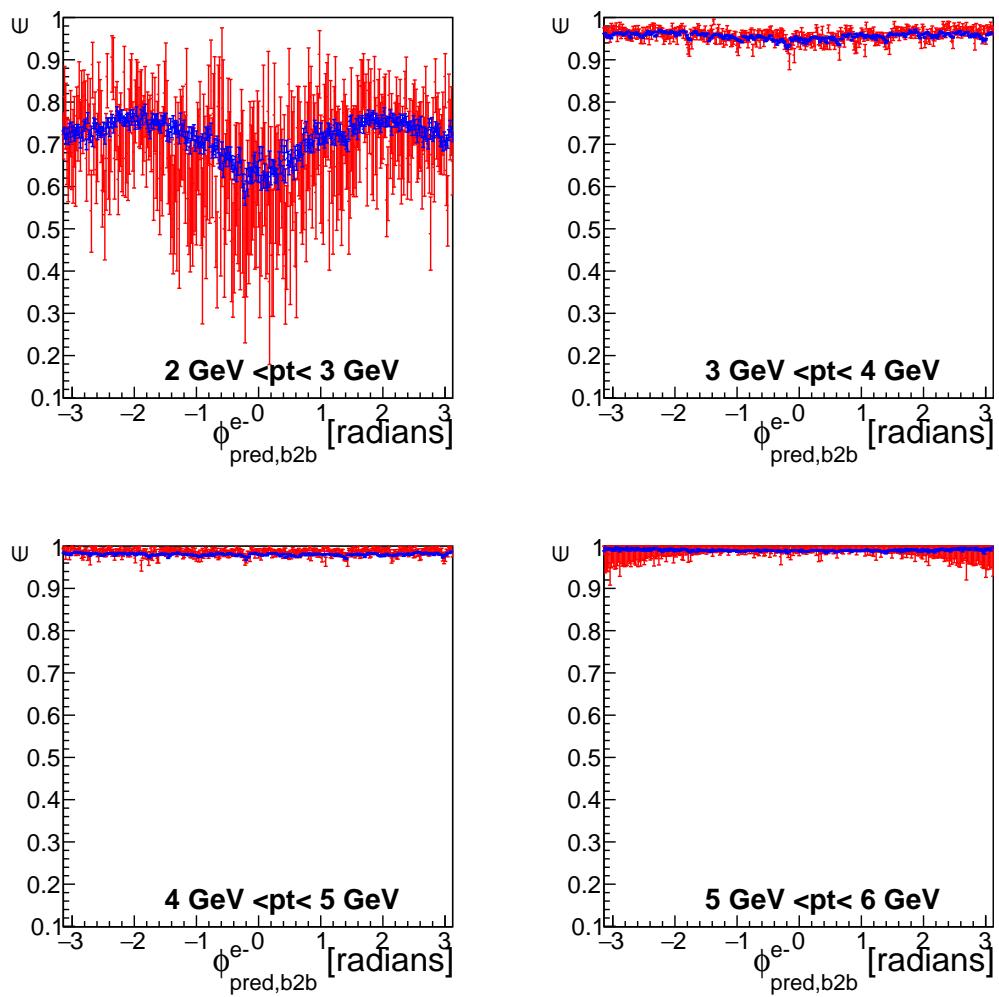
Figure 8.10.: Electron tracking efficiency plots as function of $\phi_{\mathrm{pred,b2b}}$ for different transverse momenta in the barrel. The tracking efficiency for phase3 data is shown in blue and phase3 MC in red.
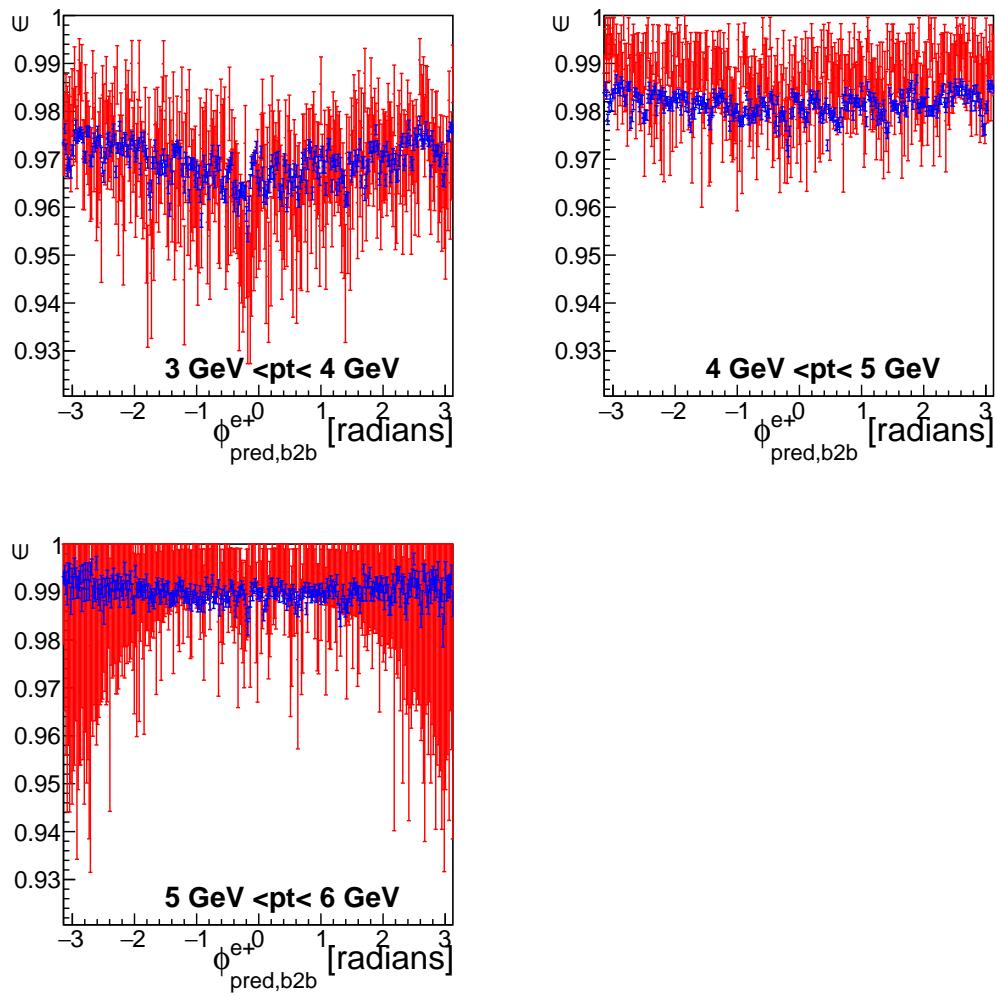
Figure 8.11.: Positron tracking efficiency plots as function of $\phi_{\mathrm{pred,b2b}}$ for different transverse momenta in the barrel. The tracking efficiency for phase3 data is shown in blue and phase3 MC in red.

8.2.3.3. Backward End-Cap

Figure 8.12 shows the calculated positron tracking efficiency in the backward end-cap for different momenta as function of $\phi_{\mathrm{pred,b2b}}$. For transverse momenta between $1\,\mathrm{GeV}$ and $2\,\mathrm{GeV}$ the calculated phase3 MC tracking efficiency is above 0.92 for $|\phi_{\mathrm{pred,b2b}}| \gtrsim 1$. For $|\phi_{\mathrm{pred,b2b}}| \lesssim 1$ the error bars are noticeably larger and the efficiency is between ~ 0.75 and 1. For phase3 data a noteworthy structure occurs. For phase3 data the highest tracking efficiency appears at $|\phi_{\mathrm{pred,b2b}}| \lesssim 0.5$. Here the efficiency is between ~ 0.96 and ~ 0.99. For $|\phi_{\mathrm{pred,b2b}}| \gtrsim 0.5$ the highest efficiency is ~ 0.97 and the tracking efficiencies seem to be scattered between ~ 0.75 and ~ 0.96. For transverse momenta between $2\,\mathrm{GeV}$ and $3\,\mathrm{GeV}$ the calculated tracking efficiency is between ~ 0.95 and ~ 0.99 for phase3 MC and between ~ 0.72 and ~ 0.98 for phase3 data. Again, the tracking efficiency for phase3 data appears to be scattered randomly. For transverse momenta between $3\,\mathrm{GeV}$ and $4\,\mathrm{GeV}$ the tracking efficiency for phase3 MC ranges between ~ 0.96 and 1. The tracking efficiency for phase3 data is above 0.99 most of the time. There are some rather smaller dips at $\phi_{\mathrm{pred,b2b}} \approx -\pi,\ -1.8,\ -1.2,\ -0.8,\ 1.2$ and 2.1.
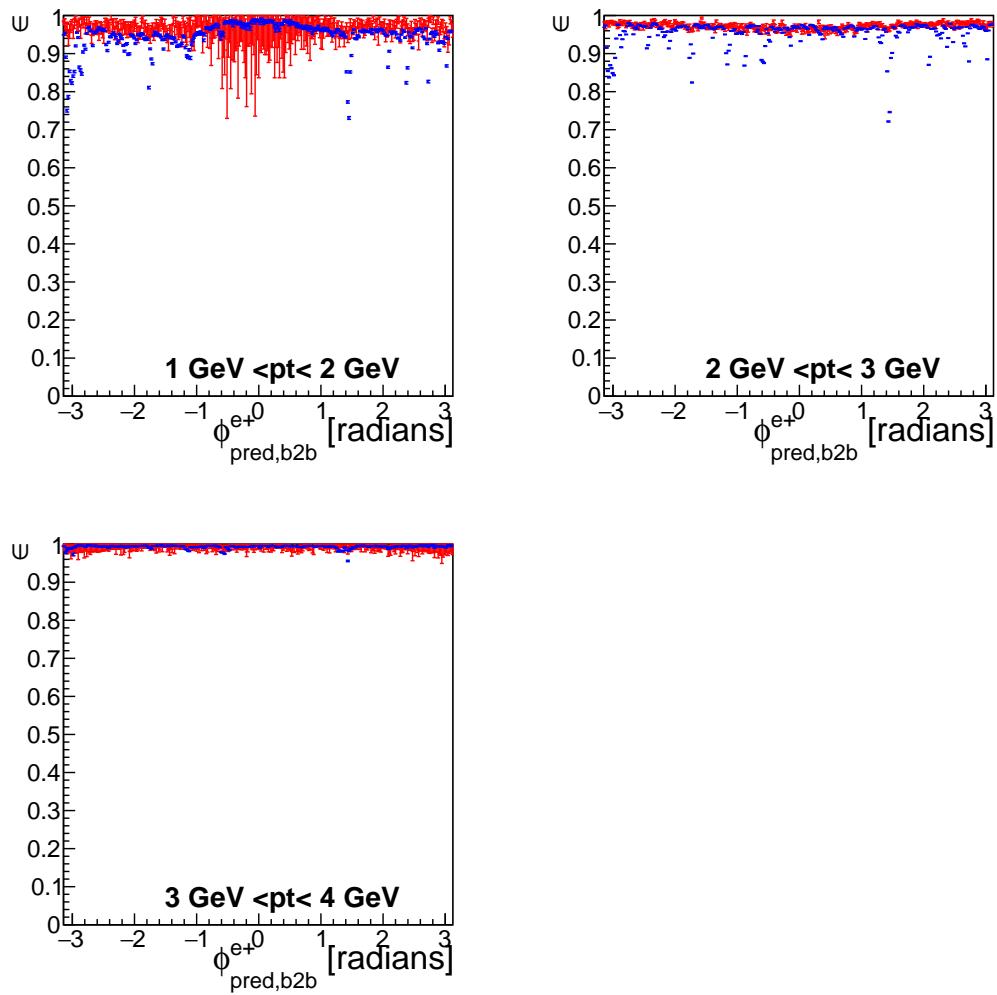
Figure 8.12.: Positron tracking efficiency plots as function of $\phi_{\mathrm{pred,b2b}}$ for different transverse momenta in the backward end-cap. The tracking efficiency for phase3 data is shown in blue and phase3 MC in red.

### 8.2.3.4. Tracking Efficiencies As Function Of $\theta_{\mathrm{pred,b2b}}$

Figure 8.13 shows the calculated electron tracking efficiency as function of $\theta_{\mathrm{pred,b2b}}$ for different transverse momenta. For transverse momenta between $1\,\mathrm{GeV}$ and $2\,\mathrm{GeV}$ almost all electrons hit one of the end-caps. In the forward end-cap both the phase3 MC and phase3 data tracking efficiency start at ~ 0.95 but both drop down to ~ 0.78 at $\theta_{\mathrm{pred,b2b}} \approx 0.4$. After this both efficiencies rise back up to over 0.9 at $\theta_{\mathrm{pred,b2b}} \approx 0.5$. At the forward end-cap and barrel transition, the efficiency drops down again. In the backward end-cap, the phase3 data tracking efficiency rises at first. It reaches a local maximum of about 0.8 at $\theta_{\mathrm{pred,b2b}} \approx 2.5$. For increasing $\theta_{\mathrm{pred,b2b}}$ the tracking efficiency drops down until it finally reaches 0 at the end of the backward end-cap. For transverse momenta between $2\,\mathrm{GeV}$ and $3\,\mathrm{GeV}$ the calculated tracking efficiency for phase3 MC starts very high with almost 1 at the beginning of the forward end-cap. But it also falls down to ~ 0.95 quickly. At $\theta_{\mathrm{pred,b2b}} \approx 0.45$ the phase3 MC tracking efficiency drops down drastically to ~ 0.7 at the forward end-cap barrel transition. After this it slowly decreases further. The phase3 data tracking efficiency also starts very high at the beginning of the forward end-cap. But it also has a small dip at $\theta_{\mathrm{pred,b2b}} \approx 0.3$. The phase3 data tracking efficiency also drops drastically at $\theta_{\mathrm{pred,b2b}} \approx 0.45$ until it reaches the barrel. In the barrel it continuous to drop slowly. After the barrel and backward end-cap transition both the phase3 MC and the phase3 data tracking efficiency first rise to a maximum of ~ 0.95 for phase3 MC and ~ 0.8 for phase3 data at $\theta_{\mathrm{pred,b2b}} \approx 2.45$. After this maximum both efficiencies drop. For transverse momenta between $3\,\mathrm{GeV}$ and $4\,\mathrm{GeV}$ the calculated tracking efficiency in the forward end-cap is above 0.99 for both phase3 data and phase3 MC for almost all values of $\theta_{\mathrm{pred,b2b}}$. In the barrel the phase3 data tracking efficiency starts to fall down and reaches a local minimum of about 0.72 at $\theta_{\mathrm{pred,b2b}} \approx 1.2$. After this the tracking efficiencies rises slowly up to ~ 0.85 at $\theta_{\mathrm{pred,b2b}} \approx 2.0$. The tracking efficiency of phase3 MC also falls down in the barrel but due to the large errors the minimum is somewhere between $1.0 \lesssim \theta_{\mathrm{pred,b2b}} \lesssim 2.0$. After $\theta_{\mathrm{pred,b2b}} \approx 2.0$ both tracking efficiencies jump up and stay at roughly the same height until $\theta_{\mathrm{pred,b2b}} \approx 2.4$. The phase3 data tracking efficiency goes up to ~ 0.9 and the phase3 MC efficiency goes up to over 0.95. The last maximum appears at $\theta_{\mathrm{pred,b2b}} \approx 2.45$. Here the tracking efficiency for phase3 data goes up to over 0.96 before it falls down at the end of the backward end-cap. For transverse momenta between $4\,\mathrm{GeV}$ and $5\,\mathrm{GeV}$ the calculated phase3 data tracking efficiency is above 0.98 for almost all values of $\theta_{\mathrm{pred,b2b}}$ in the forward end-cap. At the forward end-cap and barrel transition, the tracking efficiency drops down to ~ 0.95. But it jumps back to almost 1 for both phase3 data and phase3 MC afterwards. Then with increasing $\theta_{\mathrm{pred,b2b}}$ the tracking efficiency slowly falls down until it reaches its local minimum of ~ 0.92 at $\theta_{\mathrm{pred,b2b}} \approx 1.4$. After this minimum the tracking efficiencies go back up. Phase3 data already reaches its efficiency plateau of $\epsilon \approx 0.95$ at $\theta_{\mathrm{pred,b2b}} \approx 1.6$. Phase3 MC, on the other hand, rises up to almost 1 at $\theta_{\mathrm{pred,b2b}} \approx 1.9$. This results in a difference of the efficiencies between phase3 data and phase3 MC. For transverse momenta between $5\,\mathrm{GeV}$ and $6\,\mathrm{GeV}$ almost all electrons hit the barrel. The tracking efficiency starts with over 0.99 for both phase3 data and

phase3 MC at $\theta_{\mathrm{pred,b2b}} \approx 0.9$. The phase3 tracking efficiency stays the same with increasing $\theta_{\mathrm{pred,b2b}}$ but the phase3 data tracking efficiency slowly decreases until it reaches it minimum of ~ 0.96 at $\theta_{\mathrm{pred,b2b}} \approx 1.8$.

Figure 8.14 shows the calculated positron tracking efficiency as function of $\theta_{\mathrm{pred,b2b}}$ for different transverse momenta. For transverse momenta between $1\,\mathrm{GeV}$ and $2\,\mathrm{GeV}$ the tracking efficiency for phase3 data and phase3 MC both have a drop in the forward end-cap. Phase3 data is going from about 0.9 down to about 0.78. On phase3 MC a similar structure can be seen. In the backward end-cap the tracking efficiency stays above 0.95 for both phase3 data and phase3 MC with the exception of a drop at $\theta_{\mathrm{pred,b2b}} \approx 2.6$. For transverse momenta between $2\,\mathrm{GeV}$ and $3\,\mathrm{GeV}$ the tracking efficiency for phase3 data starts above 0.9 falls down and has a minimum at $\theta_{\mathrm{pred,b2b}} \approx 0.3$. The tracking efficiency of phase3 MC also appears to fall down at first with a minimum at the same polar angle $\theta_{\mathrm{pred,b2b}}$. With increasing $\theta_{\mathrm{pred,b2b}}$ both tracking efficiencies rise to a local maximum of ~ 0.94 for phase3 data and ~ 0.95 for phase3 MC at $\theta_{\mathrm{pred,b2b}} \approx 0.35$. At the end of the backward end-cap the efficiency falls down again and it continues to fall in the barrel. At the end of the barrel the tracking efficiency is above 0.95 at $\theta_{\mathrm{pred,b2b}} \approx 1.9$. It slowly decreases with increasing $\theta_{\mathrm{pred,b2b}}$ and at $\theta_{\mathrm{pred,b2b}} \approx 2.1$ it drops down to ~ 0.85. The error bars of the phase3 MC tracking efficiency are too large in the barrel to describe the structure. At $\theta_{\mathrm{pred,b2b}} \approx 2.1$ the phase3 tracking efficiency is below 0.9. With increasing $\theta_{\mathrm{pred,b2b}}$ both efficiencies rise until the reach a plateau of ~ 0.95 for phase3 data and ~ 0.96 for phase3 MC in the backward end-cap. Phase3 data has an additional minimum of ~ 0.92 in the backward end-cap at $\theta_{\mathrm{pred,b2b}} \approx 2.6$. Both phase3 MC and phase3 data have a maximum of ~ 0.98 at $\theta_{\mathrm{pred,b2b}} \approx 2.7$. For transverse momenta between $3\,\mathrm{GeV}$ and $4\,\mathrm{GeV}$ the phase3 MC tracking efficiency starts in the forward end-cap with over 0.97 but it decreases until it reaches its minimum at $0.9 \lesssim \theta_{\mathrm{pred,b2b}} \lesssim 1.4$ with efficiencies below ~ 0.65. After the minimum the efficiency goes back up. In the backward end-cap the phase3 MC tracking efficiency has a maximum of over 0.99. The tracking efficiency of phase3 data follows a similar path. But it starts a little lower in the forward end-cap with ~ 0.95 and it reaches its minimum of ~ 0.73 at $\theta_{\mathrm{pred,b2b}} \approx 1.1$. For transverse momenta between $4\,\mathrm{GeV}$ and $5\,\mathrm{GeV}$ almost all positrons hit the barrel or the backward end-cap. In the barrel the tracking efficiency starts at ~ 0.95 for phase3 data and at ~ 0.98 for phase3 MC at $\theta_{\mathrm{pred,b2b}} \approx 0.7$. With increasing $\theta_{\mathrm{pred,b2b}}$ both efficiencies fall down and have a minimum of ~ 0.92 at $\theta_{\mathrm{pred,b2b}} \approx 1.4$. Then both efficiencies rise back up again and they stay high with over 0.98. Note that there is a small dip in both efficiencies at $\theta_{\mathrm{pred,b2b}} \approx 2.15$. For transverse momenta between $5\,\mathrm{GeV}$ and $6\,\mathrm{GeV}$ most of the positrons hit the barrel. The tracking efficiency for phase3 MC and phase3 data stays above ~ 0.98. On phase3 data the tracking efficiency has a small dip at $\theta_{\mathrm{pred,b2b}} \approx 1.7$. The efficiency drops down by $\sim 5\%$.
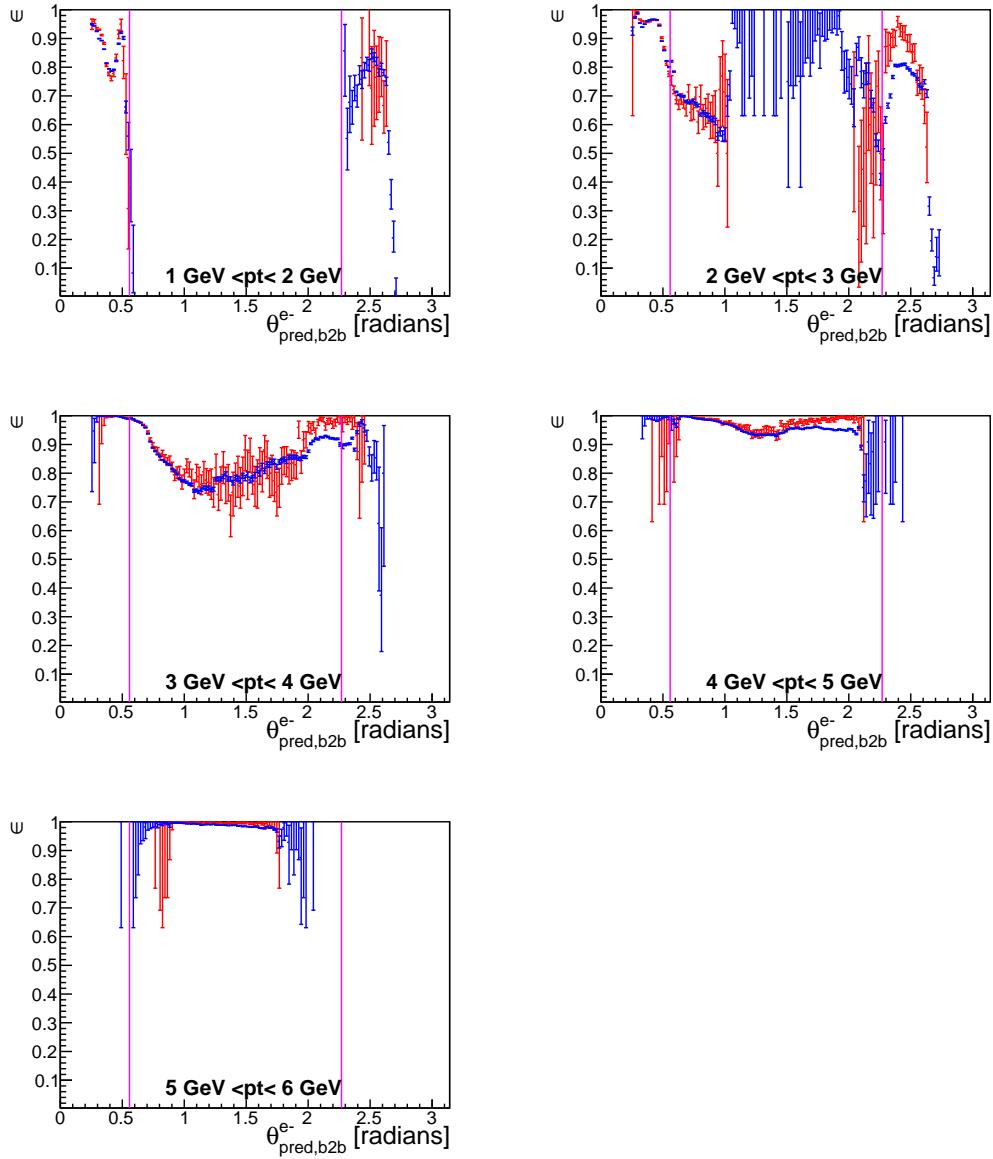
Figure 8.13.: Electron tracking efficiency plots as function of $\theta_{\mathrm{pred,b2b}}$ for different transverse momenta. The tracking efficiency for phase3 data is shown in blue and phase3 MC in red. The pink line indicates the different sectors of the ECL.
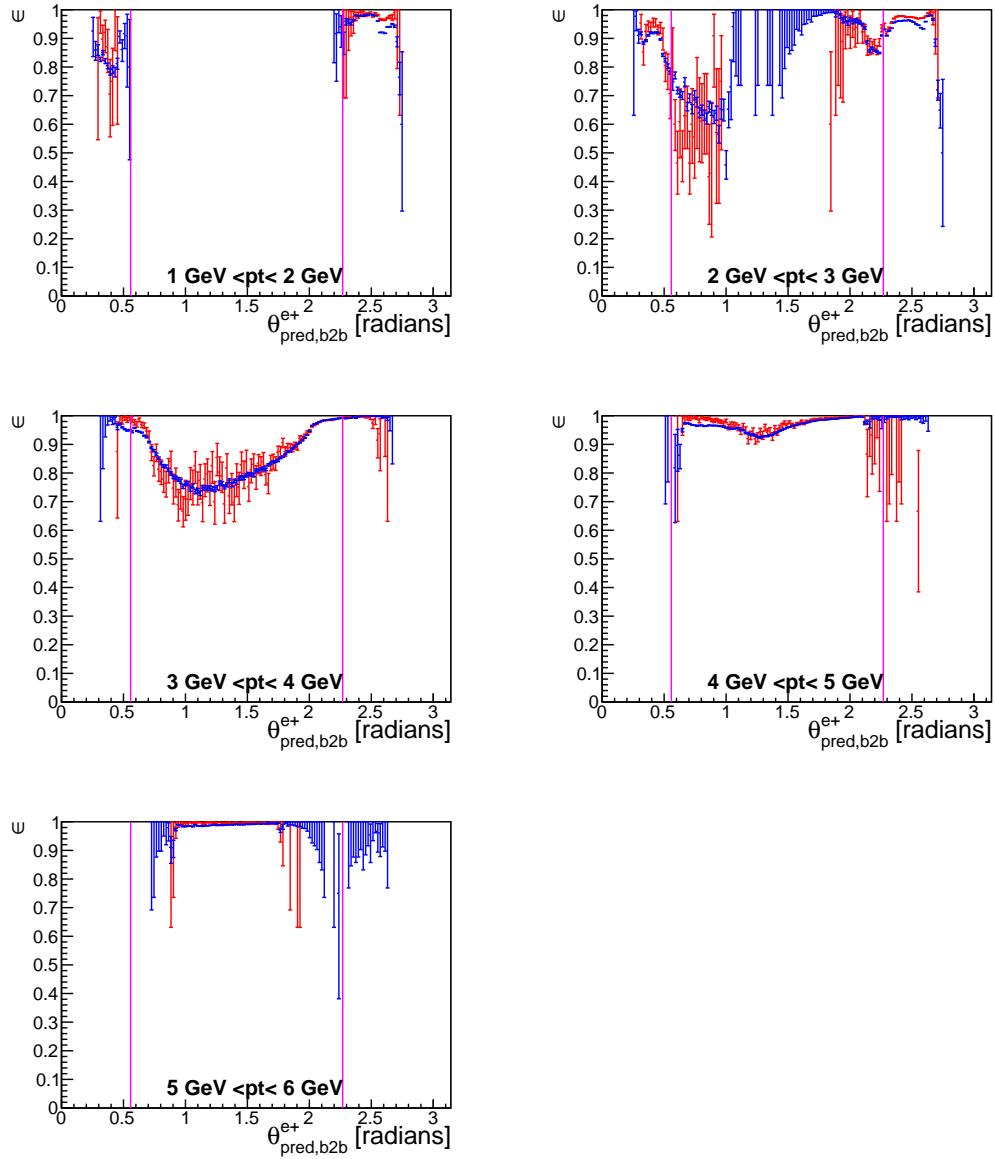
Figure 8.14.: Positron tracking efficiency plots as function of $\theta_{\mathrm{pred,b2b}}$ for different transverse momenta. The tracking efficiency for phase3 data is shown in blue and phase3 MC in red. The pink line indicates the different sectors of the ECL.

CHAPTER 9

Comparing The Tracking
Efficiencies Of Phase2 With Phase3

THIS chapter will provide a comparison between the calculated tracking efficiencies of phase2 and phase3. I will only present some plots and only the differences in the efficiencies will be described because the efficiencies were already discussed in the previous chapters. Additionally, only momenta plots for phase2 data in brown and phase3 data in blue will be shown together.

The biggest difference between phase2 and phase3 is the presence of the SVD and approximately half of the PXD detector in phase3. Since the SVD is also able to detect charged particle, we expect to have a higher tracking efficiency on phase3 compared to phase2.

9.1. Tracking Efficiencies As Function Of $\theta_{\mathrm{pred,b2b}}$

Figure 9.1 shows the electron tracking efficiency of phase2 data and phase3 data as function of $\theta_{\mathrm{pred,b2b}}$ for different momenta ranges. In the barrel there is no difference between the two tracking efficiencies. The biggest discrepancy occurs in the end-caps. Here we see a drastically improvement in the phase3 data tracking efficiency compared to phase2 data across all momenta. For momenta between 3 GeV and 6 GeV the phase3 data tracking efficiency falls down at a higher $\theta_{\mathrm{pred,b2b}}$ angle in the backward end-cap. And for momenta between 4 GeV and 8 GeV the tracking efficiency starts with a local maximum in the forward end-cap and it is overall higher than the phase2 data tracking efficiency. Since more electrons are hitting the forward end-cap compared to the backward end-cap, we will compare the electron tracking efficiency in the forward end-cap of phase2 data and phase3 data in the next section.

Figure 9.2 shows the positron tracking efficiency of phase2 data and phase3 data as function of $\theta_{\mathrm{pred,b2b}}$ for different momenta ranges. Again there is basically no difference between the efficiencies in the barrel. For momenta between 3 GeV and 5 GeV the tracking efficiency is improved drastically in the backward end-cap. The phase3 data tracking efficiency either stays at the same height coming from the barrel or it rises even higher. For momenta between 4 GeV and 7 GeV the tracking efficiency

in the forward end-cap is also improved. In the next section we will also discuss the differences in the positron tracking efficiency in the backward end-cap.

Figure 9.1.: Electron tracking efficiency plots as function of $\theta_{\mathrm{pred,b2b}}$ for different momenta. The tracking efficiency of phase2 data is shown in brown and phase3 data in blue. The pink line indicates the different sectors of the ECL.
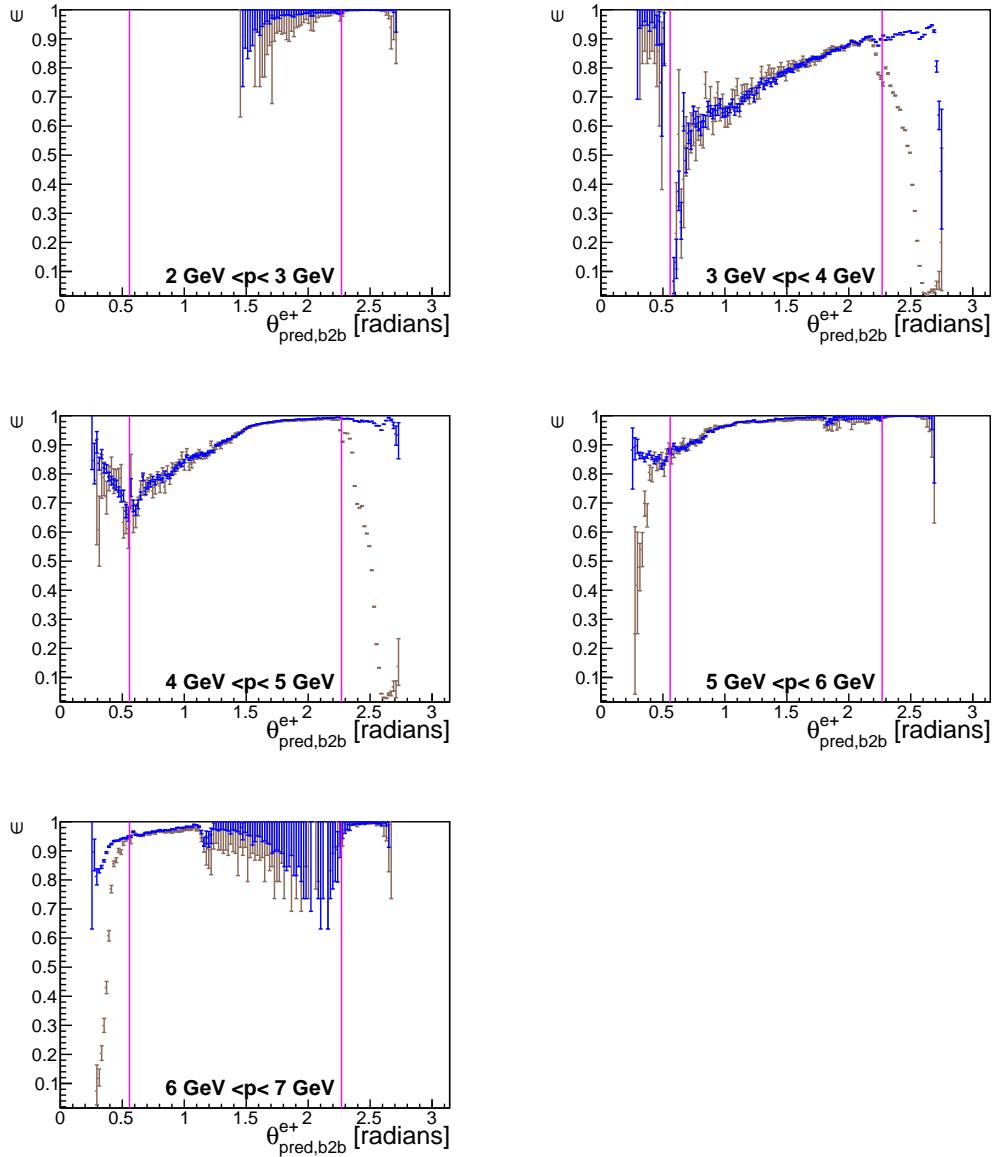
Figure 9.2.: Positron tracking efficiency plots as function of $\theta_{\mathrm{pred},b2b}$ for different momenta. The tracking efficiency of phase2 data is shown in brown and phase3 data in blue. The pink line indicates the different sectors of the ECL.

9.2. Tracking Efficiencies As Function Of $\phi_{\mathrm{pred,b2b}}$

Figure 9.3 shows the phase2 data and phase3 data electron tracking efficiency in the forward end-cap for different momenta as function of $\phi_{\mathrm{pred,b2b}}$. For momenta between $4\,\mathrm{GeV}$ and $6\,\mathrm{GeV}$ the phase3 data tracking efficiency is noticeably higher for $|\phi_{\mathrm{pred,b2b}}| \gtrsim 1$. Both phase2 data and phase3 data tracking efficiency have a local minimum at $\phi_{\mathrm{pred,b2b}} \approx 0$. For momenta between $6\,\mathrm{GeV}$ and $8\,\mathrm{GeV}$ the phase3 data tracking efficiency is overall higher than the phase2 data tracking efficiency and for momenta over $7\,\mathrm{GeV}$ the phase3 data tracking efficiency is above 0.99 for all values of $\phi_{\mathrm{pred,b2b}}$.

Figure 9.4 shows the phase2 data and phase3 data positron tracking efficiency in the backward end-cap for different momenta as function of $\phi_{\mathrm{pred,b2b}}$. The phase3 data tracking efficiency is higher for all $\phi_{\mathrm{pred,b2b}}$ and for all momenta. There are basically no similarities in structure of phase2 data compared to phase3 data for momenta between $3\,\mathrm{GeV}$ and $5\,\mathrm{GeV}$. The tracking efficiency of phase2 data ranges between ~ 0.2 and 0.95. It oscillates between ~ 0.2 and 0.6 and has two peaks at around $\phi_{\mathrm{pred,b2b}} \approx 0$. The phase3 data tracking efficiency is much higher and more flat compared to the tracking efficiency of phase2 data. The phase3 data tracking efficiency appears to drop for some $\phi_{\mathrm{pred,b2b}}$ values. For momenta between $2\,\mathrm{GeV}$ and $3\,\mathrm{GeV}$, and $5\,\mathrm{GeV}$ and $6\,\mathrm{GeV}$ both the tracking efficiencies for phase2 and phase3 data are over 0.95 for almost all values of $\phi_{\mathrm{pred,b2b}}$.
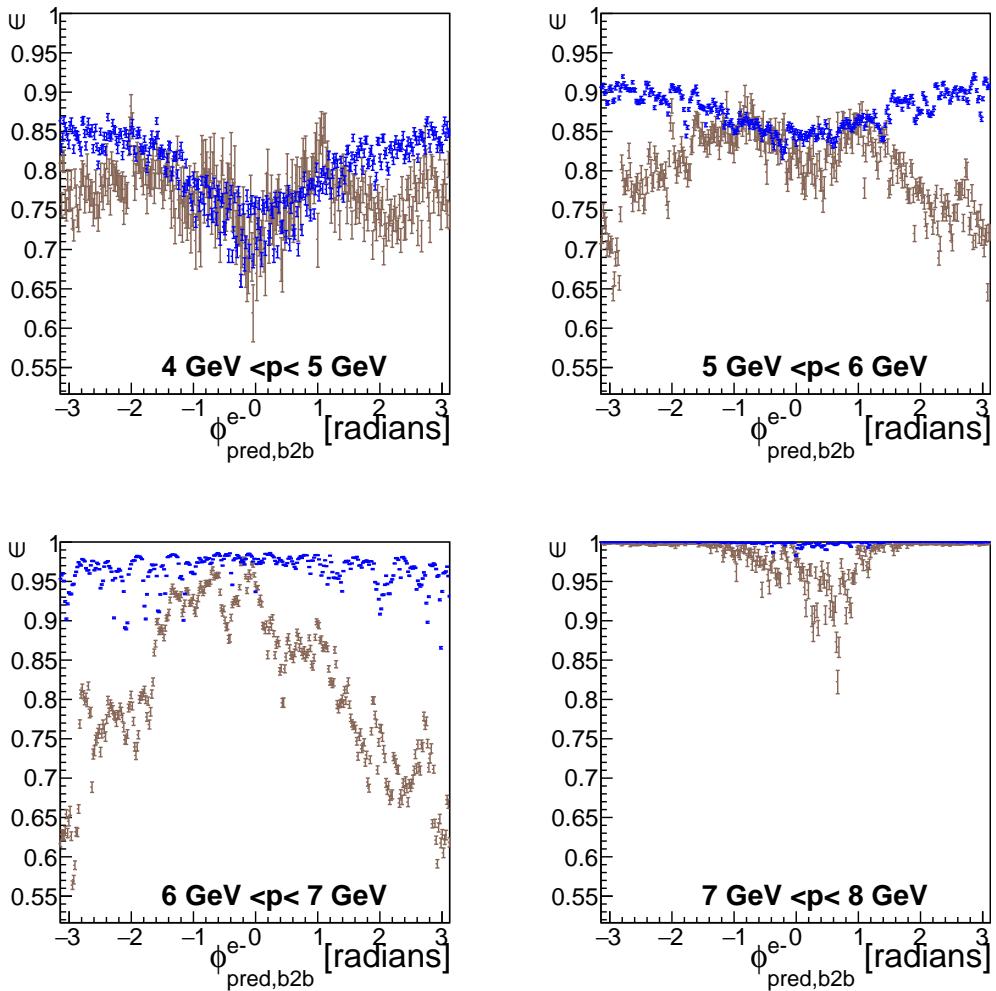
Figure 9.3.: Electron tracking efficiency plots as function of $\phi_{\mathrm{pred,b2b}}$ for different momenta in the forward end-cap. The tracking efficiency of phase2 data is shown in brown and phase3 data in blue. The pink line indicates the different sectors of the ECL.
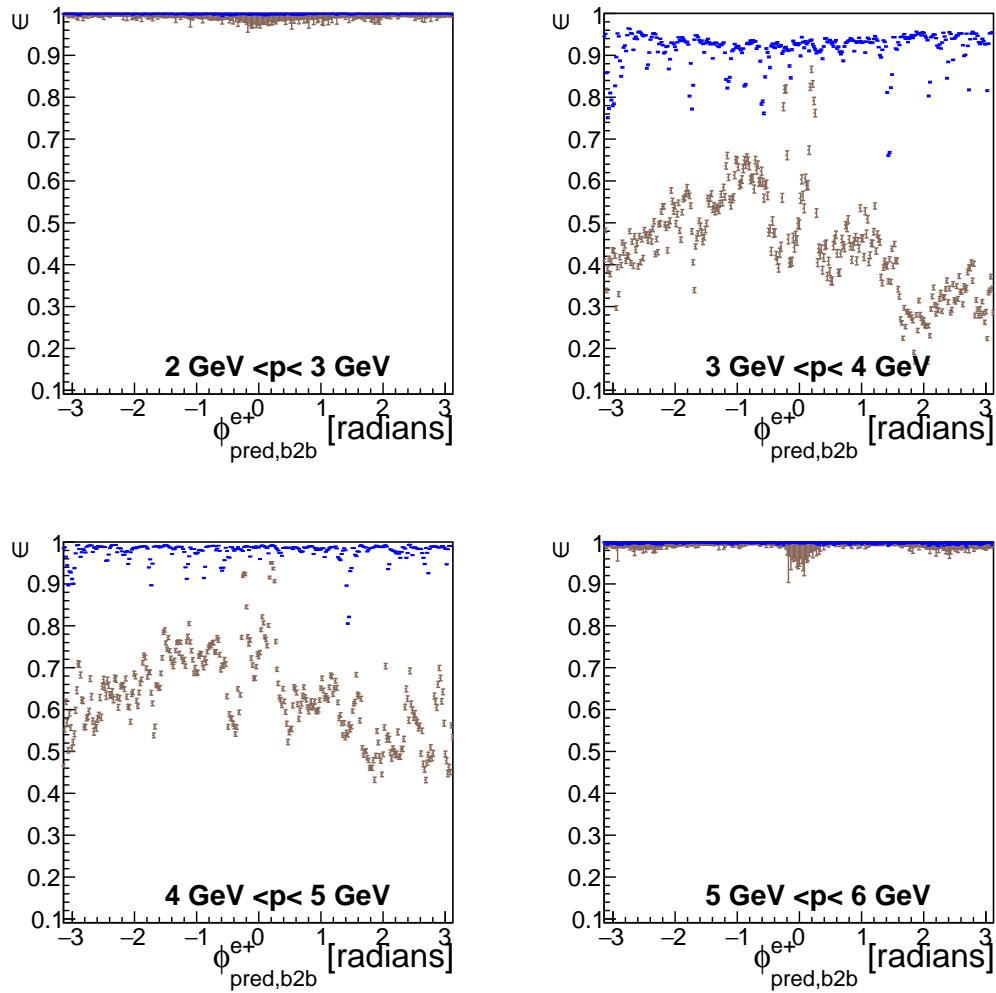
Figure 9.4.: Positron tracking efficiency plots as function of $\phi_{\mathrm{pred,b2b}}$ for different momenta in the forward end-cap. The tracking efficiency of phase2 data is shown in brown and phase3 data in blue. The pink line indicates the different sectors of the ECL.

10

Summary And Conclusion

I‍N this work the tracking efficiency of the tracking and reconstruction detectors of Belle II was presented. Using Monte Carlo-Truth information, which is the information of the generated MC particle and therefore the true properties of these particles, I showed that it is possible to select outgoing electron/positron events, i.e. Bhabha events, with informations solely coming from the electromagnetic calorimeter (ECL). This selection is rather rudimentary because it is mostly based on the kinematics of the Bhabha process. Using this selection, I managed to reconstruct these Bhabha events even without the MC-Truth information. Therefore, it was possible to apply this selection to real data and tracking efficiencies could be calculated. This was done for phase2 MC, phase2 data, phase3 MC and phase3 data. The calculated tracking efficiencies for phase2 MC and phase2 data were compared in detail and differences were highlighted. The same was done with the tracking efficiencies of phase3 MC and phase3 data.

Phase2 was a test run to study the background at Belle II. For this phase only a small fraction of the vertex detectors (VXD) were installed.

For the phase2 tracking efficiency we saw that most of the time, the tracking efficiencies of phase2 MC are higher than the tracking efficiencies of phase2 data. But this is expected, because in MC the detector has no dead time, it is always performing at its best and some structures of the detector, like cabling or screws, which may interfere with the outgoing particles, are maybe not implemented in the simulation, ultimately leading to a higher efficiency. This is also true for phase3. Unfortunately, the phase2 and phase3 MC have noticeably larger error bars compared to phase2 and phase3 data due to the lower statistics.

The tracking efficiencies, especially in the end-caps, of phase2 MC and phase2 data have remarkable differences in their structure and in their height. The biggest differences occur at $\phi_{\mathrm{pred,b2b}} \approx 0$. For these angles even the structure of the tracking efficiencies vary often. Additionally, both tracking efficiencies drop down drastically to 0 at the end of both end-caps. In the barrel phase2 MC and phase2 data are closer to each other, for the most part.

10. Summary And Conclusion

For phase3, the first physics run for Belle II, more parts of the VXD were installed. This includes the complete silicon vertex detector (SVD) and most of the pixel detector (PXD).

Overall, the tracking efficiencies in both end-caps improved for electrons and positrons for all momenta compared to phase2, especially in the end of both end-caps.

The best electron tracking efficiencies with $\epsilon \gtrsim 0.99$ for phase3 data and $\epsilon \gtrsim 0.98$ for phase3 MC appear in the forward end-cap for momenta above $7\,\mathrm{GeV}$. In the barrel similar efficiencies are reached for momenta above $6\,\mathrm{GeV}$. In contrast, the electron tracking efficiency of phase2 data is only above ~ 0.9 in the forward end-cap and above ~ 0.95 in the barrel for the same momenta ranges. Phase2 MC has a similar electron tracking efficiency compared to phase3 MC for the same momenta ranges.

For positrons the best tracking efficiencies appear in the backward end-cap for momenta between $2\,\mathrm{GeV}$ and $3\,\mathrm{GeV}$, and between $5\,\mathrm{GeV}$ and $6\,\mathrm{GeV}$ for phase3 data. For both momenta ranges the efficiencies are above 0.99. For phase3 data the highest positron tracking efficiency in the barrel appears for momenta between $4\,\mathrm{GeV}$ and $5\,\mathrm{GeV}$ with $\epsilon \gtrsim 0.98$. For phase3 MC the highest positron tracking efficiency with $\epsilon \gtrsim 0.98$ appears in the barrel and in the backward end-cap for momenta between $4\,\mathrm{GeV}$ and $5\,\mathrm{GeV}$. For the same momenta ranges as mentioned for phase3 data, the phase2 data tracking efficiency is above ~ 0.98 in the backward end-cap and above ~ 0.96 in the barrel for almost all values of $\phi_{\mathrm{pred,b2b}}$. For phase2 MC the tracking efficiency is similar compared to the phase3 MC tracking efficiency for the same momenta ranges.

One has to mention that, for phase3 data, there are drops in the tracking efficiency for some values of $\phi_{\mathrm{pred,b2b}}$ in the endcaps. In the barrel these horizontal efficiency drops are also visible for the electron tracking efficiency. These drops appear to be distributed randomly. The reason for these drops has to be determined in further studies. Additionally, there was an improvement in the phase3 MC simulation in the sense that the tracking efficiencies of phase3 MC and phase3 data are closer to each other compared to phase2 MC and phase2 data. For phase3 it is difficult to highlight differences between the tracking efficiencies of phase3 data and phase3 MC because they are very close to each other and phase3 MC has very large error bars due to its lower statistic.

The studies performed and the programs developed in this thesis will allow a quick assessment of tracking efficiency for future data taking.

A
Appendix

A.1. Additional Preparation Plots

The single MC file used for phase2 MC is located on Grid at:

/belle/MC/release-01-00-02/DB00000294/MC10/prod00004668/s00/e1002/4S/
r00000/3600520000/mdst/sub00/mdst_000050_prod00004668_task10010000050.root

The generated file is located on KEKCC at:

/home/belle2/msobotzi/bhabha/bhabha_vpho_mc.root

The single phase2 data file is located on KEKCC at:

/ghi/fs01/belle2/bdata//Data/release-03-00-03/DB00000528/proc00000008/e0003/
4S/r02608/all/mdst/sub00/*.root

The generated file is located on KEKCC at:

/home/belle2/msobotzi/bhabha/bhabha_vpho_data_608.root
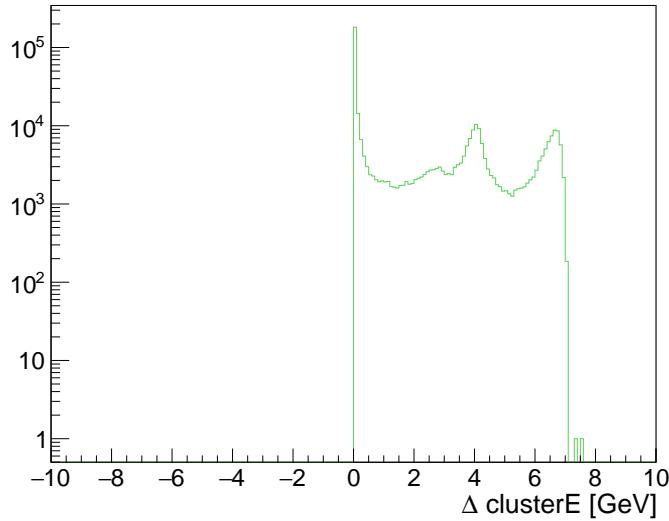
Figure A.1.: clusterE(HclE) - clusterE(LclE) of the reconstructed candidates. This shows that the HclE daughters always has higher cluster energy than the LclE daughter.
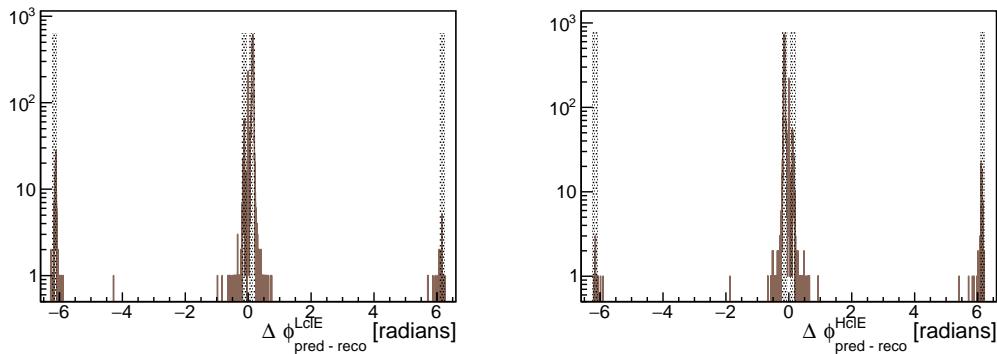
Figure A.2.: Left: $\Delta\phi_{\text{pred}-\text{reco}}^{\text{LclE}}$. Right: $\Delta\phi_{\text{pred}-\text{reco}}^{\text{HclE}}$. Only particles within the gray area are taken into account. Both plots are created with phase2 data. Note the logarithmic scale.

Figure A.3.: Left: $\Delta\phi^{\mathrm{LclE}}_{\mathrm{pred-reco}}$. Right: $\Delta\phi^{\mathrm{HclE}}_{\mathrm{pred-reco}}$. Only particles within the gray area are taken into account. Both plots are created with phase2 MC data. Note the logarithmic scale.
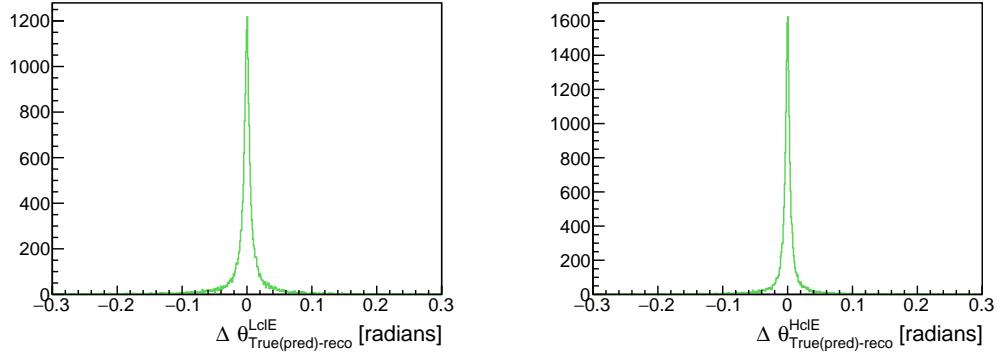
Figure A.4.: Left: $\Delta\theta^{\mathrm{LclE}}_{\mathrm{True(pred)-reco}}$. Right: $\Delta\theta^{\mathrm{HclE}}_{\mathrm{True(pred)-reco}}$. Both plots are created with phase2 MC.

Figure A.5.: Left: $\Delta\theta^{\mathrm{LclE}}_{\mathrm{True(pred)-reco}}$. Right: $\Delta\theta^{\mathrm{HclE}}_{\mathrm{True(pred)-reco}}$. Both plots are created with phase2 data.
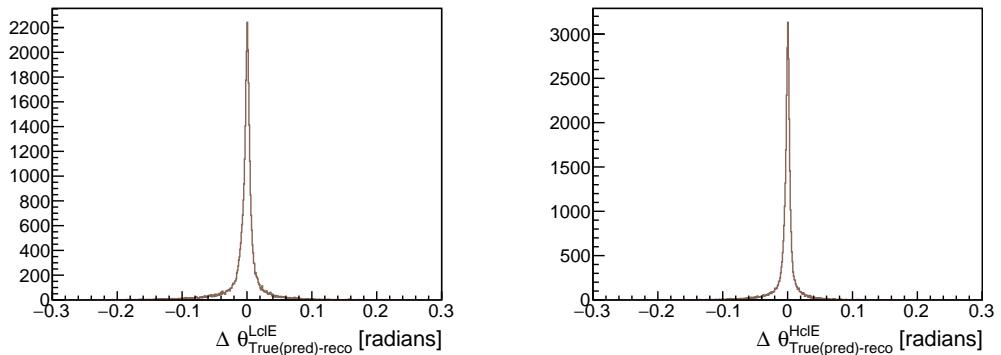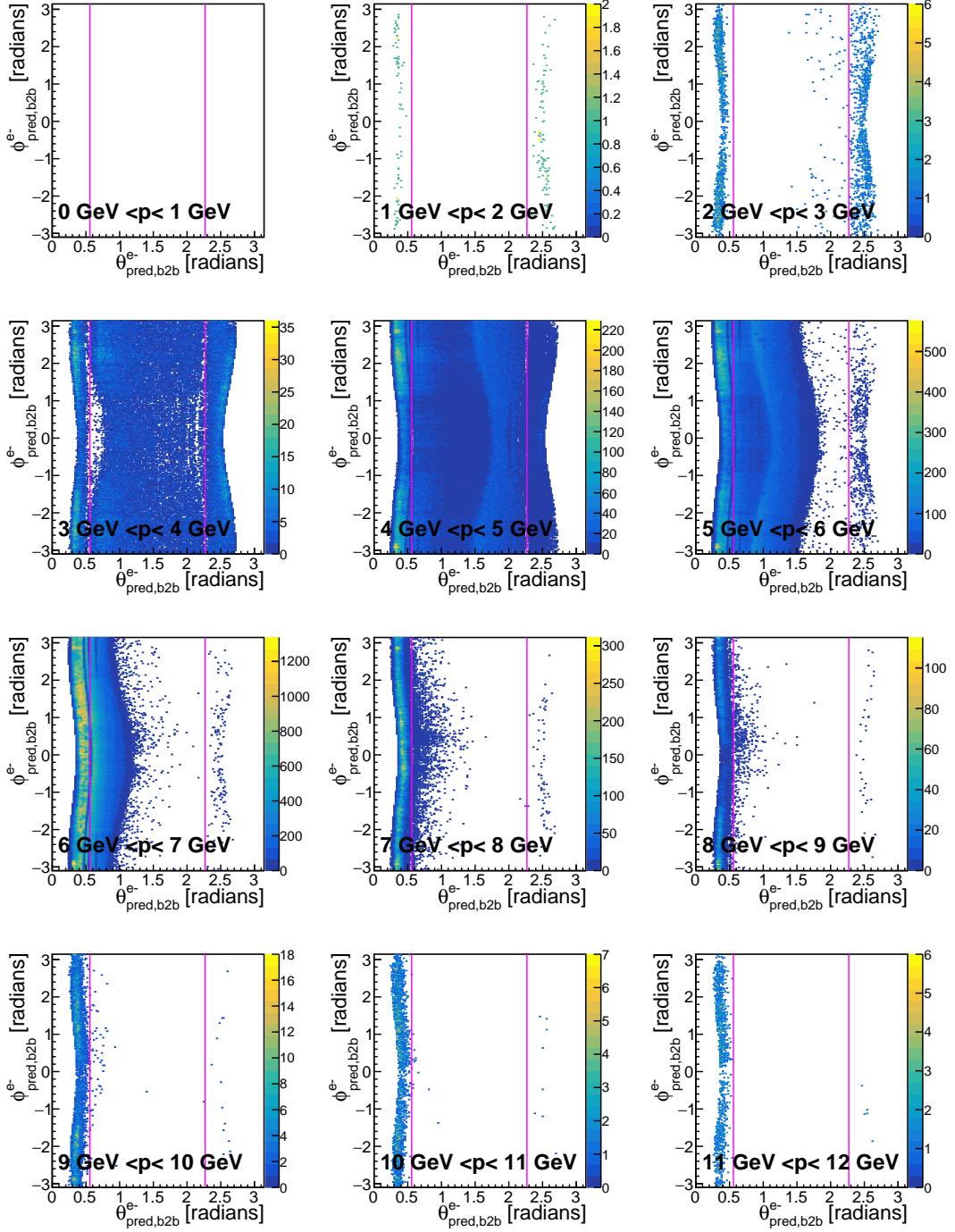
Figure A.6.: Predicted $\theta_{\mathrm{pred,b2b}}$ and $\phi_{\mathrm{pred,b2b}}$ denominator histograms of the *probe* particle for different momenta for electrons for phase2 Data are shown. The different areas of interest are indicated by the pink line.

Figure A.7.: Predicted $\theta_{\mathrm{pred,b2b}}$ and $\phi_{\mathrm{pred,b2b}}$ enumerator histograms of the *probe* particle for different momenta for electrons for phase2 MC are shown. The different areas of interest are indicated by the pink line.
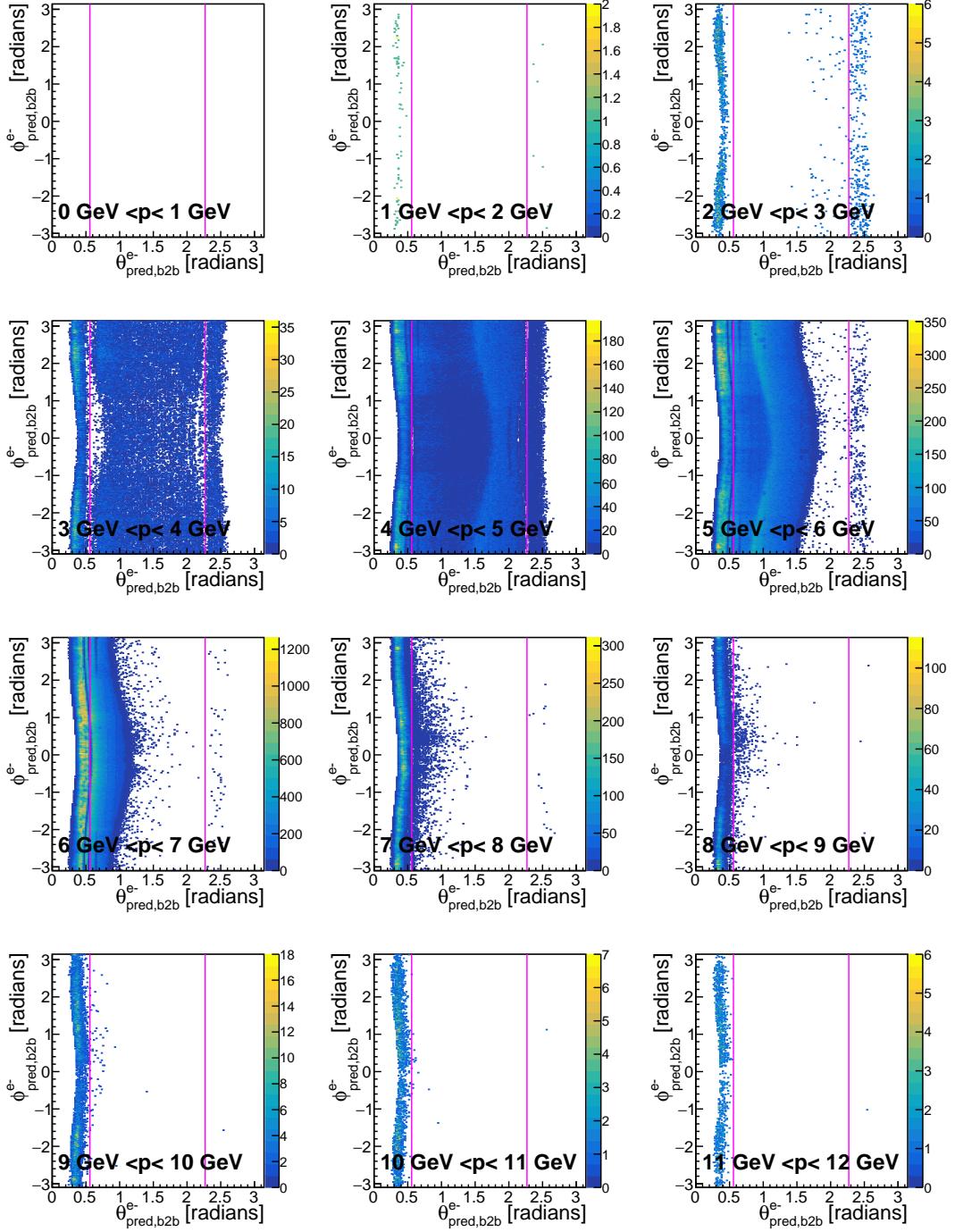
Figure A.8.: Predicted $\theta_{\text{pred,b2b}}$ and $\phi_{\text{pred,b2b}}$ enumerator histograms of the *probe* particle for different momenta for electrons for phase2 data are shown. The different areas of interest are indicated by the pink line.
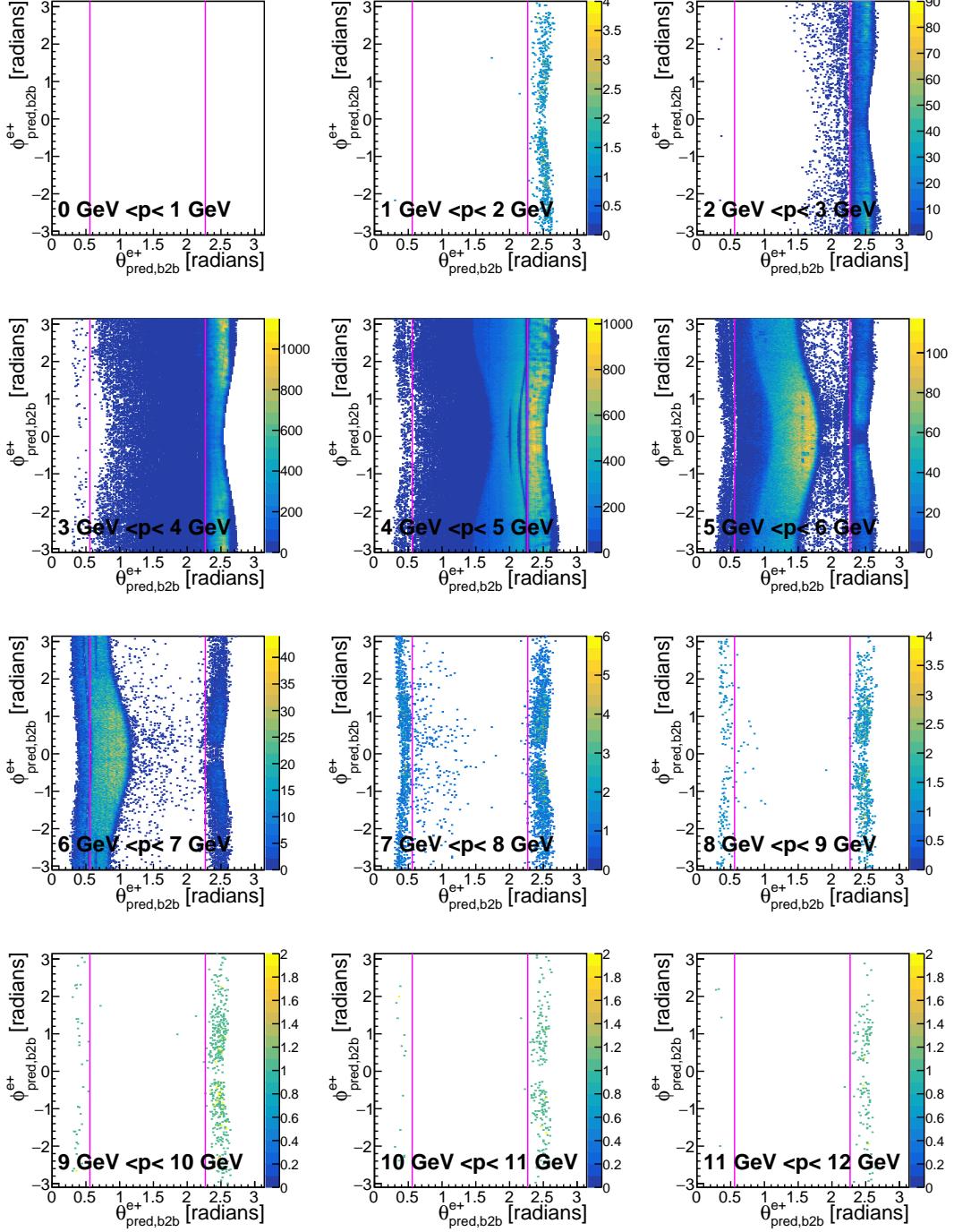
Figure A.9.: Predicted $\theta_{\text{pred,b2b}}$ and $\phi_{\text{pred,b2b}}$ denominator histograms of the *probe* particle for different momenta for positrons for phase2 Data are shown. The different areas of interest are indicated by the pink line.

Figure A.10.: Predicted $\theta_{\mathrm{pred,b2b}}$ and $\phi_{\mathrm{pred,b2b}}$ denominator histograms of the *probe* particle for different momenta for positrons for phase2 MC are shown. The different areas of interest are indicated by the pink line.
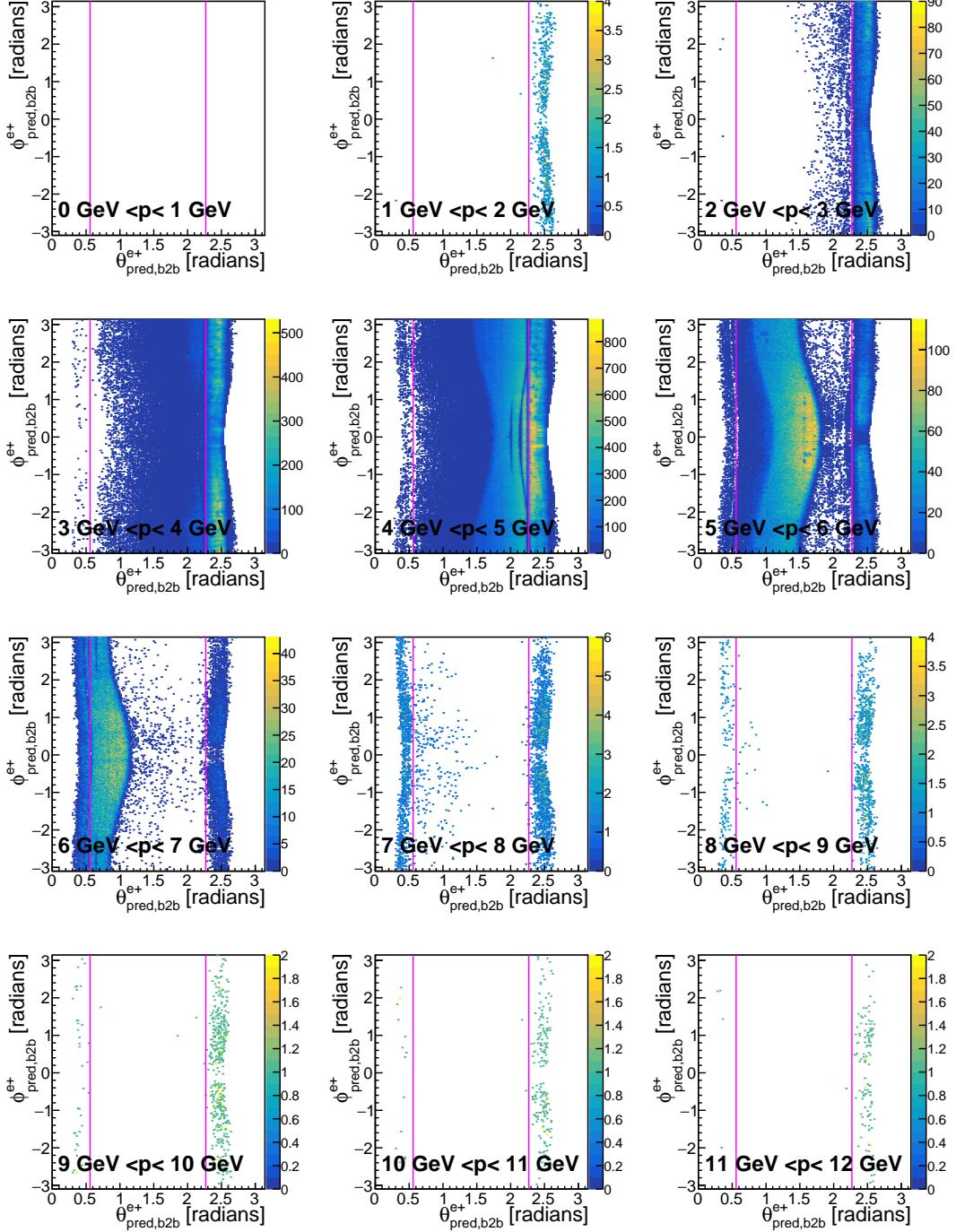
Figure A.11.: Predicted $\theta_{\mathrm{pred,b2b}}$ and $\phi_{\mathrm{pred,b2b}}$ denominator histograms of the *probe* particle for different momenta for positrons for phase2 Data are shown. The different areas of interest are indicated by the pink line.

Figure A.12.: Predicted $\theta_{\mathrm{pred,b2b}}$ and $\phi_{\mathrm{pred,b2b}}$ denominator histograms of the *probe* particle for different transverse momenta for electrons for phase2 Data are shown. The different areas of interest are indicated by the pink line.
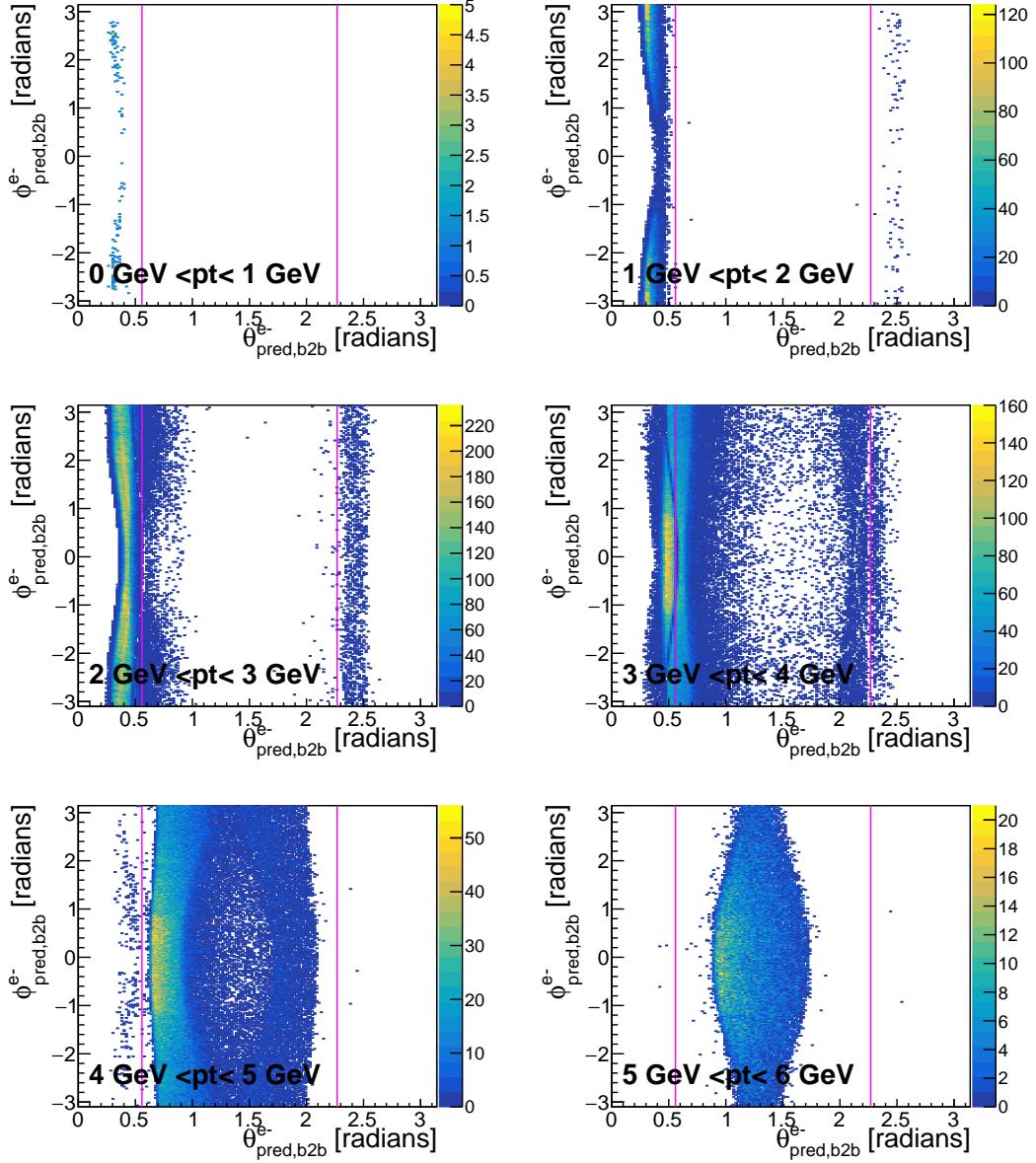
Figure A.13.: Predicted $\theta_{\mathrm{pred,b2b}}$ and $\phi_{\mathrm{pred,b2b}}$ denominator histograms of the *probe* particle for different transverse momenta for electrons for phase2 MC are shown. The different areas of interest are indicated by the pink line.

Figure A.14.: Predicted $\theta_{\mathrm{pred,b2b}}$ and $\phi_{\mathrm{pred,b2b}}$ denominator histograms of the *probe* particle for different transverse momenta for electrons for phase2 data are shown. The different areas of interest are indicated by the pink line.
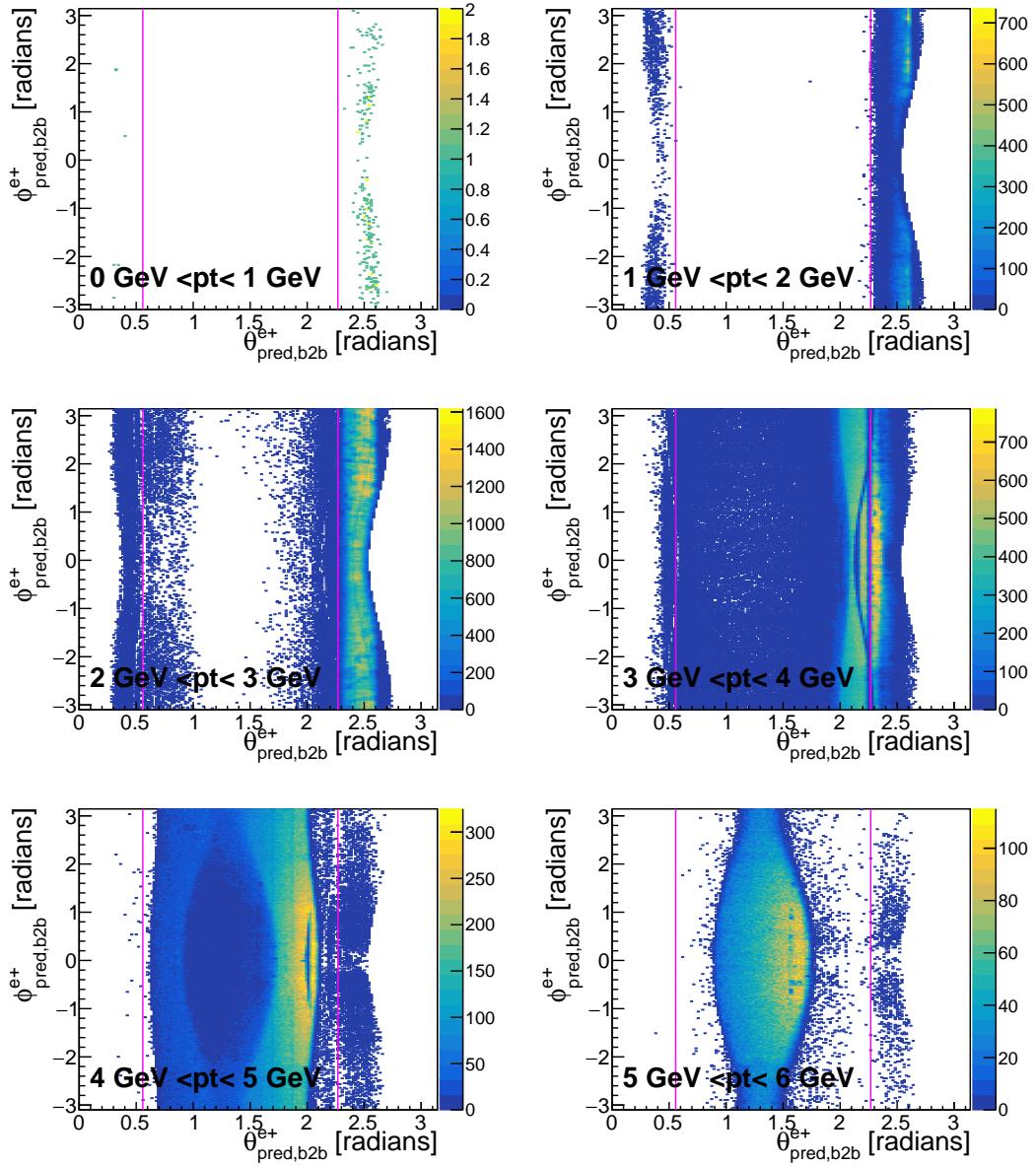
Figure A.15.: Predicted $\theta_{\text{pred,b2b}}$ and $\phi_{\text{pred,b2b}}$ denominator histograms of the *probe* particle for different transverse momenta for positrons for phase2 Data are shown. The different areas of interest are indicated by the pink line.

Figure A.16.: Predicted $\theta_{\mathrm{pred,b2b}}$ and $\phi_{\mathrm{pred,b2b}}$ denominator histograms of the *probe* particle for different transverse momenta for positrons for phase2 MC are shown. The different areas of interest are indicated by the pink line.
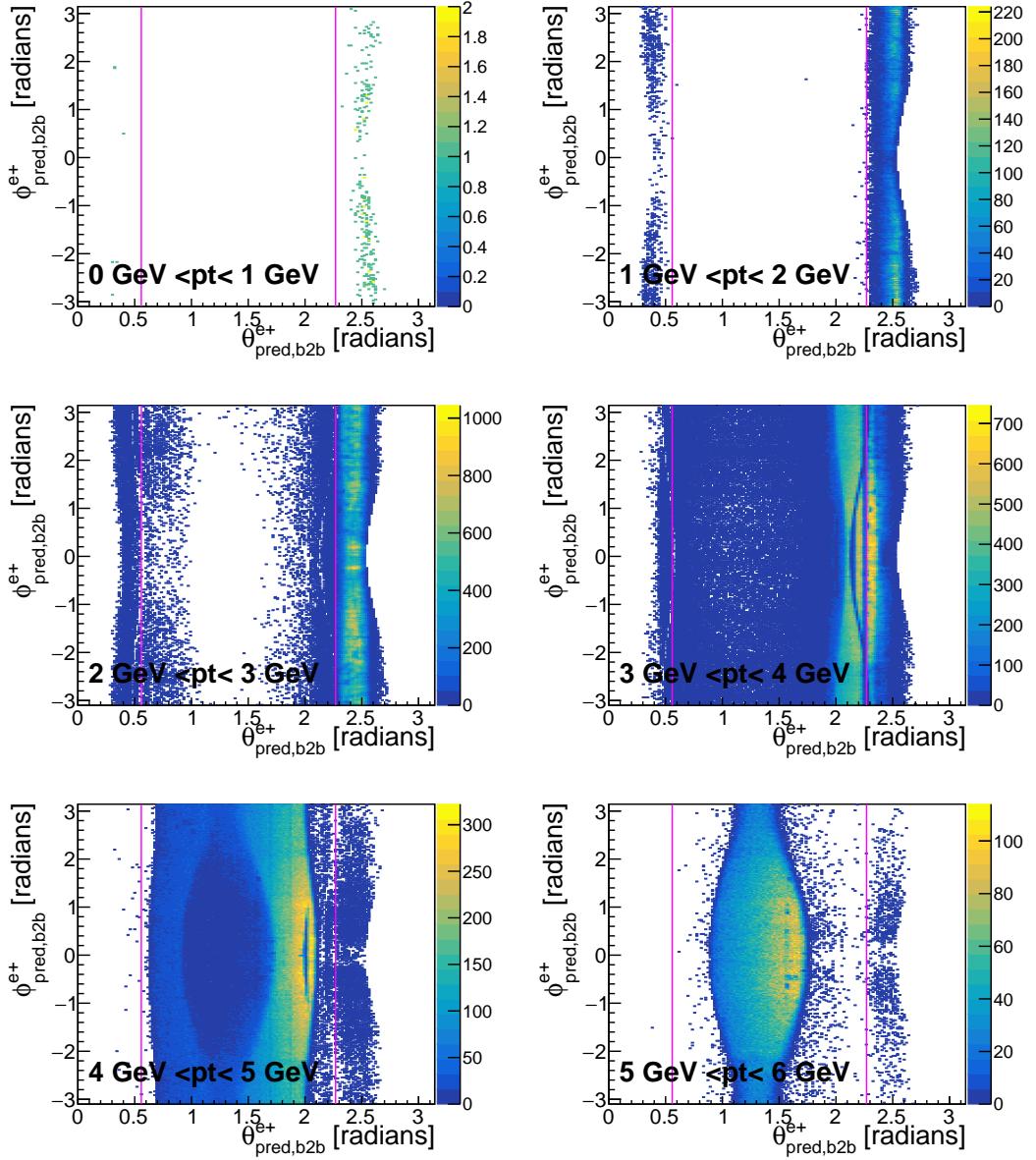
Figure A.17.: Predicted $\theta_{\mathrm{pred,b2b}}$ and $\phi_{\mathrm{pred,b2b}}$ denominator histograms of the *probe* particle for different transverse momenta for positrons for phase2 data are shown. The different areas of interest are indicated by the pink line.

A.2. Phase2

A.2.1. Location Of Phase2 Files

The phase2 MC files are located on GridKa at:

/belle/MC/release-01-00-02/DB00000294/MC10/prod00004668/s00/e1002/4S/
r00000/3600520000/mdst/sub00

The phase2 data files are located on KEKCC at:

/ghi/fs01/belle2/bdata/Data/release-03-00-03/DB00000528/proc00000008/e0003/
4S/r0*/all/mdst/sub00/*.root

A.2.2. Additional Figures
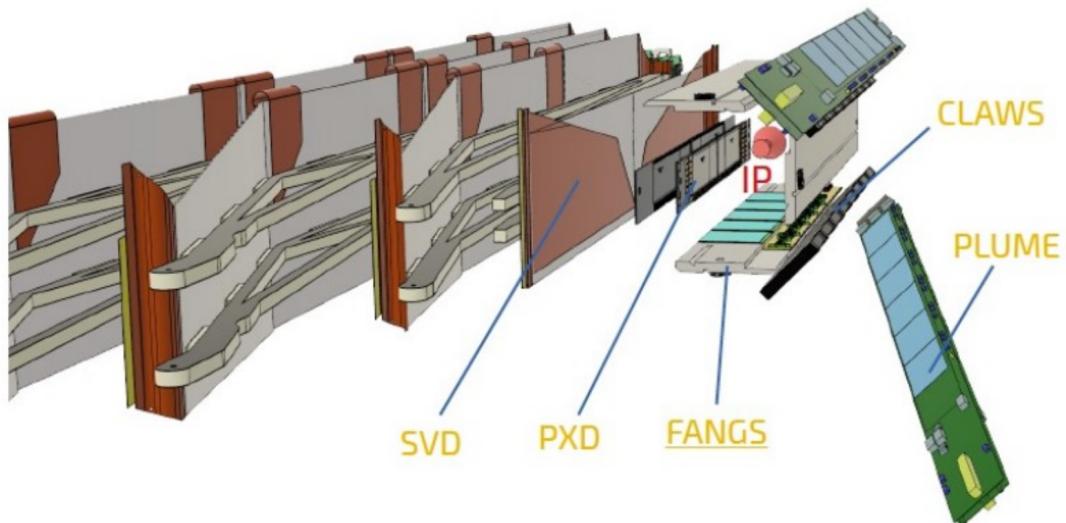
Figure A.18.: The status of the VXD detector during phase2.[36]
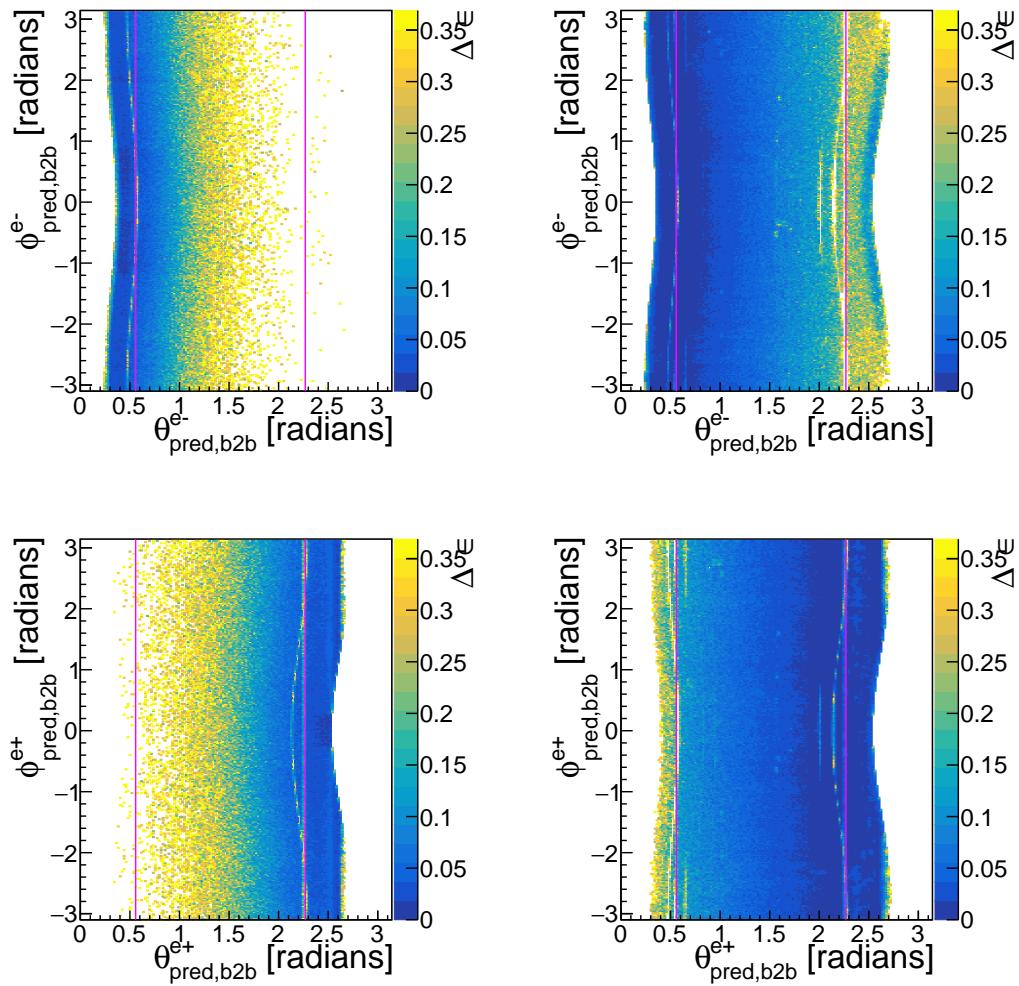
Figure A.19.: $\theta_{\mathrm{pred,b2b}}$-$\phi_{\mathrm{pred,b2b}}$ efficiency errors for phase2. Left: Phase2 MC. Right: Phase2 data. First line: electron efficiency errors. Second line: positron efficiency errors.
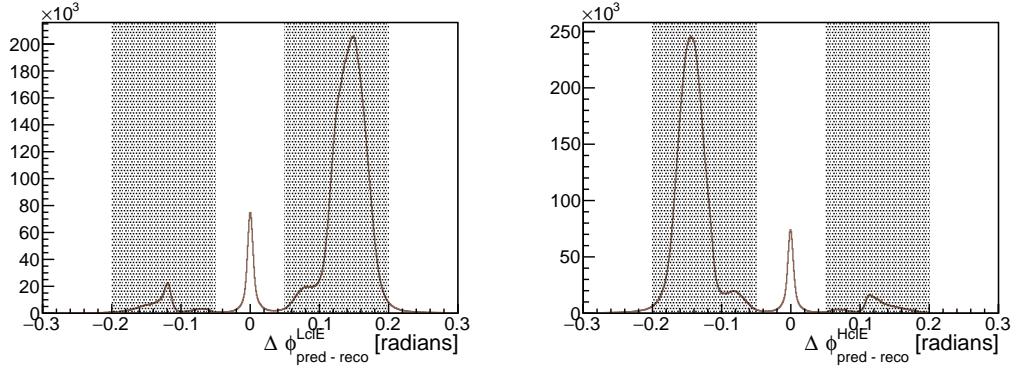
Figure A.20.: Left: $\Delta\phi_{\text{b2bpred-reco}}^{\text{LclE}}$. Right: $\Delta\phi_{\text{b2bpred-reco}}^{\text{HclE}}$. Only particles within the gray area are taken into account. Both plots are created with phase2 data. The middle peak in both plots are created by $e^+e^- \to \gamma\gamma$ events.
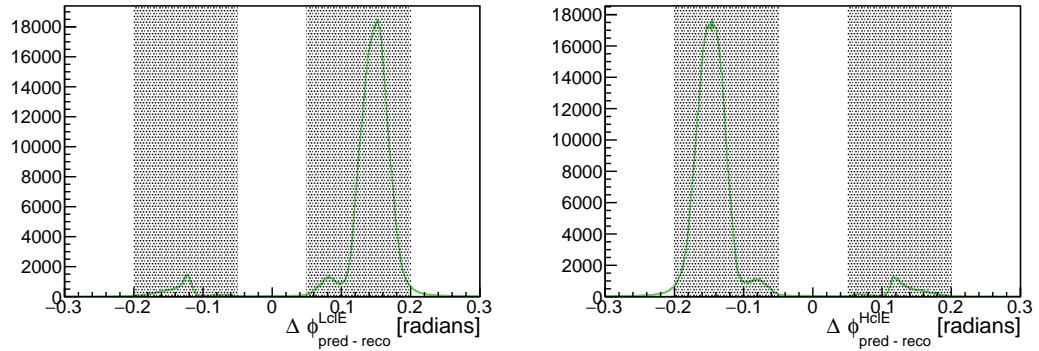
Figure A.21.: Left: $\Delta\phi_{\text{pred-reco}}^{\text{LclE}}$. Right: $\Delta\phi_{\text{pred-reco}}^{\text{HclE}}$. Only particles within the gray area are taken into account. Both plots are created with phase2 MC. There is no middle peak because only $ee \to ee$ events were generated.

A.3. Phase3

A.3.1. Location Of Phase3 Files

To have as much events as possible, all phase3 data files are taken into account. They contain all Experiment 7 located on KEKCC at:

/group/belle2/dataprod/Data/release-03-02-02/DB00000654/proc9/e0007/4S/ r0*/all/mdst/sub00/*.root

and Experiment 8 located on KEKCC at (as of October 2019):

/group/belle2/dataprod/Data/release-03-02-02/DB00000654/proc9/e0008/4S/ r0*/all/mdst/sub00/*.root

For Monte Carlo we will consider all files located on GridKa at:

/belle/MC/release-01-00-02/DB00000294/MC10/prod00004664/s00/e0000/4S/ r00000/3600520000/mdst/sub00

A.3.2. Additional Figures
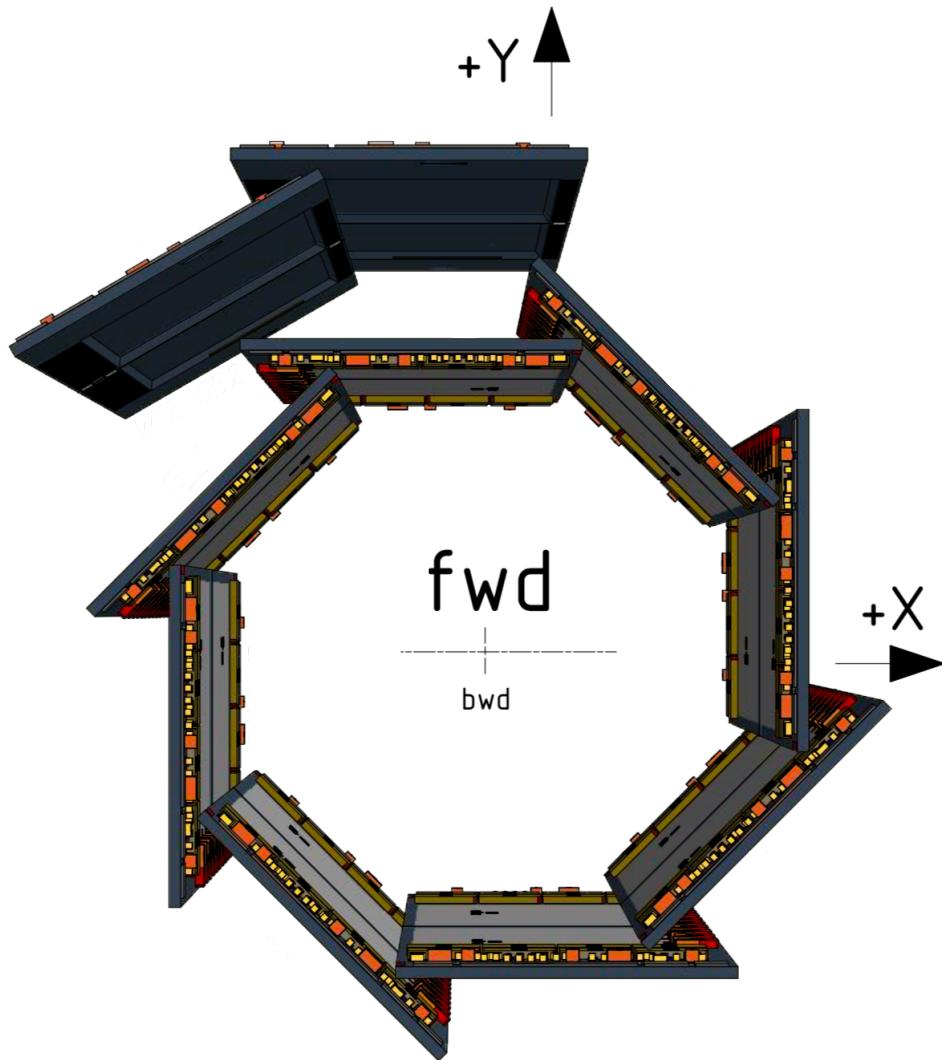
Figure A.22.: The status of the PXD during phase3. The innermost layer is completely installed and only 2 out 12 from the outer layer are installed. This sketch was modified to make it easier to look at.[37]
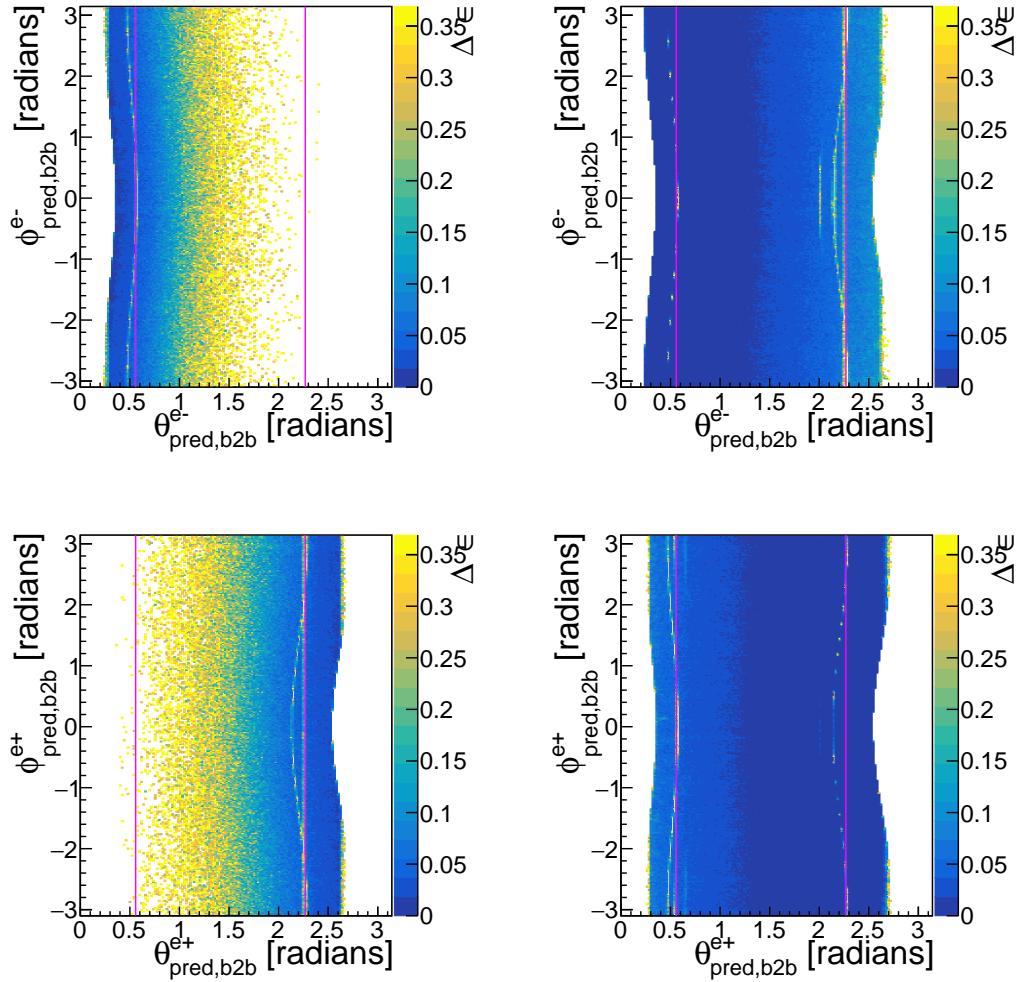
Figure A.23.: $\theta_{\mathrm{pred,b2b}}$-$\phi_{\mathrm{pred,b2b}}$ efficiency errors for phase2. Left: Phase3 MC. Right: Phase3 data. First line: electron efficiency errors. Second line: positron efficiency errors.
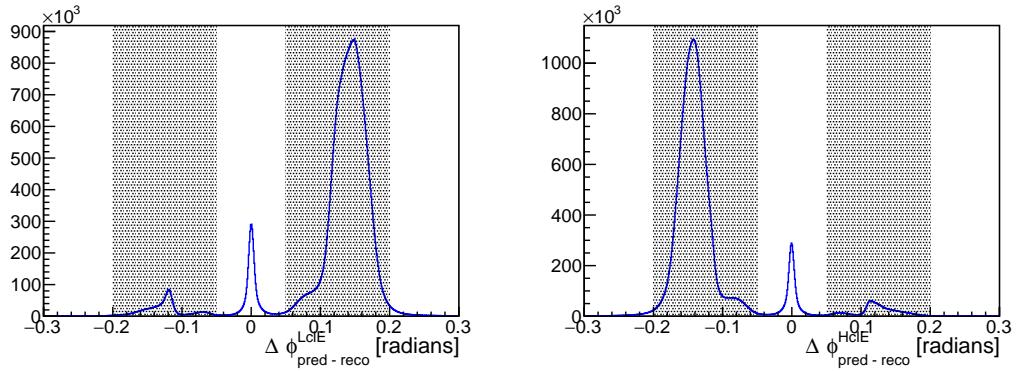
Figure A.24.: Left: $\Delta\phi_{\mathrm{pred-reco}}^{\mathrm{LclE}}$. Right: $\Delta\phi_{\mathrm{pred-reco}}^{\mathrm{HclE}}$. Only particles within the gray area are taken into account. Both plots are created with phase3 data. The middle peak in both plots are created by $e^+e^- \to \gamma\gamma$ events.
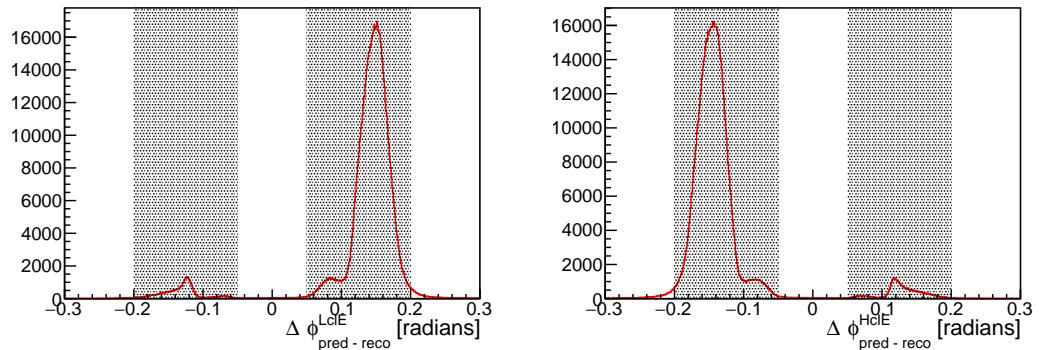
Figure A.25.: Left: $\Delta\phi_{\mathrm{pred-reco}}^{\mathrm{LclE}}$. Right: $\Delta\phi_{\mathrm{pred-reco}}^{\mathrm{HclE}}$. Only particles within the gray area are taken into account. Both plots are created with phase3 MC. There is no middle peak because only $ee \to ee$ events were generated.

Figure A.26.: Left: $\Delta\phi^{\text{LclE}}_{\text{pred}-\text{reco}}$. Right: $\Delta\phi^{\text{HclE}}_{\text{pred}-\text{reco}}$. Phase3 data (blue) is shown together with phase2 data (brown). The plots are normalized.
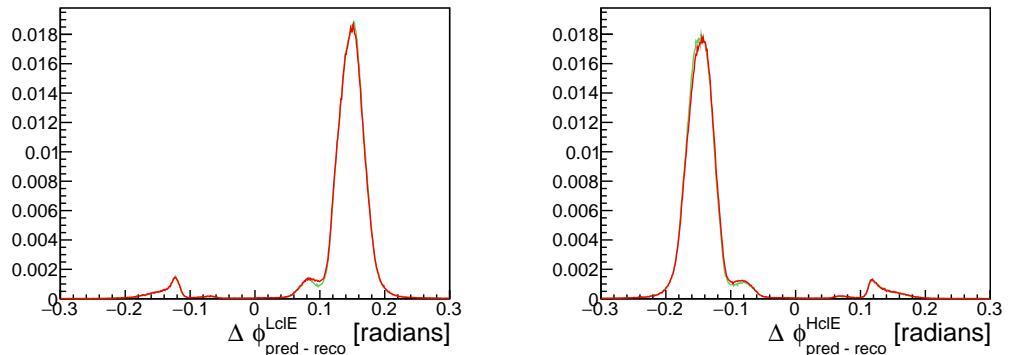
Figure A.27.: Left: $\Delta\phi^{\text{LclE}}_{\text{pred}-\text{reco}}$. Right: $\Delta\phi^{\text{HclE}}_{\text{pred}-\text{reco}}$. Phase3 MC (red) is shown together with phase2 MC (green). The plots are normalized.

List of Figures

List of Tables

Bibliography

[1] Michael Riordan Max Dresden Lillian Hoddeson Laurie Brown.
The Rise of the Standard Model: Particle Physics in the 1960's and 1970's.
Cambridge University Press, 1997.
ISBN: 0521578167.

[2] *Fundamental Particles.*
URL: https://www.universetoday.com/tag/fundamental-particles/.
visited on 20.05.2019.

[3] Frederick Reines.
"40 years of neutrino physics".
In: *Progress in Particle and Nuclear Physics* 32 (1994), pp. 1 –12.
ISSN: 0146-6410.
URL: http : / / www . sciencedirect . com / science / article / pii /
0146641094900035.

[4] C Sivaram.
"What is special about the planck mass?"
In: *arXiv preprint arXiv:0707.0058* (2007).
URL: https://arxiv.org/abs/0707.0058.

[5] *Dark Matter.*
URL: https://home.cern/science/physics/dark-matter.
visited on 24.11.2019.

[6] Hans-Thomas Janka.
Supernovae und kosmische Gammablitze.
Springer, 2011.
ISBN: 978-3-8274-2072-5.

[7] Thomas Hambye.
"CP violation and the matter–antimatter asymmetry of the Universe".
In: *Comptes Rendus Physique* 13.2 (2012). Flavour physics and CP violation /
Physique de la saveur et violation de CP, pp. 193 –203.
ISSN: 1631-0705.
URL: http : / / www . sciencedirect . com / science / article / pii /
S1631070511001873.

Bibliography

[8] Daniel V. Schroeder.
     Feynman Diagrams and Electron-Positron Annihilation.
     Oct. 2002.
     URL: https://physics.weber.edu/schroeder/feynman/.
     visited on 27.05.2019.

[9] E. Kou et al.
     The Belle II Physics Book.
     Aug. 2018.
     URL: https://arxiv.org/abs/1808.10567.

[10] Abe et al.
     "Achievements of KEKB".
     In: *Progress of Theoretical and Experimental Physics* 2013.3 (Mar. 2013).
     ISSN: 2050-3911.
     DOI: 10.1093/ptep/pts102.
     eprint: http://oup.prod.sis.lan/ptep/article-pdf/2013/3/03A001/
     4440618/pts102.pdf.
     URL: https://dx.doi.org/10.1093/ptep/pts102.

[11] Ivan Heredia de la Cruz.
     "The Belle II experiment: fundamental physics at the flavor frontier".
     In: *Journal of Physics: Conference Series* 761 (Sept. 2016).
     DOI: 10.1088/1742-6596/761/1/012017.

[12] Akemoto et al.
     "The KEKB injector linac".
     In: *Progress of Theoretical and Experimental Physics* 2013.3 (Mar. 2013).
     ISSN: 2050-3911.
     DOI: 10.1093/ptep/ptt011.
     eprint: http://oup.prod.sis.lan/ptep/article-pdf/2013/3/03A002/
     4441335/ptt011.pdf.
     URL: https://dx.doi.org/10.1093/ptep/ptt011.

[13] Werner Herr and Bruno Muratori.
     "Concept of luminosity".
     In: (Feb. 2006).
     DOI: 10.5170/CERN-2006-002.361.

[14] Fernando Abudinén.
     "Development of a B^0 flavor tagger and performance study of a novel time-
     dependant CP analysis of the decay $B^0 \to \pi^0\pi^0$ at Belle II".
     PhD Thesis. Ludwig-Maximilians-Universität München, Sept. 2018.

[15] Abe et al.
     "Belle II Technical Design Report".
     In: (Nov. 2010).
     URL: arXiv:1011.0352.

[16] *Electrons and Positrons Collide for the first time in the SuperKEKB Accelerator.*
Apr. 2018.
URL: https://www.kek.jp/en/newsroom/2018/04/26/0700/.
visited on 25.02.2019.

[17] Wikimedia Commons.
File:Spherical polar coordinates.png — Wikimedia Commons, the free media repository.
visited on 25.11.2019.
2015.
URL: \url{https://commons.wikimedia.org/w/index.php?title=File:
Spherical_polar_coordinates.png&oldid=155599525}.

[18] Nobuhiro Shimizu.
"Development of the Silicon Vertex Detector for Belle II experiment".
Department of Physics, University of Tokyo.
URL: http://hep.phys.s.u-tokyo.ac.jp/?page_id=229.
visited on 25.02.2019.

[19] F. Bernlochner et al.
"Online Data Reduction for the Belle II Experiment using DATCON".
In: (Sept. 2017).
DOI: 10.1051/epjconf/201715000014.
URL: https://arxiv.org/abs/1709.00612.

[20] C. Marinas and M. Vos.
"The Belle-II DEPFET pixel detector: A step forward in vertexing in the superKEKB flavour factory".
In: *Nuclear Instruments and Methods in Physics Research Section A: Accelerators, Spectrometers, Detectors and Associated Equipment* 650.1 (2011). International Workshop on Semiconductor Pixel Detectors for Particles and Imaging 2010, pp. 59 –63.
ISSN: 0168-9002.
DOI: https://doi.org/10.1016/j.nima.2010.12.116.
URL: http://www.sciencedirect.com/science/article/pii/
S0168900210028962.

[21] Belle II Italian collaboration.
Silicon Vertex Detector.
Mar. 2019.
URL: https://web.infn.it/Belle-II/index.php/detector/svd.
visited on 06.03.2019.

[22] Markus Friedl et al.
"The silicon vertex detector of the Belle II experiment".
In: *Nuclear Instruments and Methods in Physics Research Section A: Accelerators, Spectrometers, Detectors and Associated Equipment* 628.1 (2011), pp. 103–106.

Bibliography

[23] Thomas Hauth.
Pattern Recognition at Belle II.
Belle2-Talk.
Dec. 2016.

[24] PA Cerenkov.
"PA Cerenkov, Phys. Rev. 52, 378 (1937)."
In: *Phys. Rev.* 52 (1937), p. 378.

[25] E. Torassa.
"Particle identification with the TOP and ARICH detectors at Belle II".
In: *Nuclear Instruments and Methods in Physics Research Section A: Accelerators, Spectrometers, Detectors and Associated Equipment* 824 (2016). Frontier Detectors for Frontier Physics: Proceedings of the 13th Pisa Meeting on Advanced Detectors, pp. 152 –155.
ISSN: 0168-9002.
URL: http : / / www . sciencedirect . com / science / article / pii / S0168900215013789.

[26] V. Aulchenko et al.
"Electromagnetic calorimeter for Belle II".
In: *Journal of Physics: Conference Series* 587 (2015), p. 012045.
DOI: 10.1088/1742-6596/587/1/012045.
URL: https://doi.org/10.1088%2F1742-6596%2F587%2F1%2F012045.

[27] William R Leo.
Techniques for nuclear and particle physics experiments: a how-to approach.
Springer Science & Business Media, 2012.
DOI: 10.1007/978-3-642-57920-2.

[28] T. Aushev et al.
"A scintillator based endcap K L and muon detector for the Belle II experiment".
In: (Apr. 2015).
DOI: 10.1016/j.nima.2015.03.060.
URL: https://arxiv.org/abs/1406.3267v3.

[29] Yoshihito Iwasaki et al.
"Level 1 trigger system for the Belle II experiment".
In: *2010 17th IEEE-NPSS Real Time Conference.*
IEEE. 2010,
Pp. 1–9.

[30] Filippo Dattola, Lorenzo Vitale, and Diego Tonelli.
"Tracking studies for the Belle II detector".
Presented on 20 07 2018.
PhD thesis. Trieste: Trieste, University of Trieste, 2018.

[31] Andreas Moll.
"The Software Framework of the Belle II Experiment".

In: *Journal of Physics: Conference Series* 331.3 (2011), p. 032024.
DOI: 10.1088/1742-6596/331/3/032024.
URL: https://doi.org/10.1088%2F1742-6596%2F331%2F3%2F032024.

[32] Rod Pierce.
"Triangular Number Sequence" Math Is Fun.
Nov. 2018.
URL: http://www.mathsisfun.com/algebra/triangular-numbers.html.
visited on 27.05.2019.

[33] *Trigger Bit Table.*
June 2019.
URL: https://confluence.desy.de/display/BI/TriggerBitTable.
visited on 22.08.2019.

[34] *TEfficiency Class Reference.*
2019.
URL: https://root.cern.ch/doc/master/classTEfficiency.html.
visited on 09.10.2019.

[35] Y. Ushiroda.
Kick-off of the Belle II Phase 3 Physics Run.
Mar. 2019.
URL: https://www.kek.jp/en/newsroom/2019/03/25/2030/.

[36] G. Casarosa.
Commissioning of the Belle II Silicon Vertex Detector.
Feb. 2019.
URL: https://confluence.desy.de/display/BI/SVD+SVDTalks?preview=
%2F34034540%2F120373765%2Fb2svd_VCI_final.pdf.

[37] I. Koramov.
Belle II at SuperKEKB, 87th Meeting of Physics Research Committee.
May 2019.
URL: https://indico.desy.de/indico/event/22800/contribution/6/
material/slides/0.pdf.

[38] Robert Oerter.
The theory of almost everything - The Standard Model.
2006.
ISBN: 978-1-101-12674-5.

[39] "Doreen Wacheroth".
"Cross Section".
Mar. 2001.
URL: "https://ed.fnal.gov/painless/htmls/cross.html".
visited on 08.08.2019.

[40] Sara Pohl.
"Track Reconstruction at the First Level Trigger of the Belle II Experiment".

PhD Thesis. Ludwig-Maximilians-Universität München, Dec. 2017.
URL: https://edoc.ub.uni-muenchen.de/22085/.